University of Oklahoma

Graduate College

Quantum dots for Photovoltaic Applications

A DISSERTATION

SUBMITTED TO THE GRADUATE FACULTY

in partial fulfillment of the requirements for the

Degree of

Doctor of Philosophy

By

YANG CHENG
Norman, Oklahoma
2017

Quantum dots for Photovoltaic Applications

A DISSERTATION APPROVED FOR THE
DEPARTMENT OF ENGINEERING PHYSICS

BY

Dr. Ian R. Sellers, Chair

Dr. Michael B. Santos

Dr. Kieran J. Mullen

Dr. Eric R. I. Abraham

Dr. Zhisheng Shi

© Copyright by YANG CHENG 2017
All Rights Reserved.

Acknowledgements

I would like to first express my deepest gratitude to my supervisor, Dr. Ian R. Sellers for his constant support, guidance, and encouragement. I am grateful to have gotten a chance to work with him and know him.

I appreciate the help from Dr. Vincent Whiteside over the years. He is maybe one of the most interesting persons I have ever met.

I would like to thank Dr. Abraham, Dr. Mullen, Dr. Santos, and Dr. Shi for being my supervisory committee members.

I want to thank my current and previous group members, Mr. Esmaielpour, Mr. Brown, Mr. Meleco, Mr. Whitaker, Ms. Fukuda, Ms. Roeth, Mr. Valley for being supportive and helpful.

Thanks should also go to Dr. Debnath, Dr. Mishima, and Dr, Hossain for sample growth and AFM characterization of our InAs/GaAsSb QDs, Dr. Hatch for processing the samples, and Dr. Bumm for the PbS QD synthesis.

I want to give my very special gratitude to my wife Shuai. Without her support, I would not have been able to do any of this.

Thanks to NASA EPSCoR program (Grant(s) #NNX15AM75A, and #NNX13AN01A) for funding these projects. Support is also acknowledged from the state of Oklahoma OCAST program (Grant No. #AR14-041).

Table of Contents

Acknowledgements **iv**

Table of Contents **v**

List of Tables **vii**

List of Figures **viii**

Abstract **xii**

1 Introduction **1**

1.1 Solar Energy and Solar Cell . . . 1
- 1.1.1 Solar Energy Market . . . 2
- 1.1.2 Solar Cell Operating Principles . . . 3
- 1.1.3 Efficiency loss in solar cells . . . 6
- 1.1.4 Three generations of solar cell technologies . . . 8

1.2 Quantum dots . . . 11
- 1.2.1 Introduction . . . 11
- 1.2.2 Colloidal quantum dots and epitaxially self-assembled quantum dots . . . 12

1.3 Intermediate band solar cells . . . 14
- 1.3.1 Basic concept . . . 14
- 1.3.2 Candidate material systems for intermediate band solar cell application . . . 17

1.4 Colloidal quantum dot solar cells . . . 19

2 Characterization Techniques and Experimental Setup **22**

2.1 Transport Characterization . . . 22
- 2.1.1 Current-Voltage Measurements . . . 22
- 2.1.2 External Quantum Efficiency Measurements . . . 27
- 2.1.3 Impedance Measurements . . . 29
  - 2.1.3.1 Capacitance-Voltage measurements . . . 29
  - 2.1.3.2 Impedance Spectroscopy . . . 30
  - 2.1.3.3 Impedance Experimental Setup . . . 30

2.2 Photoluminescence and Electroluminescence Spectroscopy . . . 31
- 2.2.1 Photoluminescence . . . 32
- 2.2.2 Electroluminescence . . . 34

3 Optimization of Growth Conditions for InAs/GaAs$_{1-x}$Sb$_x$ Quantum Dots and Devices **37**

3.1 Growth of InAs/GaAs$_{1-x}$Sb$_x$ Quantum Dots . . . 38
- 3.1.1 Experimental Details . . . 38
- 3.1.2 Experimental Results and Discussions . . . 40
  - 3.1.2.1 Optimization of InAs Deposition Thickness . . . 40
  - 3.1.2.2 Optimization of Sb Composition in GaAs$_{1-x}$Sb$_x$ Matrix 43

3.2 Photoluminescence characterization of Multilayer InAs/GaAs$_{1-x}$Sb$_x$ Quantum Dot Solar Cells . . . 51
3.2.1 Experimental Details . . . 52
3.2.2 Experimental Results and Discussions . . . 53
3.3 Conclusion . . . 63

4 Electrical Characterization of InAs/GaAs$_{1-x}$Sb$_x$ Quantum Dots Solar Cells 66
4.1 Experimental Details . . . 67
4.2 Experimental Results and Discussions . . . 67
4.2.1 Current-Voltage Measurements . . . 67
4.2.2 External Quantum Efficiency Measurements . . . 74
4.2.3 Electroluminescence Measurements . . . 80
4.3 Conclusion . . . 89

5 Investigation of the Non-linearity of the Diode Characteristics in PbS/ZnO Quantum Dot Solar Cells 90
5.1 Experimental Details . . . 91
5.1.1 PbS/ZnO Quantum Dot Thin Film Deposition and Solar Cell Fabrications . . . 91
5.1.2 Characterization techniques . . . 95
5.2 Experimental Results and Discussions . . . 96
5.2.1 Absorption Measurements . . . 96
5.2.2 *Current-Voltage* Analysis . . . 97
5.2.3 Mott-Schottky Analysis . . . 106
5.2.4 Impedance Spectroscopy Analysis . . . 111
5.3 Conclusion . . . 120

6 Summary and Future Work 121

References 127

A Publications and Presentations 148
A.1 List of publications . . . 148
A.2 List of presentations . . . 149

List of Tables

3.1 Activation energies extracted from two activation energy Arrhenius plot fitting of three QD samples. 62

5.1 Parameters extracted from IS fitting. Reprint from Yang et al. *ACS Applied Materials & Interfaces* 9.15 (2017): 13269-13277. 116

List of Figures

1.1 (a) Schematic plot of a p-n junction solar cell structure; (b) band diagram of a simple p-n junction solar cell. 4

1.2 Dark, light J-V and output power curves for an example single junction solar cell. 5

1.3 Thermalization loss (yellow arrow), transmission loss (red arrow), and re-emission loss (green arrow) in a single $p-n$ junction solar cell. 7

1.4 (a) SunPower SPR-X21-345 solar panel (first generation), (b) Hanergy Headquarters Building Integrated Photovoltaics (BIPV) project using CdTe thin film solar panel (second generation), (c) AZUR SPACE TJ 3G30C triple junction GaAs Solar cell (third generation). 9

1.5 Density of states (DOS) for electrons in bulk semiconductors (3-D, blue), quantum wells (2-D, red), quantum wires (1-D, green), and quantum dots (0-D, black). Reprint from *Nanomaterials*, pages 457-583. Springer Netherlands, Dordrecht, 2011. 12

1.6 (a) Cross-section TEM image of the relaxed InSb quantum dot; (b) TEM images of CdSe/ZnS quantum dots. Reprinted from *Thin Solid Films*, 543:74-77, 2013 and *Sensors and Actuators B*: Chemical, 126(1):187-192, 2007. 13

1.7 (a)Schematic band diagram of an IBSC. Two sub-bandgaps within the bandgap E_g, E_H and E_L, are created by the IB. E_H (E_L) generally refers to high (low) energy gap, and represents the energy seperation between CB and IB (IB and VB) in this plot. Absorbed photons pump carriers from *VB* to *CB* (blue arrow), from *IB* to *CB* (green arrow), from *VB* to *IB* (red arrow). The quasi-fermi level (QFL) separation between the *CB* and *VB* determines the output voltage (V). (b) Circuit diagram of an IBSC. 15

1.8 Photoluminescence of CQDs with varying size and composition. Reprint from *Nat Photon*, 7(1):13-23, 2013. 19

2.1 AM 0 (black line), AM 1.5G (red line), and AM 1.5D (green line) reference solar spectra. 23

2.2 Ideal light J-V (black), light J-V with smaller shunt resistance (red), and light J-V with larger series resistance (green). 24

2.3 Equivalent J-V circuit including series and shunt resistances. 25

2.4 J-V experimental setup. 26

2.5 *EQE* experimental setup. 28

2.6 C-V and impedance spectroscopy (IS) experimental setup. 31

2.7 *PL* experimental setup. 33

2.8 *EL* experimental setup. 35

3.1 Schematic plot of optical InAs/GaAsSb QD sample with various InAs deposition thickness. 38

3.2 (a) Schematic band diagram of InAs QDs in a $GaAs_{0.86}Sb_{0.14}$ matrix; (b) AFM image ($1\ \mu m \times 1\ \mu m$) of an uncapped QD layer with 3.0 ML InAs deposition thickness and 13% Sb composition in GaAsSb. 40

3.3 4 K (a) *PL* spectra and (b) normalized *PL* spectra of optical QD samples with 1.5 ML (black), 1.75 ML (red), 3.0 ML (green), and 3.5 ML (blue) InAs deposition thickness. 41
3.4 The QD areal density as a function of InAs deposition thickness. Reprint from M. C. Debnath, Yang et al. published paper *Journal of Applied Physics* 119.11 (2016): 114301. 43
3.5 (a) Schematic plot of optical InAs/$GaAs_{1-x}Sb_x$ QD sample with various Sb composition in $GaAs_{1-x}Sb_x$ matrix; (b) Type-I and type-II band alignments. 44
3.6 (a) PL spectra for QD samples with different Sb compositions in the $GaAs_{1-x}Sb_x$ matrix. A 50 and a 100 multiplier are applied to the 16% and 18% Sb data; (b) Type-I and type-II band alignments. 45
3.7 Temperature dependent *PL* at 4 K from a 3.0 ML InAs/$GaAs_{1-x}Sb_x$ QD structures with Sb compositions of (a) 12% and (b) 16%. (c) PL peak intensity for the 12% (black symbols) and 16% (red symbols) structures as a function of temperature. 47
3.8 Power-dependent PL at 77 K from a 3.0 ML InAs/$GaAs_{1-x}Sb_x$ QD structures with Sb compositions of (a) 12% and (b) 14%. 48
3.9 PL peak positions are shown for the QD structures with 12% (green symbols) and 14% (red symbols) as a function of the cubic root of the excitation power. Reprint from Yang et.al. *Solar Energy Materials and Solar Cells* 147 (2016): 94-100. 50
3.10 The QD areal density as a function of Sb composition in $GaAs_{1-x}Sb_x$ matrix . Reprint from M. C. Debnath, Yang et al. published paper *Journal of Applied Physics* 119.11 (2016): 114301. 50
3.11 Schematic plot of p-i-n GaAs solar cell structures with four different intrinsic region designs: (a) 3 multi-layers, (b) 5 multi-layers, (c) 7 multi-layers of InAs/$GaAs_{0.86}Sb_{0.14}$ QDs, (d) 170 nm $GaAs_{0.86}Sb_{0.14}$. . 52
3.12 4 K Normalized *PL* spectra of the 3 (black symbols), 5 (red symbols), 7 (green symbols) periods QD samples, and the control sample (blue symbols). Peaks related to QD transition and GaAs are labeled. 54
3.13 Power dependent *PL* measurement results of the (a) 3-layer, (a) 5-layer, (a) 7-layer QD cell, and (d) the control cell. 56
3.14 *PL* peak energies are shown for 5-layer (blue symbols) and 7-layer (red symbols) QD samples as a function of the cubic root of the excitation power. 57
3.15 Temperature dependent PL measurement results of the (a) 3-layer, (a) 5-layer, (a) 7-layer QD cells, and (d) the control cell from 4 K to 200 K. 58
3.16 (a) Peak intensity and (b) peak energy as a function of temperature for the 3-, 5-, and 7-layer samples from 4 K to 200 K. 60
3.17 Example of two activation Arrhenius fit for 3-layer QD sample. 62

4.1 (a) 77 K and (b) room temperature *J-V* measurements; solid lines and open symbols represent the light and dark measurements respectively. . 68
4.2 Temperature dependent *J-V* measurements for (a) 3-layer, (b) 5-layer, (c) 7-layer, and (d) control cell from 77 K to 350 K. 70

4.3 Extracted J-V parameters (a) V_{oc}, (b) V_{max}, (c) J_{sc}, (d) J_{max} as a function of temperature; black, red, green, and blue symbols represent the 3-layer, 5-layer, 7-layer and control cells respectively. 72
4.4 77 K (a) linear scale and (b) log scale *EQE* measurements for the 3-layer (black line), 5-layer (red line), 7-layer (green line), and control cells (blue line). 75
4.5 Temperature dependent *EQE* measurements for (a) 3-layer, (b) 5-layer, (c) 7-layer, and (d) control cells from 77 K to 350 K. 77
4.6 *PL* (red line) and *EQE* (black symbols) measurements for (a) control cell and (b) 7-layer QD cell at 150 K; GaAs, $GaAs_{0.86}Sb_{0.14}$, and QDs are labeled as blue, green, and red arrows respectively. 78
4.7 Temperature dependent *PL* (lines) and *EQE* (symbols) measurements for 7-layer QD sample. 79
4.8 Current injection level dependent *EL* measurements for 5-layer QD sample at (a) 77 K (1 - 207 mA), (b) 150 K (1 - 207 mA), and (c) 210 K (1 - 207 mA); (d) The *EL* intensity at 16 mA injection level as a function of temperature. 81
4.9 Injection level dependent *EL* measurements for 7-layer QD sample at (a) 77 K, (b) 150 K, and (c) 210 K; (d) The *EL* intensity at 123 mA injection level as a function of temperature. 82
4.10 PL (red), and EL (green) spectra for 7-layer QD cell at 150 K. 83
4.11 PL (red), and EL (green) spectra for 7-layer QD cell at (a) 77 K, and (b) 210 K. Reprinted from Yang et al. *IEEE JPV* (in press). 84
4.12 (a) $ln(I) - ln(L^{1/2})$ plots for the 7-layer QD sample at various temperatures; (b) z-factors extracted for 5-layer and 7-layer QD samples. . . . 87

5.1 Schematics of (a) photo-lithography mask for patterning ITO substrate and (b) evaporation mask for thermal evaporation of top contact. . . . 92
5.2 Schematic (a) Off-axis and (b) top views of the PbS/ZnO QD solar cells. 94
5.3 PbS/ZnO QD solar cells with exposure masks on for electrical measurements. 95
5.4 PbS/ZnO QD solar cells with exposure masks on for electrical measurements. Reprint from Yang et.al. *ACS Applied Materials & Interfaces* 9.15 (2017): 13269-13277. 96
5.5 (a) Dark and Light J-V measurement results; (b) Zoom in of Dark J-V measurement data, inset is the back to back diode model used to predict this dark J-V behavior. Reprint from Yang et al. *ACS Applied Materials & Interfaces* 9.15 (2017): 13269-13277 97
5.6 One diode model fitting for dark J-V measurements (data - black symbols, fitting - redline); inset is the semi-log plot of dark J-V data. Reprint from Yang et al. *ACS Applied Materials & Interfaces* 9.15 (2017): 13269-13277 99
5.7 Schematic band alignments of both main junction (1) and Schottky diode (2) at equilibrium 101
5.8 Schematic band alignments of both main junction (1) and Schottky diode (2) at forward bias. 102
5.9 Schematic band alignments of both the main junction (1) and Schottky diode (2) at reverse bias. 104

5.10 Schematic plot of defect mediated tunneling mechanism across the PbS/ZnO heterojunction. 105
5.11 (a) C-V and (b) corresponding $1/C^2$-V plot at different sweeping frequencies (black (80 Hz), red (100 Hz), green (250 Hz), blue (500 Hz), and cyan (1 kHz)). Reprint from Yang et al. *ACS Applied Materials & Interfaces* 9.15 (2017): 13269-13277. 108
5.12 *EQE* measurements of a ZnO/TBAI-PbS/EDT-PbS quantum dot solar cell at modulation frequencies (black (97 Hz), red (157 Hz), and green (197 Hz); inset is a zoom in of the *EQE* spectra 111
5.13 Two RC equivalent circuits modeling the back-to-back diodes. 112
5.14 Nyquist plots for impedance spectroscopy measurements under (a) forward and zero bias, (b) reverse and zero bias. Black, red, and green represent the zero, forward, and reverse bias data. Open symbols and lines represent the measurement data and fitting data, respectively. Inset to (a) is a zoom-in Nyquist plot under forward bias. 114

Abstract

During the past century, impacts of climate change on both natural and human systems have been observed worldwide. Numerous scientific investigations suggest a strong correlation between the global warming and greenhouse gas (GHG) emissions. CO_2 emission accounts for 78% of the GHG emissions, and 35% of this CO_2 comes from electricity generation. Reduction of GHG emission from the electricity generation would therefore be beneficial to decrease global warming.

As a renewable energy source, in comparison with conventional fossil fuels, solar energy has limitless supply, is accessible in most geographic locations, and is much cleaner. Currently, solar energy is economically viable in areas where the infrastructure is limited, or the GHG emissions are restricted by policy. To further facilitate the ubiquitous deployment of solar energy on a tera-watt utility scale, further increases in power conversion efficiency and reductions in cost are still required of solar cell technology.

Third generation solar cells are emerging solar cell technologies, which are predicted to operate beyond the Shockley-Queisser limit for single bandgap cells. Nanostructured materials are under investigation as potential candidates for next generation photovoltaic technologies. In this dissertation, one type of nanostructured material, semiconductor quantum dots (QDs), were studied for their potential applications for next-generation photovoltaics.

Epitaxial self-assembled InAs/GaAsSb QD solar cells are investigated for applications as intermediate band solar cells. These systems have a theoretical

efficiency of $\sim 50\%$ with a simple single junction design. Two sets of optical InAs/GaAsSb QD samples grown by Molecular Beam Epitaxy (MBE), one set with various InAs deposition thicknesses, and the other set with different percentages of Sb composition in the barrier, were studied to determine the optimal growth conditions in terms of QD density and uniformity. A deposition thickness of 3 monolayers (ML) and 14% Sb matrix composition were shown to yield uniform QDs with the highest QD density $\sim 3.5 \times 10^{11} /cm^2$ and a quasi-flat valance band alignment.

Four p-i-n GaAs solar cells with different intrinsic region designs were then grown by MBE. An unusually large reduction of the Voc and a complex behavior of Jsc were both observed. A detailed experimental investigation of these devices supports the hypothesis that thermal activation of defects or ionization of impurities in the lattice induces a transition from that dominated by radiative recombination to non-radiative processes. This results in a quenching of the photoluminescence and electroluminescence intensity and a decrease the z-factor from 2 to 1, with increasing temperature. The 1.1% lattice mismatch between the GaAs substrate and GaAsSb matrix contributes to the defect formation, which serves as the main limitation of the performance of InAs/GaAsSb quantum dot solar cells presented in this work.

PbS/ZnO colloidal QD solar cells are investigated for thin film solar cell applications. A suite of transport characterization techniques including current-voltage, capacitance-voltage, and impedance spectroscopy were used to study the effect of the interfaces and intrinsic surface states in a standard ITO/ZnO/PbS/Au

colloidal quantum dot solar cell, without any passivation. An unintentional Schottky barrier formed at the PbS/ZnO interface results in Fermi level pinning and induces a non-linearity in the diode characteristic of this solar cell. Losses associated with Shockley-Reed-Hall recombination processes through interfacial and midgap states associated with the surface states on the PbS QDs contributes to a low minority carrier diffusion length, serving to inhibit the performance of the CQD solar cells.

Chapter 1

Introduction

1.1 Solar Energy and Solar Cell

During the past century, impacts of climate change on both natural and human systems have been observed worldwide. Especially for the last few decades, substantial impacts for physical and biological systems, such as: the shrinkage of glaciers, rising sea levels, and an increase in frequency of severe tropical storms have been attributed to global warming with (high) confidence, based on numerous scientific investigations [1]. The influence of human activities is found to account for much of the dramatic changes of the climate, where greenhouse gas (GHG) emissions are considered likely to be the main reason for global warming since 1950s [1].

According to the Intergovernmental Panel on Climate Change (IPCC)'s Fifth Assessment Report (AR5), "Emissions of CO_2 from fossil fuel combustion and industrial processes contributed about 78% of the total GHG emissions increase from 1970 to 2010, with a similar percentage contribution for the increase during the period 2000 to 2010 (high confidence) [1]." In 2016, the U.S. Energy Information Administration (EIA) reported that 35% of the total U.S. CO_2 emissions can be attributed to electricity generation [2]. Unlike conventional fossil fuels, which take several millions of years to form, have limited reserve, and are geographically concentrated in limited regions, renewable energies such as the sun, wind, rain,

and geothermal heat are accessible in most geographic areas and have limitless supply. Renewable energy is also much cleaner, because of less GHG and pollutant emission. Through incorporation of more renewable energies into electricity generation, better control of GHG emissions is expected, which will benefit the whole world.

1.1.1 Solar Energy Market

Apart from the advantages of less GHG and pollutant emissions, the need for alternative sources of power generation in areas with limited infrastructures or restriction of GHG emissions also makes solar energy potentially economically viable. In 2016, new Global investment in renewable power and fuels was an estimated 241.6 billion USD [3], solar and wind power accounted for 90% of the total investment [3]. Solar energy is the most abundant, renewable, and free energy resource on earth, which makes it a feasible and sustainable alternative to fossil fuels. Compared with 2015, recent investment in solar has declined 34%; however, a market increase of 50% was also observed because of the significant reduction of the manufacturing cost of PV systems [3].

Levelized cost of electricity (LCOE) is a commonly used metric to check the viability of an energy generation technology. It assesses the average total cost per-kilowatthour to build and operate a power generation plant over its lifetime [4]. According to the EIA Levelized Cost and Levelized Avoided Cost of New Generation Resources in the Annual Energy Outlook 2017, the estimated U.S. Capacity-Weighted LCOE for Solar PV plants ($ 58.1/MWh) entering service in

2022 is competitive with conventional fossil fuels (minimum \$ 53.8 /MWh) [4]. In some countries, the actual price of electricity generated by PV is as low as $\sim$ 0.03/kWh [5]. The total deployment of PV is expected to reach at least $\sim$ 3 TW by 2030 [5].

The solar industry is not only becoming a big challenger in the power generation industries, but is also the second highest job creator (373,807) among the whole energy sector in the U.S. at 2016 [6]. The number of new job positions created in the solar industry during 2016 was 737,878 [6] [7], which is close to the total employment of the coal industry for both coal mining and electricity power generation [6].

To increase solar energy accessibly to more areas and population, as well as facilitate the multi-TW scale deployment of PV, it is of great importance to know what limits the achievable efficiency of solar cells to further reduce the cost and increase efficiency. This is the fundamental vision of the work undertaken in the body of the research presented in this thesis. However, the operation principles and efficiency loss in solar cells are briefly explained in the next two sections.

1.1.2 Solar Cell Operating Principles

Photovoltaic (PV) devices convert energy stored in electromagnetic waves into electricity. A solar cell is one type of photovoltaic device which harvests the light from the sun to generate electric energy. The basic operating processes of a simple p-n junction solar cell is shown in Figure 1.1. The majority electrons (holes) in the n-type (p-type) material will diffuse into the p-type (n-type) material and

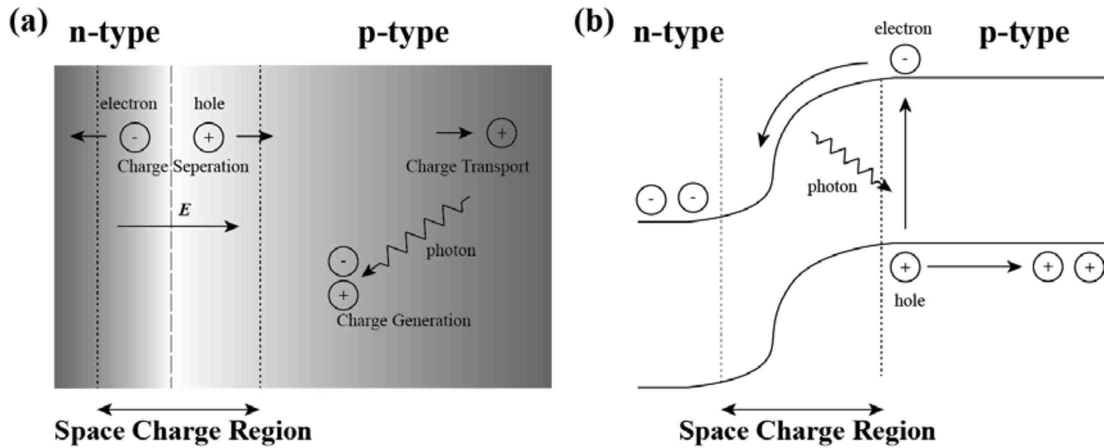

Figure 1.1: (a) Schematic plot of a p-n junction solar cell structure;

(b) band diagram of a simple p-n junction solar cell.

recombine with the holes (electrons), introducing negative (positive) charges in the p-type (n-type) material. Those charges will create a electric field and prohibit further diffusion of majority carriers. The region near the interface of the p-n junction, where the concentrations of the mobile carriers are limited due to the electric field, is defined as the space charge region or depletion region.

There are several requirements for an efficient light-electricity conversion of a solar cell:

Charge generation - photons absorbed by the semiconductor material transfer their energy to the electrons in the valence band, excite electrons to the conduction band, and create electron-hole pairs.

Charge separation - photogenerated electron-hole pairs are separated into electrons and holes through the drift of carriers driven by the electric field in the space charge region (depletion region).

Charge transport - the separated electrons and holes travel in the semiconductor

materials to the opposite terminals.

Electricity output - the electrons run through the external load, recombine with the holes, and return to the ground state.

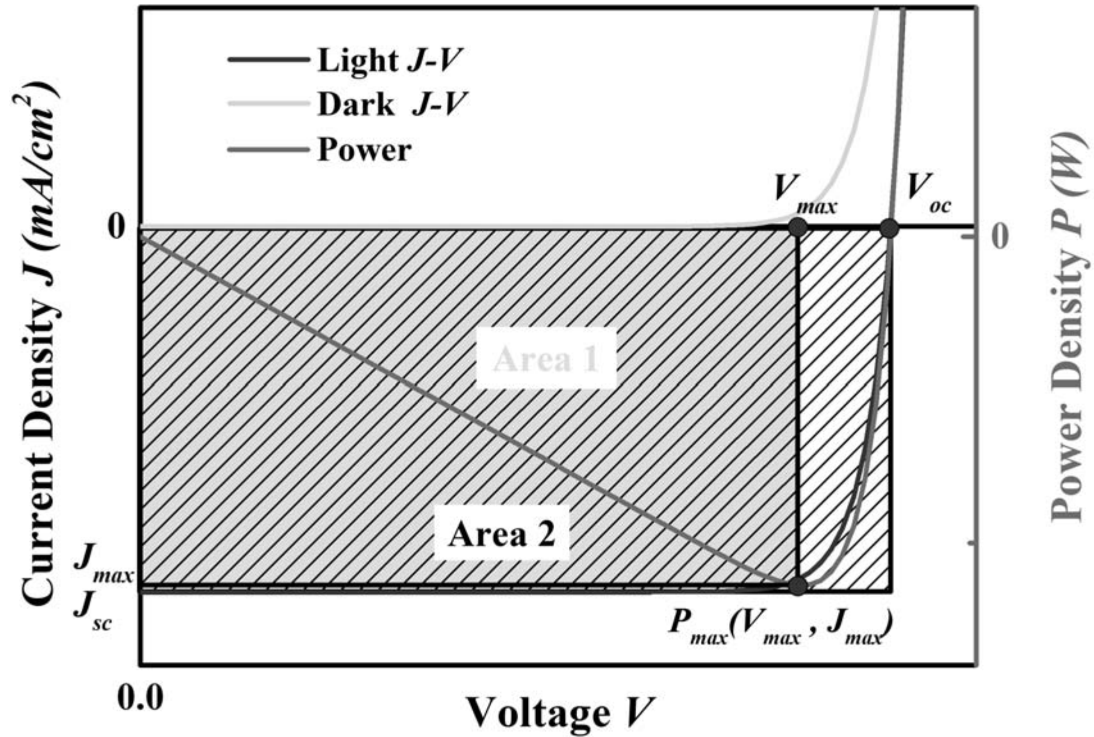

Figure 1.2: Dark, light J-V and output power curves for an example single junction solar cell.

Figure 1.2 shows a plot of dark, light current-voltage (J-V) and output power curves for an example single junction solar cell. Four important parameters open circuit voltage (V_{oc}), short circuit current (J_{sc}), fill factor (FF), and power conversion efficiency (PCE) associated with solar cell operation are directly extracted from J-V measurements.

As shown in Figure 1.2, V_{oc} represents the voltage where the net current flow across the cell is zero and J_{sc} is the current where the voltage across the device is

zero. The maximum output power is determined as

$$P_{max} = J_{max} \times V_{max}. \tag{1.1}$$

FF is used to characterize how well the rectification of the tested solar cell is in comparison with an ideal rectangular $J - V$ curve, and it is determined by

$$FF = \frac{J_{max} \times V_{max}}{J_{sc} \times V_{oc}}. \tag{1.2}$$

Finally, the most important parameter PCE (η) is given by

$$\begin{aligned} \eta &= \frac{J_{max} \times V_{max}}{P_{in}} \\ &= FF \times \frac{J_{sc} \times V_{oc}}{P_{in}}, \end{aligned} \tag{1.3}$$

where P_{in} is the total power per unit area illuminating the solar cell.

1.1.3 Efficiency loss in solar cells

Both the solar spectrum and the semiconductor materials determine photon absorption. Photons with $h\nu_{tr} < E_g$ transmit through the material and introduce the *transmission loss* (red arrow in Figure 1.3). Photons with $h\nu_{ex} > E_g$ will create carriers above the bandgap, those carriers will lose the excess energy to the lattice and generate heat (*thermalization loss* (yellow arrow) in Figure 1.3). Typically, semiconductors with larger (smaller) bandgaps have larger (smaller) open circuit voltages, but have smaller (larger) photocurrents because of the transmission loss. In order to optimize the performance of a solar cell, the transmission loss and thermalization loss have to be balanced. According to Kirchhoff's law of thermal radiation, the photogenerated carriers in the semiconductor materials will also

recombine and result in the spontaneous emission of photons with $h\nu_{em} = E_g$ (*re-emission loss* (green arrow) in Figure 1.3). The maximum efficiency as a function of the bandgap of semiconductor that considers these processes is based a the detailed balanced model known as the Shockley-Queisser limit [8].

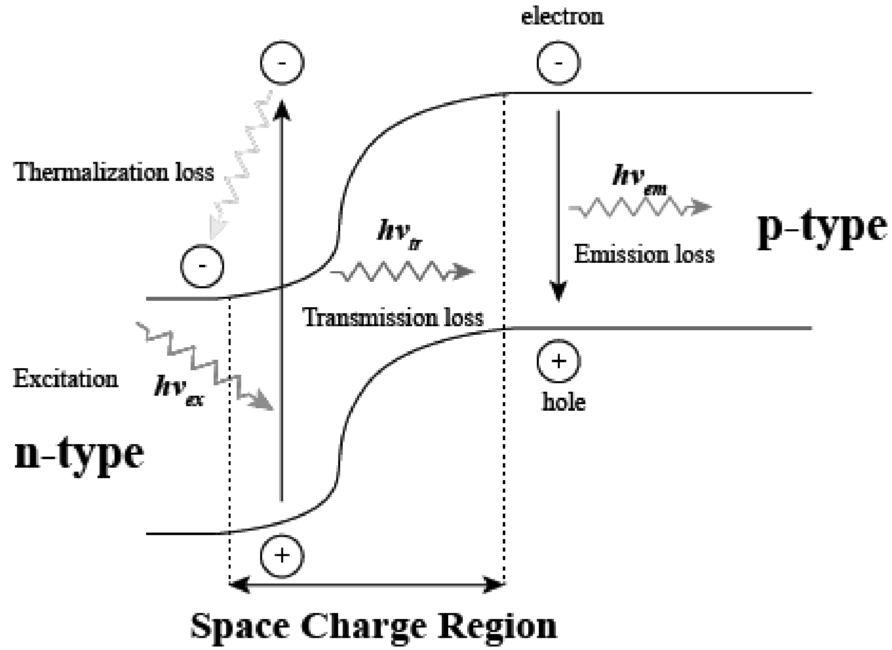

Figure 1.3: Thermalization loss (yellow arrow), transmission loss (red arrow), and re-emission loss (green arrow) in a single $p-n$ junction solar cell.

Apart from these three loss processes, there are two further fundamental losses: a solar cell can be treated as a heat engine doing work between a hot reservoir (the sun) and a cold reservoir (ambient temperature). The maximum efficiency for such a heat engine is determined by the Carnot efficiency $(1 - T_c/T_h)$, this will introduce a *Carnot loss* to the solar cell. The entropy generation during the absorption, conversion, and emission processes will also limit the highest

achievable efficiency (*Black-body limit* [9]). The five losses mentioned above are considered as the fundamental losses of a solar cell [10]. In a practical solar cell, extrinsic losses, such as series resistance, parasitic loss, and non-radiative recombination will further reduce the device efficiency, limiting their performance.

1.1.4 Three generations of solar cell technologies

PV devices are generally classified into three generations [11]:

First generation solar cells - wafer based solar cells - were first introduced by Bell Labs in 1954 [12]. Si wafer based solar cells (monocrystalline Si (mono-Si) and multicrystalline silicon (multi-Si)) are the most successful photovoltaic technology for residential electricity generation due to the abundance of Si in Earth's crust and low manufacturing costs; even though the bandgap of Si is not optimum based on Shockley-Queisser limit [8] in comparison with for example GaAs. The best cell efficiencies for mono-Si and multi-Si are 26.7% [13, 14] and 21.9% [14, 15], respectively. When integrated into modules, the highest efficiencies for mono-Si and multi-Si are reduced to 24.4% [13, 14] and 19.9% [14], respectively. These two technologies accounted for more than 90% of the total PV production in 2016 as reported by the Fraunhofer Institute of Solar Energy in Germany [16]. Figure 1.4 (a) shows a SunPower mono-Si solar cell module. The price of multi-Si cells has seen a significant reduction for the past few years, which has allowed them to obtain 70% of the PV production and become very competitive with conventional fossil fuels.

Second generation solar cells generally refer to thin film solar cells using

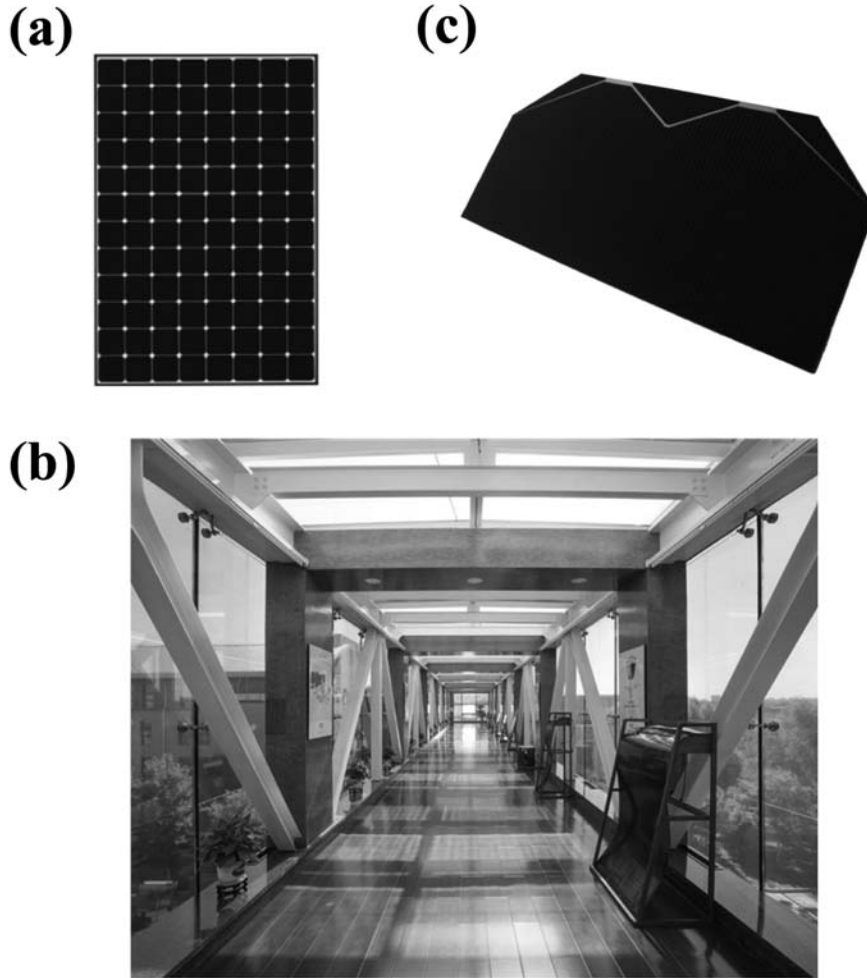

Figure 1.4: (a) SunPower SPR-X21-345 solar panel (first generation), (b) Hanergy Headquarters Building Integrated Photovoltaics (BIPV) project using CdTe thin film solar panel (second generation), (c) AZUR SPACE TJ 3G30C triple junction GaAs Solar cell (third generation).

material systems such as Cu(In,Ga)Se_2, amorphous Si, CdTe, etc. Compared with Si wafer based solar cells, thin film solar cells could potentially offer price reductions in material costs. However, the majority cost of solar panels has shifted to the balance of system (BOS) and inverter technology. For a current commercial rooftop multi-Si solar system, the raw Si and module fabrication now cost less

than 50% of the total system cost [16]. Therefore, module efficiency is of great importance, as higher efficiency means less total solar modules are required (for compatible power output) and therefore, lower installation costs. Thus, the low cost of materials is not an advantage for thin film solar cell anymore.

Currently, the market share for thin film solar cells is less than 10%. Instead, flexible substrates, which along with the capability of being semitransparent and colorful, make thin film solar cells suitable for specific applications such as windows and decorative solar panels. An example of building integrated photovoltaics (BIPV) using semi-transparent CdTe solar cells is shown in Figure 1.4 (b).

Third generation solar cells are generally referred to as emerging solar cell tehcnologies which are predicted to operate beyond the Shockley-Queisser limit for single bandgap solar cells [8]. The most successfully commercialized third generation technology is multijunction solar cells, which stack several materials with different energy gaps to increase the total absorption of the solar spectrum and reduce thermalization and transmission losses. Figure 1.4 (c) shows a AZUR SPACE TJ 3G30C triple junction GaAs based solar cell. By using concentrators, the efficiency loss related to the entropy generation in absorption and emission processes may also be reduced. The highest achieved efficiency record for a multijunction solar cell is 38.8% under 1 sun [17], 46% under 508 suns [18], and 38.9% for modules under 333 suns [19]. However, due to the use of expensive materials and synthesis equipment costs incorporated in the production process, multijunction solar cells are predominantly used in places where the priority is efficiency rather than unit cell price such as, space applications and concentrator

PV (CPV) systems.

Emerging techniques for solar cell applications focus on delivering high efficiency solar cells at relatively low cost. Several developing techniques including multi-exciton generation (MEG), hot carrier solar cells, and intermediate band solar cells (IBSC) could potentially offer much higher power conversion efficiencies at less cost.

Nanostructured materials have been investigated extensively for third generation photovoltaic applications [14, 20]. Multiple quantum wells (MQWs) have been successfully used in 4 junction solar cells, achieving a 46% efficiency under 508 concentration [18]. In this dissertation, another type of nanostructured material, quantum dots (QDs), are studied for their potential applications for next-generation photovoltaics. Since this dissertation focuses on QD solar cells, the concept of QDs will now be briefly introduced and discussed.

1.2 Quantum dots

1.2.1 Introduction

Quantum dots (QDs) typically refer to semiconductor materials with excitons confined in all three spatial dimensions (on the order of the bulk semiconductor's Bohr exciton radius, i.e. 10's of nm). The band structure of QDs is analogous to the simple quantum mechanics model - "a particle in a box", where the electron wave is confined in a 3-dimensional infinitely deep potential well. By solving the Schrödinger equation, the density of states (DOS) in QDs is a δ-

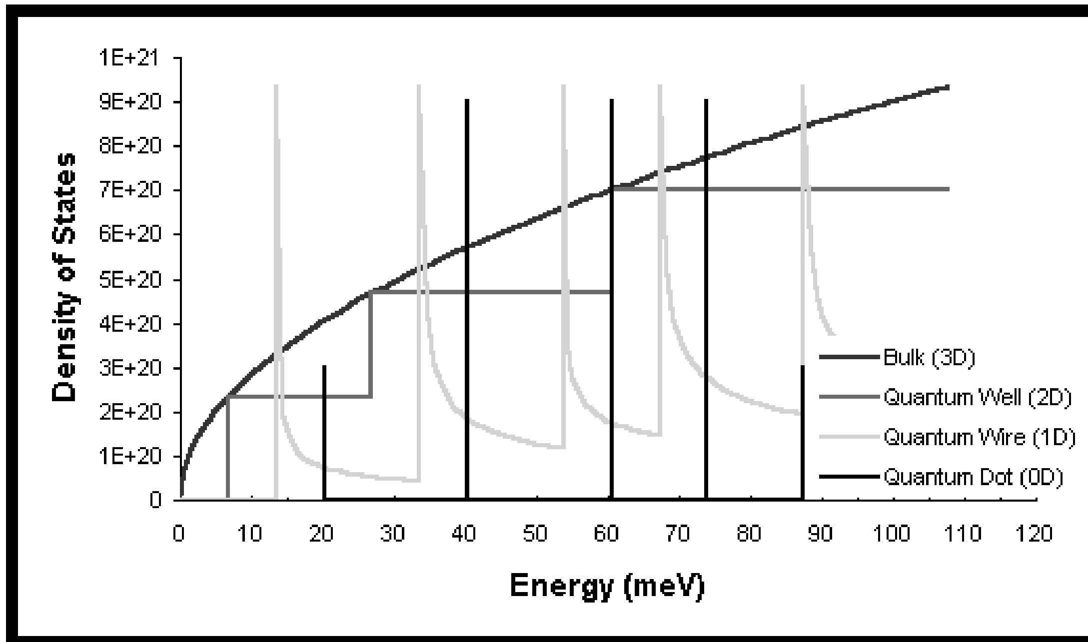

Figure 1.5: Density of states (DOS) for electrons in bulk semiconductors (3-D, blue), quantum wells (2-D, red), quantum wires (1-D, green), and quantum dots (0-D, black). Reprint from *Nanomaterials*, pages 457-583. Springer Netherlands, Dordrecht, 2011. [21].

function [22], which leads to quantized and discrete energy levels similar to that of atomic and molecular energy states (see Figure 1.5 black line). The optical and electric properties can be therefore finely controlled by simply varying the spatial dimensions of QDs [23].

1.2.2 Colloidal quantum dots and epitaxially self-assembled quantum dots

Typically, there are two techniques in QD synthesis: chemical synthesis and self assembled epitaxy, which is most often Stranski-Krastanov (SK) growth [23]. Based on the different synthesis routines, QDs can be divided into two broad

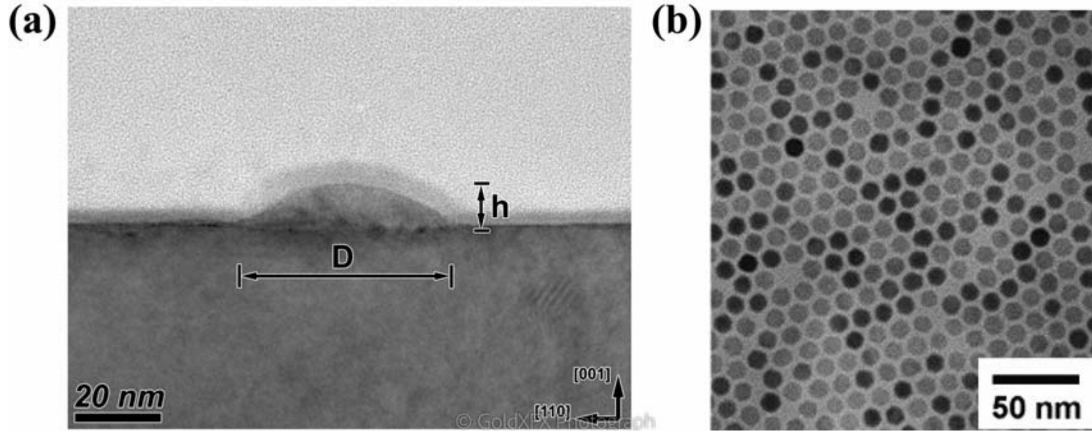

Figure 1.6: (a) Cross-section TEM image of the relaxed InSb quantum dot; (b) TEM images of CdSe/ZnS quantum dots. Reprinted from *Thin Solid Films*, 543:74-77, 2013 [24] and *Sensors and Actuators B*: Chemical, 126(1):187-192, 2007 [25].

categories: colloidal QDs (CQDs) and epitaxially self-assembled QDs. Examples of self-assembled QDs and colloidal QDs are shown in Figure 1.6.

CQDs are synthesized by injecting cation and anion precursors (typically metal-organic reagents) to an organic coordinating solvent. The anion/cation precursors decompose at relatively high temperature, and after reaching the supersaturation state, they will react to form nuclei. The nuclei keep growing into small crystallites until the cation/anion precursors are used up or stopped by rapid cooling below the reaction temperature [23].

Self-assembled QDs are usually grown by molecular beam epitaxy (MBE). In this systems, a lattice-mismatched material is deposited on top of another material, a uniform layer whereby a 2D strained epilayer referred to as a wetting layer is formed. As the thickness of the wetting layer reaches a critical thickness,

the strain energy built up between the two lattice-mismatched materials triggers the spontaneous nucleation of island-like QDs (see Figure 1.6(a)) [23].

In comparison with epitaxially grown self-assembled QDs which are typically produced by MBE in an ultra-high vacuum environment, chemically synthesized CQDs have larger production yields and higher impurity tolerances. The free-standing CQDs are easy to apply post-treatment and purification processes upon to further enhance the spectral purity through improvement of both the size and shape uniformity. Moreover, CQDs have high photoluminescence quantum yields (η_{pl}). All these advantages have led to the commercialization of CQD based television displays [26]. Compared with CQDs, the crystal quality of self-assembled QDs is higher, which results in better electrical and optoelectrical performance, making them suitable for laser applications [27].

In this dissertation, two different types of QDs were investigated for photovoltaic applications; epitaxially grown QDs for high efficiency IBSCs and low cost colloidal QDs for quantum dot thin film solar cells. In both cases, there are plenty of issues limiting the applications of the technologies. The focus is to study the complementary physics behind those limiting factors, in both systems.

1.3 Intermediate band solar cells

1.3.1 Basic concept

The concept of IBSC was first introduced by Antonio Luque and Antonio Martí in 1997 [28], where an intermediate energy level is introduced into the bandgap

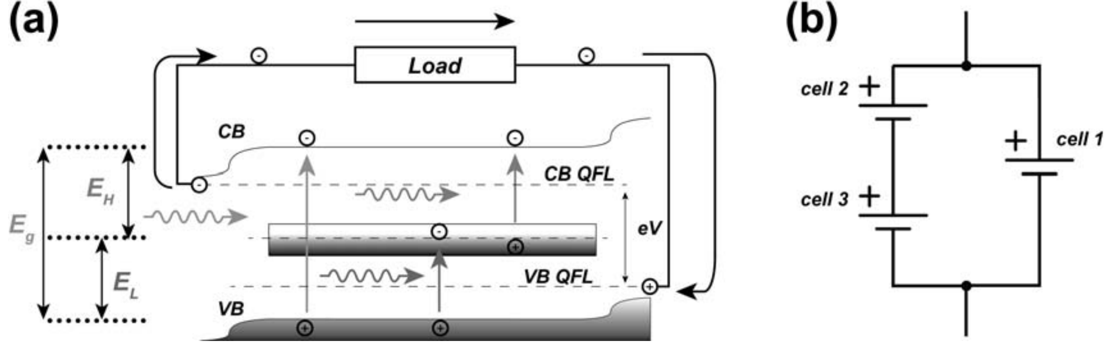

Figure 1.7: (a)Schematic band diagram of an IBSC. Two sub-bandgaps within the bandgap E_g, E_H and E_L, are created by the IB. E_H (E_L) generally refers to high (low) energy gap, and represents the energy seperation between CB and IB (IB and VB) in this plot. Absorbed photons pump carriers from VB to CB (blue arrow), from IB to CB (green arrow), from VB to IB (red arrow). The quasi-fermi level (QFL) separation between the CB and VB determines the output voltage (V). (b) Circuit diagram of an IBSC.

of a conventional single junction solar cell. The schematic band diagram of an IBSC is shown in Figure 1.7(a). A half filled intermediate band (IB) lies between the valence band (VB) and the conduction band (CB), and introduces two sub-bandgaps E_H and E_L (Figure 1.7); where E_H and E_L represent the larger and smaller energy separations, respectively. In addition to absorption of photons with $h\nu$ ($> E_g$), sub-bandgap photons with $h\nu > E_H$ or $> E_L$, are also absorbed through a transition from the IB to CB (green arrow in Figure 1.7) or from the VB to IB (red arrow in Figure 1.7). The concept of IBSCs is analogous to 3-stage multijunction solar cell, which uses semiconductors with 3 different energy gaps to absorb a larger range of the solar spectrum. Unlike the 3-stage multijunction

solar cell acting as a 3 solar cells in series, IBSC works as a solar cell in parallel with 2 solar cells in series (Figure 1.7(b)).

There are two important characteristics for IBSC operation:

Two-step photon absorption (TSPA) - The IB materials are sandwiched by two conventional n- and p-type semiconductors, which serve as selective contacts to electrons and holes in the CB and VB. The IB is isolated from the contact, therefore no sub-bandgap photocurrent will be generated from a single transition VB to IB or IB to CB unless a two-step transition occurs. TSPA occurs when a sub-bandgap photon pumps a electron from VB to IB and subsequently another sub-bandgap photon pumps a electron from IB to CB. Thus, the total generated photocurrent is a combination of photocurrent from the direct VB-CB transition and photocurrent from the TSPA.

Voltage preservation - For conventional single junction solar cells, the photocurrent can be increased by choosing the semiconductor materials with smaller bandgaps, but with a trade-off of low output voltage (typically $\sim V_{max}$). However, the output voltage in an IBSC remains determined by the quasi Fermi level separation between the n- and p- type materials, since the IB is isolated from VB and CB; therefore, for an IBSC, the voltage is preserved with an increased photocurrent.

The optimum theoretical efficiency of an ideal IBSC is 63% under a concentration of 46,050 suns based on a detailed balance model [28], which is significantly higher than the Shockley-Queisser limit of 41% for a conventional single junction solar cell under the same concentrated illuminations [28–30].

1.3.2 Candidate material systems for intermediate band solar cell application

The techniques that have been applied to create the IBSC can be divided into three broad categories [29–32]: QDs, highly mismatched alloys (HMAs), and bulk semiconductors with deep level impurities (DLI).

Quantum dots - QDs are a candidate system for an IBSC because of the discrete energy levels introduced by the 3-dimensional quantum confinement effects; and semiconductor QDs are the most well investigated technologies for IBSC applications [33–47]. As the most well-established material systems for IBSC application, InAs/GaAs QD solar cells (QDSCs) have been used to demonstrated the existence of sub-bandgap transitions (E_H and E_L) [43–45] and the photocurrent enhancement related to TSPA [39, 46, 47]. However, the TSPA process is very weak ($< 1\%$) at room temperature and voltage preservation [48] is only achieved at low temperature [31, 32], due to the efficient carrier escape processes (tunneling and thermal escape) at relatively high temperatures ($> 70K$) [32].

Highly mismatched alloys - HMAs refer to semiconductor alloys composed of semiconductor materials with distinctly different electronegativities. Normally, the bandgap of semiconductor alloys can be estimated by the linear interpolation of the compositions of the endpoint materials A and B based on the virtual crystal approximation (VCA) as described in reference [49]. However, due to the dramatic mismatch of HMAs containing component elements, the standard VCA theory deviates from the experimental results. For instance, incorporating 1% N into

GaAs will reduce the bandgap by more than 0.1 eV [50].

A band anticrossing (BAC) model is used to explain the band structure of HMAs, where the conduction band is reconstructed into E_+ and E_- because of the anticrossing interaction between the extended states of the host materials and the highly localized states introduced by the substitutional atoms (eg. N in GaAs, and O in ZnTe) [51, 52]. The resulting energy state E_- will serve as the IB. TSPA process has been observed in both GaNAs [53, 54] and ZnTeO [55, 56] material systems.

Bulk semiconductors with deep level impurities - In general, deep levels introduced by normal impurities will serve as non-radiative channels (eg. Shockley-Read-Hall recombination). The increased dark saturation current in terms of non-radiative recombination current reduces the open-circuit voltage and eliminates the benefits of improved photocurrent related to absorption of sub-bandgap photons. Dilute magnetic semiconductors (DMS), which have been investigated extensively for spintronics applications have been proposed for IBSC applications since, the recombination through the IB formed by the spin-degeneracy is forbidden by the spin selection rules. Both GaN with Mn impurities [57] and GaAs with implanted Ti [58] show photocurrent from the sub-bandgap transition. Voltage preservation has also been seen in a GaAs:Ti IBSC prototype [58].

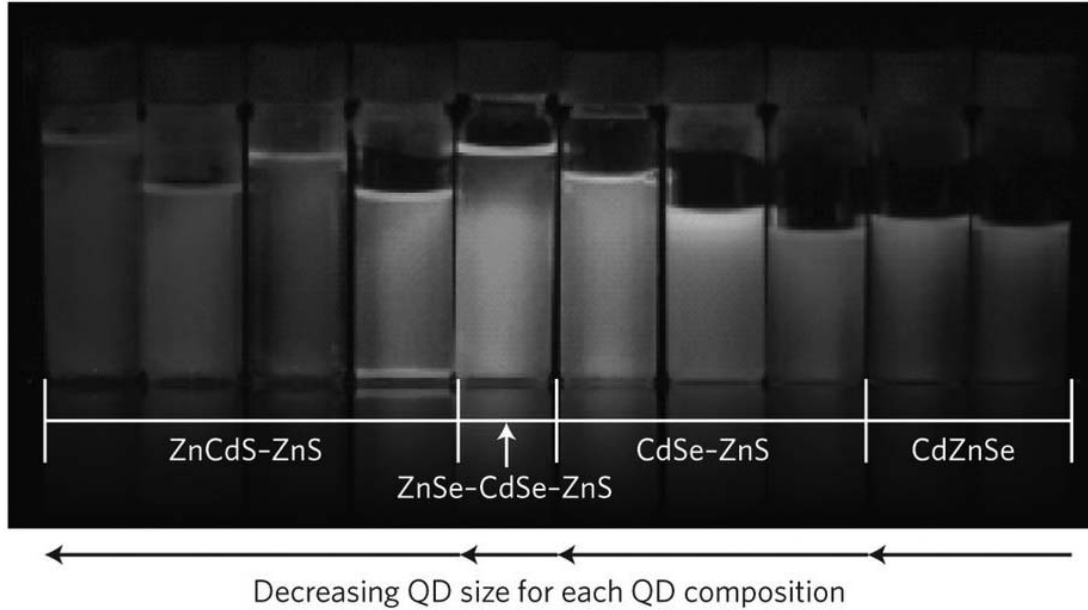

Figure 1.8: Photoluminescence of CQDs with varying size and composition. Reprint from *Nat Photon*, 7(1):13-23, 2013 [59].

1.4 Colloidal quantum dot solar cells

An alternative technology utilizing QDs for solar cell applications is CQD thin film solar cells. Incorporation of solution and low temperature synthesis techniques could significantly decrease the manufacturing cost of solar cells. CQDs have been studied extensively for solar cell applications due to their exceptional bandgap tunability from quantum confinement effects. Chemistry fabrication allows easy manufacture of CQDs without the requirement of expensive techniques such as: high temperature processes and ultra-high vacuum environment. The absorption and emission of CQDs can be easily tuned during the synthesis process by controlling reaction time and temperature. Figure 1.8 shows the photoluminescence of CQDs with different compositions and sizes, illustrating the large bandgap

tunability of these systems.

Among the many CQD material systems, lead chalcogenide QDs (PbS [60–63], PbSe [64, 65]) represent a promising candidate for solar cell applications for their capability of optimized solar spectra overlap and incorporation of multiple exciton generation (MEG) [66, 67], as well as, a tandem structure [68].

Multiple exciton generation is a process that one absorbed photon generates two or more electron-hole pairs in nanostructured materials, which is similar as the impact ionization in wide bandgap bulk semiconductor materials. MEG processes in QDs occur at the photon energies of ~ 3 eV [67], which is considerably lower than the typical impact ionization process (~ 7 eV) [67]; this is due to the atomic like energy levels of QDs decoupling of phonon processes, and their superior bandgap tunability. The Beard-group at NREL has demonstrated a PbSe QD solar cells achieving a peak external quantum efficiency (EQE) over 110% [67], via MEG suggesting this process could potentially enable power conversion efficiency (PCE) in excess of the Shockley-Queisser limit.

Multijunction solar cells, despite being the most efficient solar cells in the market, have high fabrication costs limiting their mass production and deployment. Solution processed CQDs with size-tunable bandgaps offer another approach to break the Shockley-Queisser limit by incorporating ***tandem multijunction structures***. By utilizing multiple absorber layers with cascading energy gaps, researchers have demonstrated CQD solar cells with enhanced open circuit voltages [69]. This can be done in several ways, for example: using different CQD materials, the same CQD material with various sizes, or a combination of the two. Intensive

research efforts continue to make CQD solar cells more efficient. Currently, the best power conversion efficiency (PCE) for a CQD solar cell has reached 11.4% with good stability using PbS [70].

Chapter 2

Characterization Techniques and Experimental Setup

In this chapter, a suite of experiments used in this research is described in detail. First, transport measurements including: current-voltage measurements (J-V), external quantum efficiency (EQE) measurements, capacitance-voltage (C-V), and impedance spectroscopy (IS) measurements are introduced. Then, the basic theory and experimental setup for both photoluminescence (PL) and electroluminescence (EL) measurements are presented.

2.1 Transport Characterization

2.1.1 Current-Voltage Measurements

J-V measurements are one of the most well used and important techniques for solar cell characterization. As is described in Chapter 1, several important parameters including V_{oc}, J_{sc}, FF, and PCE associated with a solar cell's operation can be directly extracted from J-V measurements.

To make the performance of various solar cells comparable, a well defined solar spectrum is needed to determine the P_{in}. The standard solar reference spectra for solar cells and modules characterization is documented in ASTM E-490-00 (AM 0) [71] and ASTM G-173-03 (AM 1.5G and AM 1.5D) [72] and shown in Figure 2.1.

The Air Mass (AM) 0 spectrum represents the solar spectrum outside the

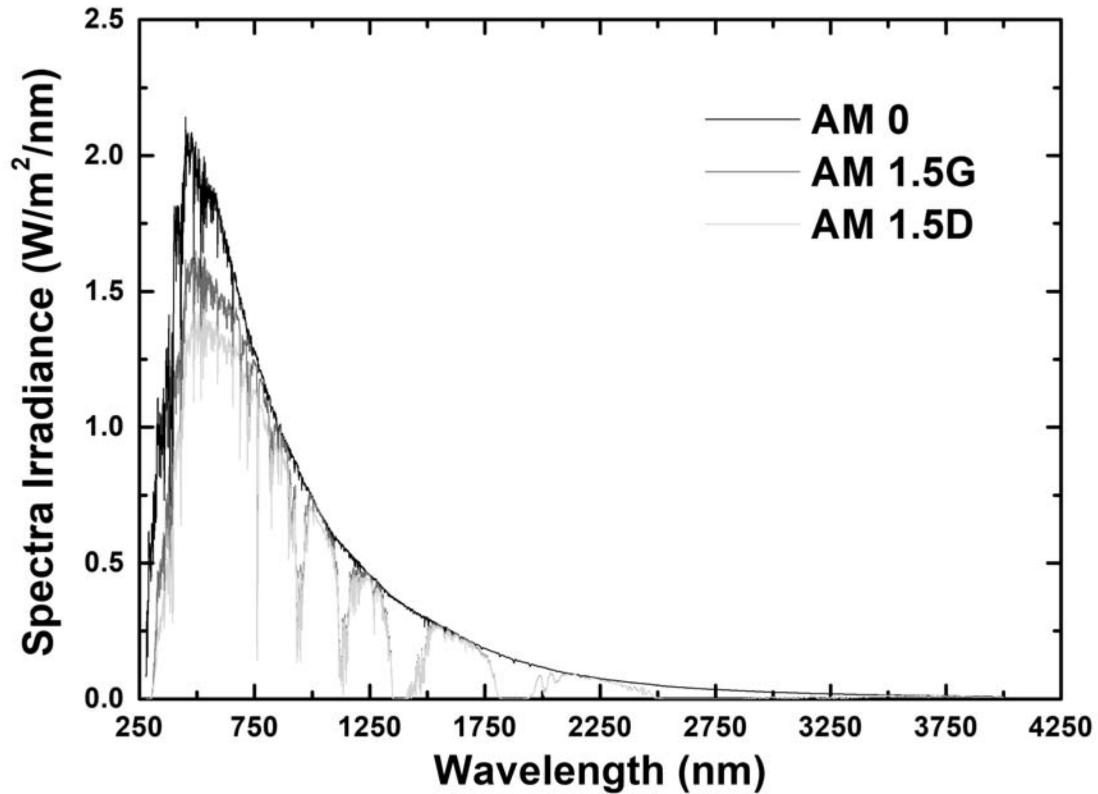

Figure 2.1: AM 0 (black line), AM 1.5G (red line), and AM 1.5D (green line) reference solar spectra.

atmosphere and is used for satellite applications. AM 1.5G and AM 1.5D are standards for terrestrial applications, where AM 1.5G includes both direct and diffuse light, and AM 1.5D spectrum only includes direct light. The total power P_{in} per unit area for AM 0, AM 1.5G, and AM 1.5D are 1366.1 W/m^2, 1000 W/m^2, and 888 W/m^2, respectively. The AM 1.5G standard is used throughout the light J-V measurements in this dissertation.

The light J-V characteristic of an ideal single junction p-n solar cell (see black line in Figure 2.2) is a superposition of an ideal dark J-V curve and constant

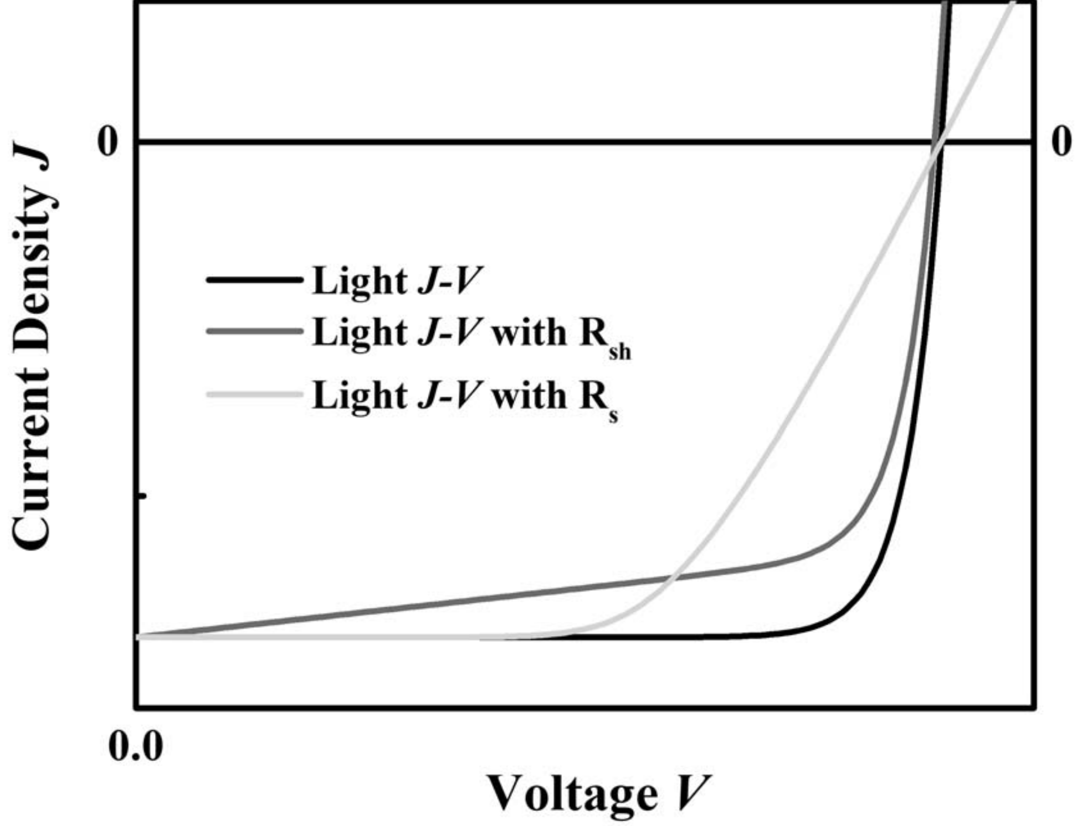

Figure 2.2: Ideal light J-V (black), light J-V with smaller shunt resistance (red), and light J-V with larger series resistance (green).

current source J_P. It is written as:

$$J = J_0 \cdot [exp\ (\frac{qV}{nk_BT}) - 1] - J_P, \tag{2.1}$$

where J_0, n, q, k_B, and T represent dark saturation current density, ideality factor, unit charge, Boltzmann constant and temperature, respectively.

If parasitic resistances, for instance, series and shunt resistances are taken into account, Equation 2.1 is re-written as:

$$J = J_0 \cdot [exp\ (\frac{q(V - JR_s)}{nkT}) - 1] + \frac{V - JR_s}{R_{sh}} - J_P, \tag{2.2}$$

where R_s and R_{sh} are the series and shunt resistance, respectively. An equivalent

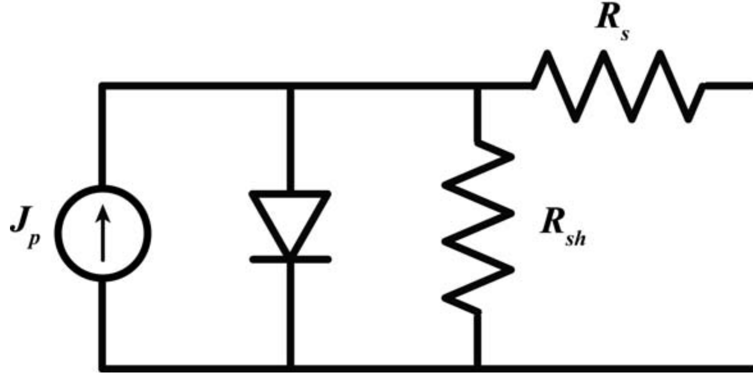

Figure 2.3: Equivalent J-V circuit including series and shunt resistances.

circuit describing the operation of a solar cell and incorporating parasitic losses is shown in Figure 2.3.

Parasitic resistances dissipate the solar energy into heat instead of electricity and reduce the PCE of the solar cells. The influence of the shunt resistance is illustrated in Figure 2.2 (red line). The shunt resistance will introduce a leakage path and affect the collectable current throughout the whole range of the working bias. For an ideal solar cell, the shunt resistance is close to infinity. In reality, the smaller the shunt resistance, the larger the leakage current.

The series resistance, which reflects the opposition to current transport through the device, will result in a voltage drop across the output terminals due to the voltage division of this resistance, which is reflected in a reduction of the operating voltage and FF as shown in the Figure 2.2 (green line). However, the series resistance will not affect V_{oc} due to the lack of current running through the terminals. The photocurrent J_P compensates the diode dark current, therefore no reduction of the V_{oc}.

Current-Voltage Experimental Setup

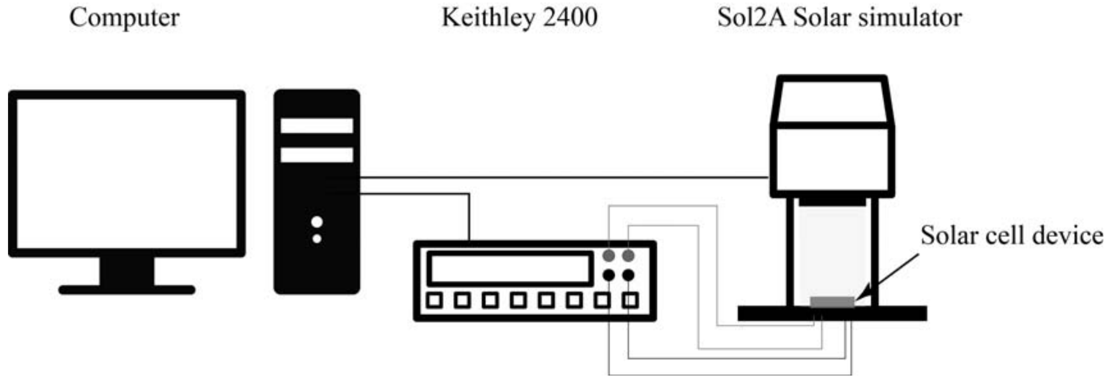

Figure 2.4: J-V experimental setup.

The experimental setup for J-V measurements is shown in Figure 2.4. A Keithley 2400 multimeter is used to apply a bias and measure the resulting current. Current density is calculated from the measured current I divided by the device area or illuminated area through the mask (eg. the mask used in Chapter 5). A Newport Oriel Sol2A (model 94022A) solar simulator is used to provide an AM 1.5G solar spectrum. The illumination power density is calibrated with a Si reference cell. The InAs/GaAsSb QD solar cells described in in Chapter 3 & 4 and the PbS/ZnO QD heterojunction discussed solar cells in Chapter 5 were mounted and connected in the Linkam THMS600 cryostat. For temperature dependent measurements from 77 K to 350 K, a Linkam LNP95 cooling system including a liquid nitrogen dewar, a liquid nitrogen pump, and a T95 temperature controller were used. The cryostat is sealed tight at first; then, N_2 was used to purge air out of the cryostat and attain an oxygen- and moisture-free environment; after the purging process, the sample is cooled down to 77 K to begin the temperature

dependent measurements.

2.1.2 External Quantum Efficiency Measurements

External quantum efficiency (EQE) of a device is written as:

$$\begin{aligned} EQE(\lambda) &= \frac{current\ /e}{incident\ power/photon\ energy}\,(\lambda) \\ &= \frac{collected\ carriers\ (device)}{collected\ carriers/\ Spectral\ response\ (detector)}\,(\lambda), \end{aligned} \tag{2.3}$$

which is determined as the ratio of the collected photogenerated carriers to the number of incident photons as a function of wavelength. If one incident photon gets absorbed and one carrier is extracted, the resulting EQE is 100%. Since EQE is also directly related to the absorption spectrum, it can also be used to determine the bandgap of the solar cell and the contribution of the photogenerated current from different materials in the device.

In J-V measurements, J_{sc} is photogenerated current per area at zero bias. Therefore, the equivalent J_{sc} can also be extracted from the EQE measurements across the solar spectrum at zero bias by:

$$J_{sc} = q \int \Phi_0(\lambda) EQE(\lambda) d\lambda, \tag{2.4}$$

where q and Φ_0 represent the charge and photon flux, respectively.

External Quantum Efficiency Experimental Setup

The EQE experimental setup is shown in Figure 2.5. A Quartz Tungsten Halogen (QTH) lamp (model Oriel 66884) and a Xenon arc lamp (model Oriel 66092) are used as light sources to cover visible and infrared spectrum. An Oriel Merlin

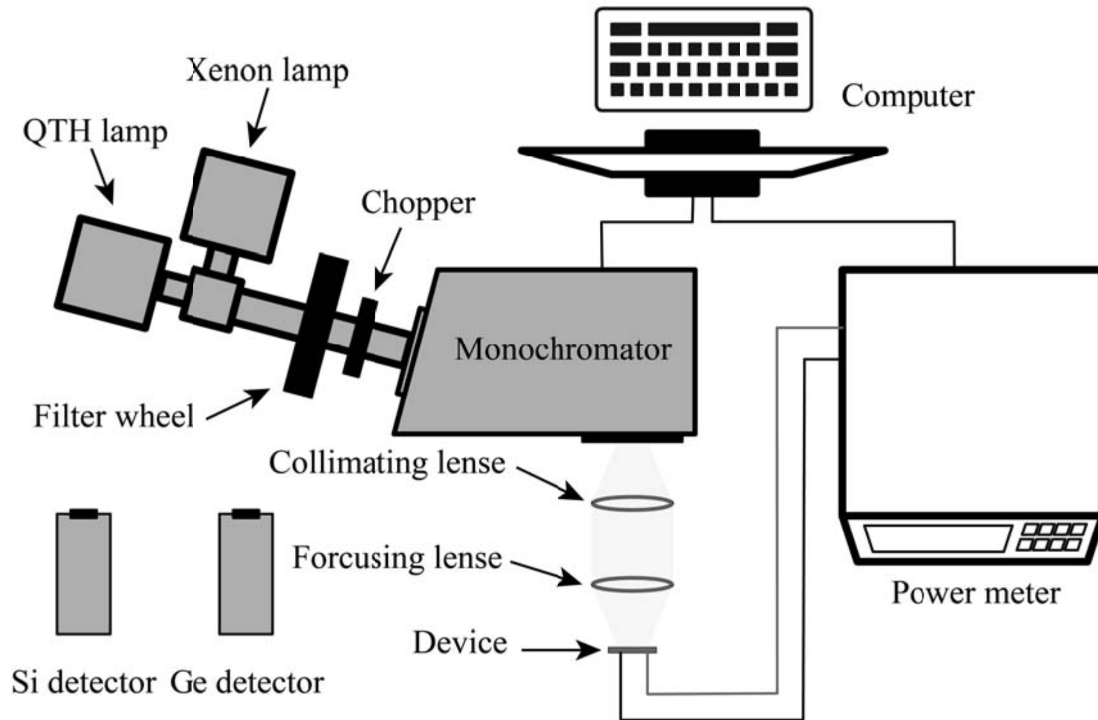

Figure 2.5: *EQE* experimental setup.

Digital Lock-in radiometry system, including a filter wheel with three long pass filters (305, 550, and 1000 nm), a chopper (1 - 200 Hz) and an Oriel Cornerstone 260 monochromator, are used to provide chopped monochromatic light. Two lenses are used to collimate and focus the light onto the sample. Two detectors, Si detector (model Oriel 71650) and Ge detector (model Oriel 71653), are used to measure the reference spectrum from 400 nm to 1100 nm and from 700 nm to 1700 nm, respectively. For temperature dependent *EQE* measurements, the same Linkam system used in temperature dependent *J*-*V* measurements is used.

2.1.3 Impedance Measurements

The concept of impedance was first introduced by Oliver Heaviside in 1886 [73]. In analogy to resistance under DC conditions, impedance reflects the ability of a component to inhibit the current flow with given AC bias. The impedance of a system is defined as applied AC voltage $V(t)$ divided by the resulting current $I(t)$:

$$Z = \frac{V(t)}{I(t)}. \tag{2.5}$$

By measuring the amplitude and phase of the response of a small modulation signal, the impedance Z is determined as $Z = |Z|e^{j\omega\phi}$, where j is the imaginary unit, ω is the angular frequency, and ϕ is the phase angle. For three ideal fundamental components: resistor R, capacitor C, and inductor L, each impedance is defined as $Z_R = R$, $Z_C = \frac{1}{j\omega C}$, and $Z = j\omega L$, respectively.

2.1.3.1 Capacitance-Voltage measurements

The C-V measurements described in Chapter 4 are also referred to as Mott-Schottky analysis. The capacitance of a Schottky junction is analogous to the capacitance of a parallel-plate capacitor, with capacitance given by:

$$C = \frac{A\epsilon_s}{\omega}, \tag{2.6}$$

where ω is the depletion region formed by the diffused minority carriers, and the associated built-in potential is V_{bi}. The depletion width of a Schottky junction is given by [74]:

$$\omega = \sqrt{\frac{2\epsilon_s(V_{bi} - V)}{qN_{D,A}}}. \tag{2.7}$$

Parameters N_D or N_A represent the donor or acceptor concentration in the semiconductor, respectively. Combining Equation 2.6 and 2.7, the capacitance of a Schottky junction can be written as:

$$C = A\sqrt{\frac{q\epsilon_s N_{D,A}}{2(V_{bi} - V)}}, \tag{2.8}$$

or

$$\frac{1}{C^2} = \frac{2(V_{bi} - V)}{A^2 q\epsilon_s N_{D,A}}. \tag{2.9}$$

By plotting $1/C^2$ - V, the doping concentration N_D or N_A and built-in potential V_{bi} can be determined from the slope and intercept of a linear fit, respectively. For heterojunctions, if the doping concentration on one side of the interface is much higher than the other, the capacitance can still be approximated by Equation 2.9.

2.1.3.2 Impedance Spectroscopy

A Nyquist plot, is used to interpret the impedance spectroscopy (IS) in which the imaginary part of impedance Z'' is plotted against the real part of the impedance Z', as a function of modulation frequency ω. The minority carrier lifetime and diffusion length can therefore be determined from the recombination resistance, transmission resistance, and chemical capacitance, which are all extracted directly by fitting the Nyquist plot with an appropriate equivalent circuit model model.

2.1.3.3 Impedance Experimental Setup

Capacitance and impedance measurements were taken with Hewlett Packard 4192A LF impedance analyzer. This impedance analyzer is capable of bias and

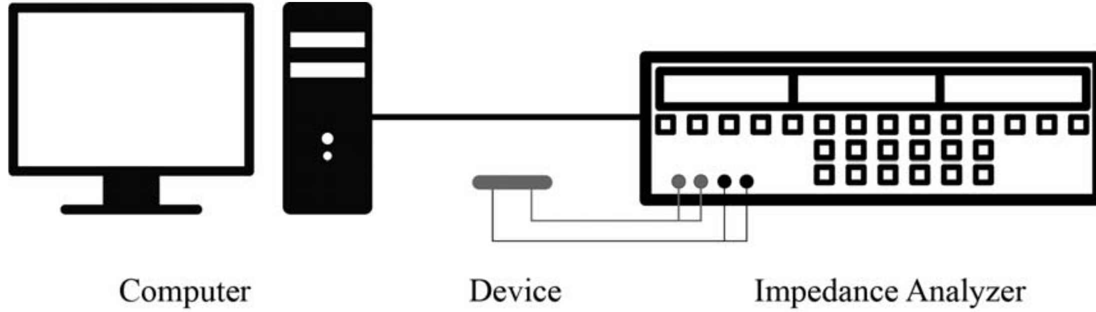

Figure 2.6: C-V and impedance spectroscopy (IS) experimental setup.

oscillation frequency dependent measurements. The impedance measurements setup is shown in Figure 2.6. The AC oscillation voltage amplitude is set to 20 mV root-mean-square (on the order of kT/e) to achieve an approximate linear response $Z(\omega) = V(\omega)/I(\omega)$ [75] for both C-V and IS measurements. The sweeping frequency range for IS measurements was set from 10 Hz to 13 MHz. However for the C-V measurements discussed in Chapter 4, a relatively low frequency range of 80 Hz to 1000 Hz was chosen due to the relatively slow response of the devices.

2.2 Photoluminescence and Electroluminescence Spectroscopy

Luminescence spectroscopy is a powerful technique for semiconductor characterization. This non-destructive technique is used to study band structures of the materials and defects that have an energy that is close to the band edge. After exciting the carriers above the bandgap, the excited carriers will eventually relax back to the valence band states through multiple processes. Luminescence spectroscopy is used to study the radiative recombination of the excited carriers

in the semiconductor material.

Based on different excitation methods, the luminescence spectroscopy includes photoluminescence, electroluminescence, cathodoluminescence, thermoluminescence, etc. In this dissertation, photoluminescence and electroluminescence were used to characterize and investigate the fundamental properties of the quantum dot solar cells.

2.2.1 Photoluminescence

Photoluminescence (*PL*) measures the light emitted from the radiative recombination of photo-excited carriers in a material. *PL* is a non-destructive optical measurement and therefore doesn't need a full electrical device architecture. The excitation source is typically a laser that has a photon energy larger than the bandgap of the probed material. The semiconductor material will absorb the photons, pump the electrons above the conduction band, and generate electron-hole pairs. The photo-excited electrons and holes will relax rapidly to the local extrema of the energy states (typically the CB and VB band edge for bulk materials) within the conduction and valence bands, then subsequently recombine through radiative or non-radiative processes. The radiative portion is measured by the photodetector, yielding information about bandgap of materials and defects.

By investigating the shape, peak position, and intensity of the *PL* spectra at various temperatures (TD *PL*), additional information of the material such as: the nature of the optical transition (bandgap or defects induced localized states), activation energies, relative strength of non-radiative recombination, etc. can be

determined. By varying the excitation power, information related to the band alignment can be evaluated by studying the behavior of the peak energy shift.

Photoluminescence Experimental Setup

The *PL* experimental setup used in this work is shown in Figure 2.7. A Thor-

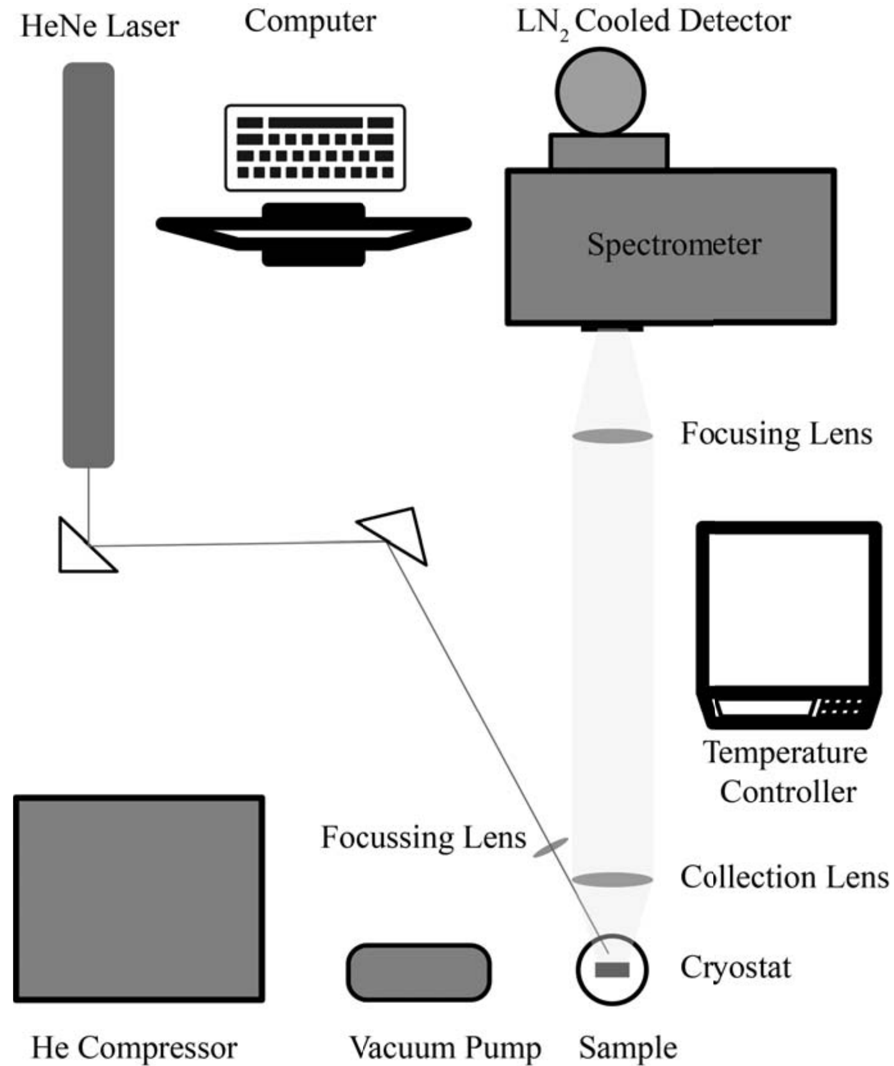

Figure 2.7: *PL* experimental setup.

labs HNL210 10mW HeNe laser (632.8 nm) was used as the excitation source. Borosilicate Crown Newport lenses and Borofloat 33 flat mirrors are used to

focus the laser onto the sample in a He cooled closed-cycle cryostat. The light emitted from the sample is then collected/collimated and focused into a Princeton Instruments Acton SP2500 spectrometer fitted with a Roper Scientific liquid N_2 cooled Princeton Instrument InGaAs linear array photodetector. For PD *PL* measurements, a neutral density filter wheel is used to reduce the laser power incident onto the sample. A heater inside the cryostat is controlled by a Lakeshore 331 temperature controller to vary the temperature of the sample for TD *PL* measurements. Winspec^{TM} data acquisition software is then used to control and record the *PL* measurement data.

After loading the sample into the cryostat, a turbo molecular pump is used to pump down the cryostat to below $\sim 10^{-5}$ torr. A He compressor is then turned on to cool the whole system to 4.2 K, which eventually cryo-pumps the whole system to below 10^{-6} torr. The optical path is aligned to maximize the QD signal ($\sim$ 1060 nm). The exposure time constant is chosen to produce a peak intensity of $\sim$ 60,000 counts (or 30s if the *PL* signal is really low).

For PD *PL*, a combination of neutral density filters are used to achieve a laser power range from 0.05 mW to 10 mW. For TD *PL* measurements, the temperature range is set from 4.2 K to 300 K, with 5 K step size below 100 K and 10 K step above 100 K.

2.2.2 Electroluminescence

Unlike the *PL* probing the radiative recombination of the photo-excited carriers, electroluminescence (*EL*) measures the spontaneous emission of electrically injected

carriers in the semiconductors. In contrast to *PL*, *EL* requires full electrical devices

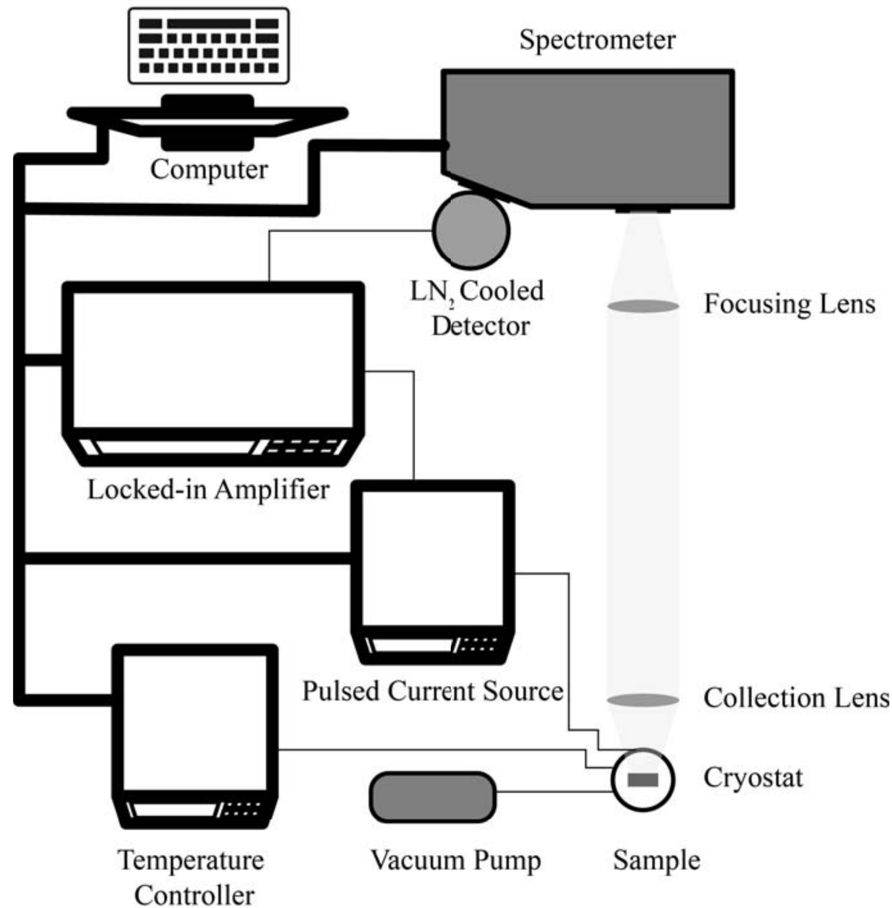

Figure 2.8: *EL* experimental setup.

to inject the carriers into the active region. The direct injection of carriers into the active region in *EL* allows the radiative recombination to be probed directly in the active medium without attenuation of the signal from the emitters (which is common in *PL* measurements). *EL* provides similar information to *PL* such as the bandgap, activation energy, etc. Furthermore (in addition), injection level dependent *EL* measurements allow the determination of the nature of the recombination processes that occur in the system directly.

Electroluminescence Experimental Setup

The *EL* experimental setup is shown in Figure 2.8. A ILX Lightwave LDP 3840B pulsed current source is used to inject the current into the solar cells. The pulse width and duty cycle are set to 100 ms and 10%, respectively. The injection level is varied from 1 mA to 200 mA for injection level dependent *EL* measurements. A set of two Borosilicate Crown Newport lenses is used to collect and focus the *EL* into a SPEX 270M spectrometer fitted with an Edinburgh Instruments liquid N_2 cooled Ge detector. The DC signal from the Ge detector is then sent to an analog lock-in amplifier and recorded by a Keithley 2400 multimeter.

Chapter 3

Optimization of Growth Conditions for InAs/GaAs$_{1-x}$Sb$_x$ Quantum Dots and Devices

The InAs/GaAs quantum dot (QD) system is one of the most well-studied material systems for intermediate band solar cell (IBSC) applications [33–35, 39]. Despite successful demonstration of the fundamental operating procedures of IBSCs, the InAs/GaAs QD system has several drawbacks including having a poor solar spectrum overlap and limited absorption, which inhibit its potential application in PV. The InAs/GaAsSb QD system, however, has been proposed as a promising alternative for QD IBSC applications [42]. This system has several advantages compared with conventional InAs/GaAs QDs such as: (1) a quasi-flat valence band (VB) offset, which facilitates the carrier extraction; (2) a reasonable solar spectrum overlap, which suggests a higher theoretical efficiency [42]; (3) significantly higher QD density, therefore higher absortpion [76].

In this chapter, growth conditions for InAs/GaAs$_{1-x}$Sb$_x$ QDs were optimized in terms of QD density and uniformity. Atomic force microscope (AFM) was used to measure the QD density. Power dependent (at 4.2 K) and temperature dependent *PL* were performed to characterize the optical properties of the QD samples. Then, a set of three InAs/GaAs$_{1-x}$Sb$_x$ QDSCs with the optimal growth conditions for QDs and a control cell were studied using complementary *PL*, *EL*, *J*-*V*, and *EQE* measurements. Those electrical device measurements will be discussed in the next chapter, here only the *PL* measurements will be presented.

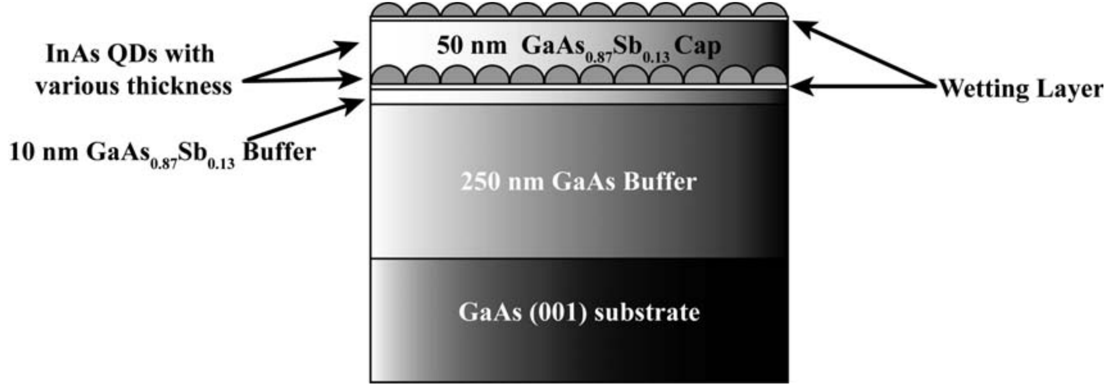

Figure 3.1: Schematic plot of optical InAs/GaAsSb QD sample with various InAs deposition thickness.

All the QD samples described were grown by molecular beam epitaxy (MBE) in the Department of Physics and Astronomy at University of Oklahoma by the Santos-Group. AFM images were captured and analyzed by our collaborators at Amethyst Research Inc. All solar cell structures were processed using standard III-V wet-etch procedures at University College London.

This chapter is partially based on results described in Debnath, Yang et al.'s paper published in the *Journal of Applied Physics* 119.11 (2016): 114301. and Yang et al.'s paper published in *Solar Energy Materials and Solar Cells* 147 (2016): 94-100.

3.1 Growth of InAs/GaAs$_{1-x}$Sb$_x$ Quantum Dots

3.1.1 Experimental Details

All the optical QD samples were grown on semi-insulating GaAs (001) substrates in an Intevac Gen II MBE system. Figure 3.1 is a schematic plot of the optical

sample structure depicting a variable InAs deposition thickness - as there are several different configurations investigated. First, a 250 nm GaAs buffer layer was grown on top of the GaAs substrate at a growth rate of 0.8 monolayer (ML)/s with a substrate temperature (T_{sub}) of 580°C. Then, a 10 nm $GaAs_{1-x}Sb_x$ buffer layer was grown at a rate of 0.39 ML/s with a reduced $T_{sub} = 510 - 520°C$. After that, InAs was deposited at a slower growth rate of 0.1 ML/s under an As_2/In beam equivalent pressure ratio between 25 and 35 with $T_{sub} = 500 - 520°C$. When the deposition thickness of InAs reached the critical thickness $\sim$ 1.65 ML, the Stranski-Krastanov growth mode was triggered and facilitated the direct formation of InAs QDs. The total InAs deposition thickness is varied from 1.75 ML to 4 ML. Then, another 30-50 nm $GaAs_{1-x}Sb_x$ cap layer, which also served as the buffer layer for QD growth, was grown using the same conditions for $GaAs_{1-x}Sb_x$ buffer layer [76]. Finally, another uncapped InAs QDs layer were grown for AFM evaluation of the QD size and density.

Two sets of optical InAs/GaAsSb QD samples were investigated in this chapter. One set was designed to find the optimal InAs deposition thickness (by varying the number of MLs from 1.75 to 4 ML) for the highest QD density and narrowest QD size distribution; the other set was designed to observe the band alignment transition from type-I to type-II by varying the Sb composition in $GaAs_{1-x}Sb_x$ matrix material.

The areal density and QD size for uncapped InAs QDs were analyzed using a Bruker AFM in contact mode [76]. *PL* measurements were performed using the *PL* setup described in Chapter 2.

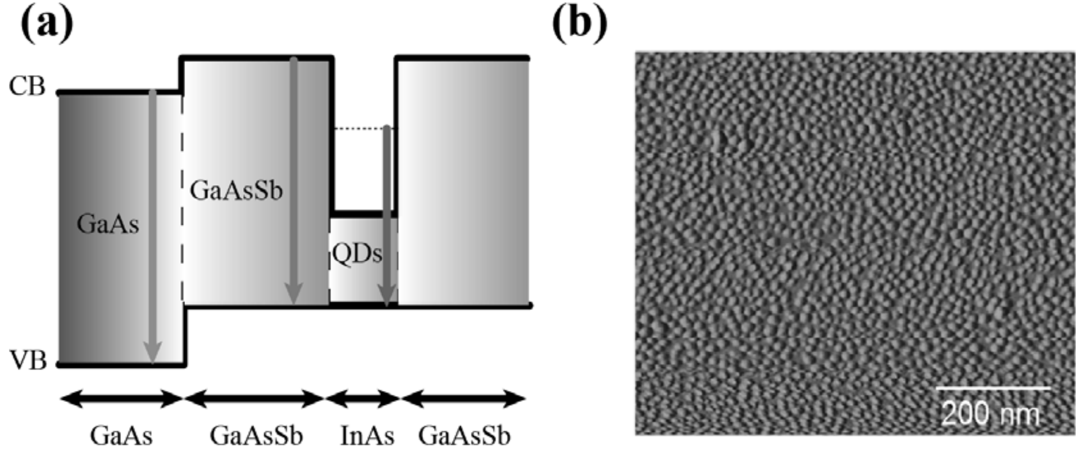

Figure 3.2: (a) Schematic band diagram of InAs QDs in a $GaAs_{0.86}Sb_{0.14}$ matrix; (b) AFM image (1 $\mu m \times 1$ μm) of an uncapped QD layer with 3.0 ML InAs deposition thickness and 13% Sb composition in GaAsSb.

3.1.2 Experimental Results and Discussions

3.1.2.1 Optimization of InAs Deposition Thickness

A schematic band diagram of the optical InAs QD samples is shown in Figure 3.2. At low temperatures, most of the photogenerated carriers are captured and frozen in the QDs due to the large CB offset between the InAs and $GaAs_{1-x}Sb_x$. Since the confinement energy levels in QDs are much lower than the bandgap of GaAs and $GaAs_{1-x}Sb_x$, the QD transition (red arrow) serves as the most efficient pathway for carriers to recombine. Thus, the *PL* signal is dominated by QDs which is consistent with our *PL* measurements.

PL measurements were performed at 4 K on a series of QD samples where the total InAs deposition (ML) has been varied to investigate its effects. A 13%

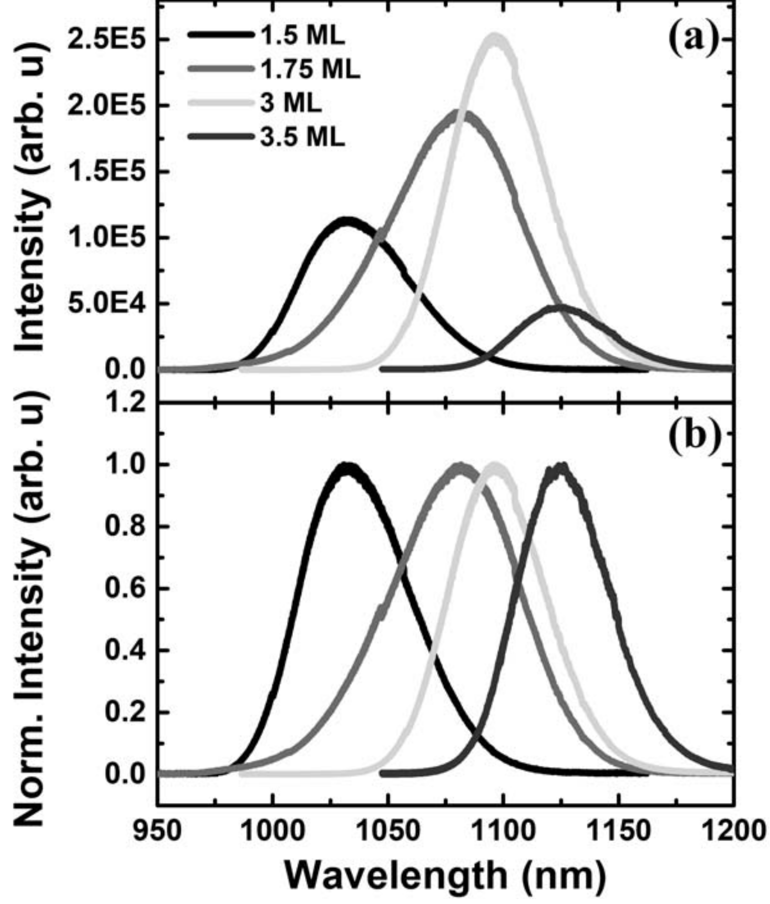

Figure 3.3: 4 K (a) *PL* spectra and (b) normalized *PL* spectra of optical QD samples with 1.5 ML (black), 1.75 ML (red), 3.0 ML (green), and 3.5 ML (blue) InAs deposition thickness.

Sb composition was chosen for the $GaAs_{1-x}Sb_x$ matrix, based on a theoretical prediction of a quasi-flat VB for the InAs/$GaAs_{0.87}Sb_{0.13}$ system [42]. *PL* and normalized *PL* spectra are shown in Figure 3.3. The *PL* intensity increases steadily with increasing deposition thickness from 1.5 ML (black) to 3.0 ML (red) as shown in Figure 3.3 (a), which indicates a higher material quality for 3.0 ML QD sample. The 1.5 ML deposition thickness is close to the critical thickness of the wetting layer to QD formation transition [76]. Apart from the improved *PL* intensity, the

narrowest full width at half maximum (FWHM) of the PL spectra suggests that a more uniform QD size distribution is achieved for the 3.0 ML sample. However, as the InAs thickness is further increased, though the *PL* spectra is still narrow, a dramatic reduction of *PL* intensity is observed for the 3.5 ML layer sample. Such a reduction is most likely attributed to plastic relaxation and defect formation with increasing InAs deposition and the formation of larger QDs as QDs coalesce. We have seen some high quality 3.5 ML QDs but all the 4 ML samples have been poor due to the transition back to 2-D growth.

In Figure 3.3, a red shift of the *PL* peak position is also observed with increasing thickness. The peak position for the 3.5 ML sample shifts by ~100 meV with respect to 1.5 ML sample. Such a change indicates the formation of larger QDs since, the confinement energy is inversely proportional to the size of the QDs; the increasing QD size is as expected - with an increase in InAs ML deposition.

Figure 3.2 (b) shows an example AFM image ($1\ \mu m \times 1\ \mu m$) of an uncapped QD layer after 3.0 ML InAs deposition on a $GaAs_{0.87}Sb_{0.13}$ epilayer. The QD areal density as a function of InAs deposition thickness is summarized in Figure 3.4. Varying the deposition thickness from 1.5 ML to 3.5 ML results in an areal density that increases from $6.5 \times 10^{10}/cm^2$ to $3.5 \times 10^{11}/cm^2$ and then decreases to $2.3 \times 10^{11}/cm^2$; where, the 3.0 ML thickness gives the highest areal density of $3.5 \times 10^{11}/cm^2$, providing an average height and diameter of the InAs QD islands of $\sim$ 2 nm and $\sim$ 15 nm, respectively [76, 77]. This areal density is almost one order magnitude higher than conventional InAs/GaAs QDs [76]. The AFM results, along with the 4 K *PL* measurements suggest that 3.0 ML is the optimal deposition

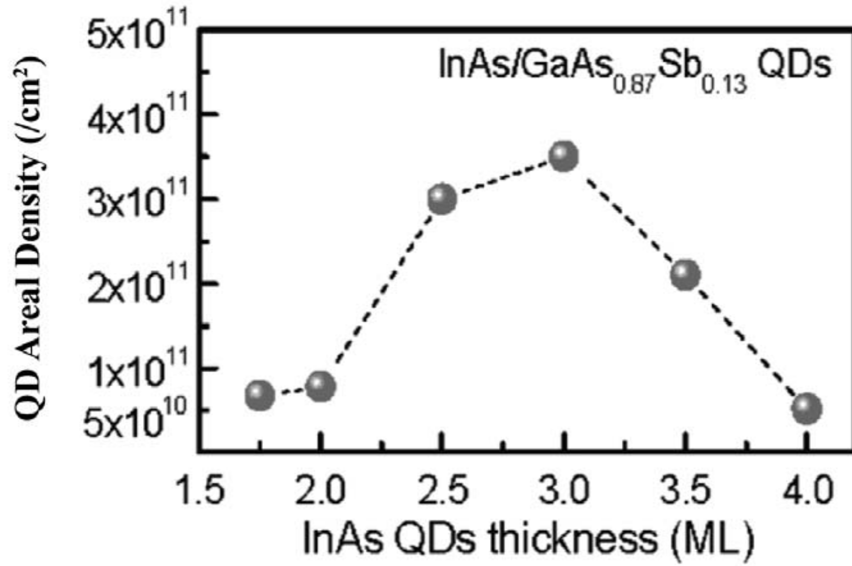

Figure 3.4: The QD areal density as a function of InAs deposition thickness. Reprint from M. C. Debnath, Yang et al. published paper *Journal of Applied Physics* 119.11 (2016): 114301.

thickness for the growth of high quality and dense InAs QDs on $GaAs_{0.87}Sb_{0.13}$.

3.1.2.2 Optimization of Sb Composition in $GaAs_{1-x}Sb_x$ Matrix

Four InAs/$GaAs_{1-x}Sb_x$ QD samples with various Sb composition in $GaAs_{1-x}Sb_x$ matrix were investigated to find a quasi-flat VB alignment which is preferred for IBSC applications. A schematic plot of the sample structure is shown in Figure 3.5 (a). Figure 3.5 (b) illustrates the two different band alignments for InAs/$GaAs_{1-x}Sb_x$ QD heterojunctions. For a type-I band alignment: electrons and holes are both confined in the InAs QDs; in contrast, for a type-II band alignment: electrons are confined in InAs QDs while the holes are excluded into the $GaAs_{1-x}Sb_x$ matrix. Radiative recombination is generally less efficient in

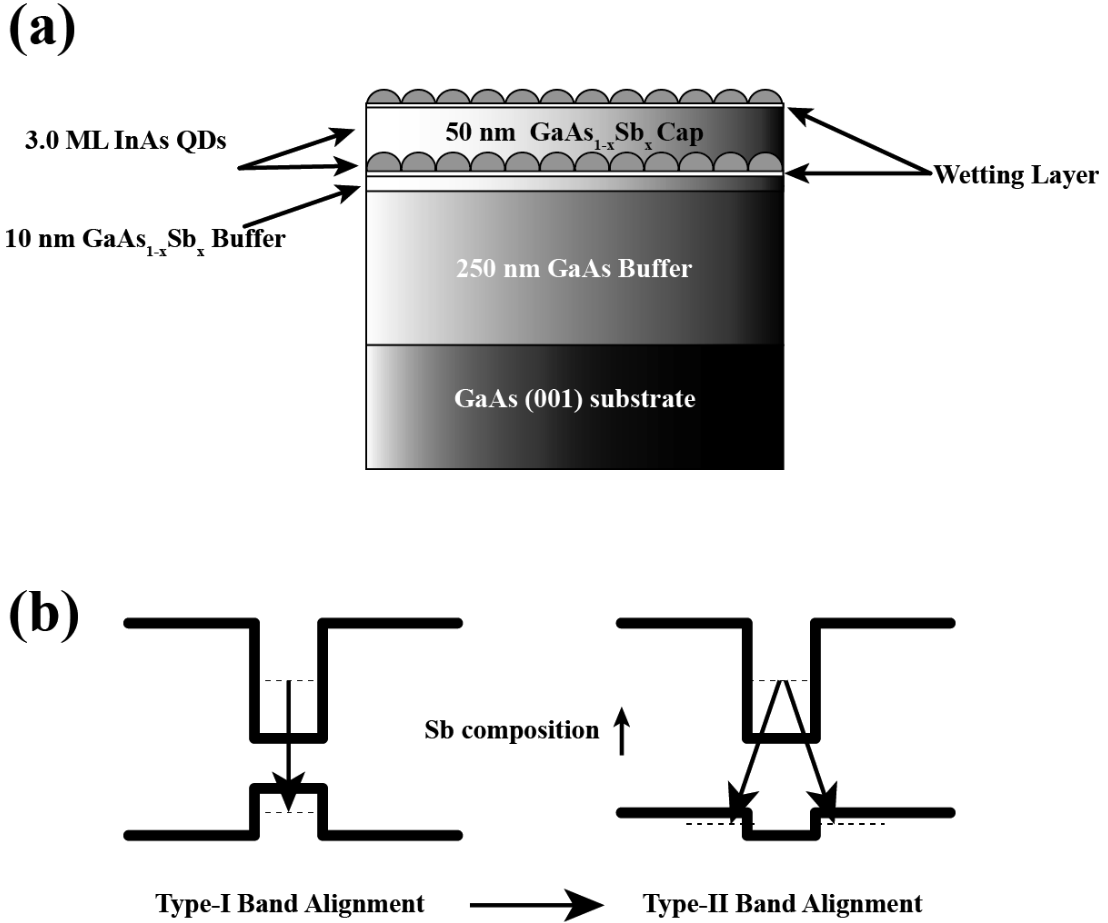

Figure 3.5: (a) Schematic plot of optical InAs/$GaAs_{1-x}Sb_x$ QD sample with various Sb composition in $GaAs_{1-x}Sb_x$ matrix; (b) Type-I and type-II band alignments.

type-II structures than type-I structures, since the electrons and holes are spatially separated in different materials, which reduces the oscillation strength. According to the literature [42, 78–81], the band alignment of InAs/$GaAs_{1-x}Sb_x$ QDs is predicted to change from type-I to type-II as the Sb composition increases above 13-14%.

4 K *PL* and normalized *PL* spectra for various Sb compositions (10%, 12%, 16%, 18%) samples are directly compared in Figure 3.6, with a 50 mulitiplier and

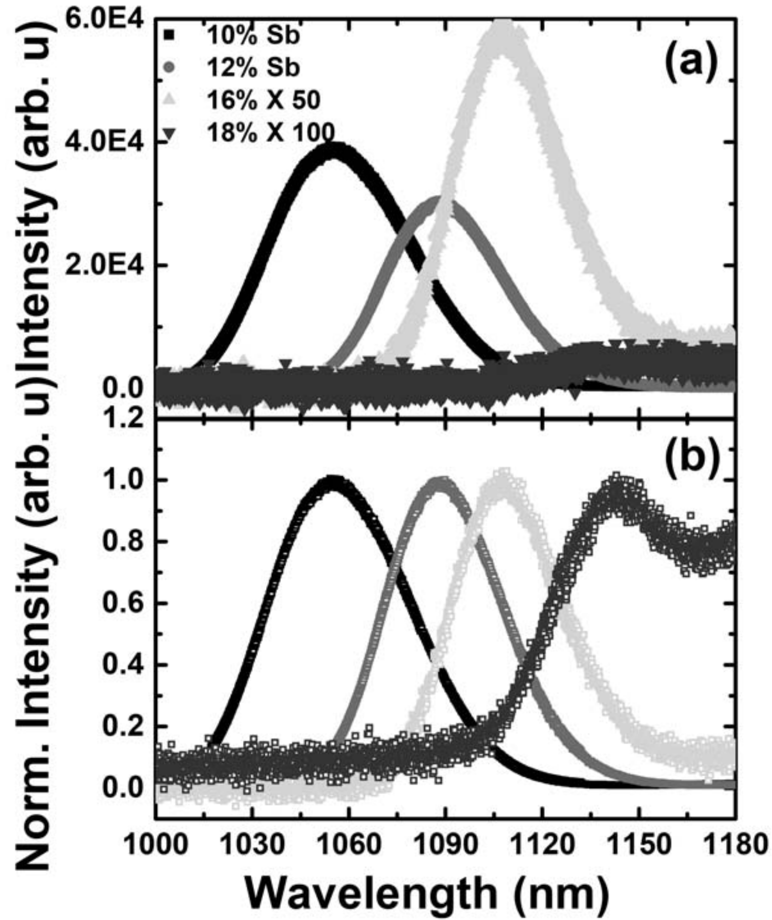

Figure 3.6: (a) PL spectra for QD samples with different Sb compositions in the $GaAs_{1-x}Sb_x$ matrix. A 50 and a 100 multiplier are applied to the 16% and 18% Sb data; (b) Type-I and type-II band alignments. Reprinted from [77].

a 100 multiplier applied to the 16% and 18% Sb data for an intuitive comparison. As shown in Figure 3.6 (a), the *PL* signals from 10% and 12% samples are much brighter than the 16% (two orders of magnitude) and 18% samples (three orders of magnitude). The significant reduction of *PL* intensity when the Sb composition is increased is consistent with the band alignment transition from type-I to type-II, since the spatially separated electrons (in InAs QDs) and holes (in the $GaAs_{1-x}Sb_x$

matrix) in type-II structures will reduce the radiative recombination efficiency dramatically [42, 78–81].

A red shift of the PL peak is also observed in Figure 3.6 with increasing Sb composition in the $GaAs_{1-x}Sb_x$ matrix. This red shift is attributed to the reduction of the effective bandgap, since the increasing Sb composition decreases the barrier heights and therefore reduces the confinement energies. The effective bandgap is given by a combination of bandgap of the materials, confinement energies, and exciton binding energy. Apart from this process, the formation of defects also plays a role in the reduction of the *PL* intensity. Since the lattice mismatch between the matrix and substrate will increase when the Sb composition increases, the density of the defects in the matrix will also increase. This is evidently reflected in the *PL* spectra for the 18% sample, where a strong tail that is even brighter than the QD peak is observed on the low energy side of the *PL* spectra.

TD *PL* spectra of 12% and 16% QD samples are shown in Figure 3.7. Both samples demonstrate a reduction of the *PL* intensity with increasing temperature. However, the 16% sample quenches more rapidly than the 12% sample (see Figure 3.7 (c)), and the *PL* from QDs diminishes when the temperature reaches 95 K. The more rapid quenching of the *PL* intensity can be attributed to the spatial separation of electrons and holes for the type-II band alignment, which results in a smaller overlap between the electron and hole wavefunctions limiting the radiative recombination efficiency. Moreover, signals related to the lower energy defects that are more evident in the 16% sample (see Figure 3.7 (b)) also contribute to

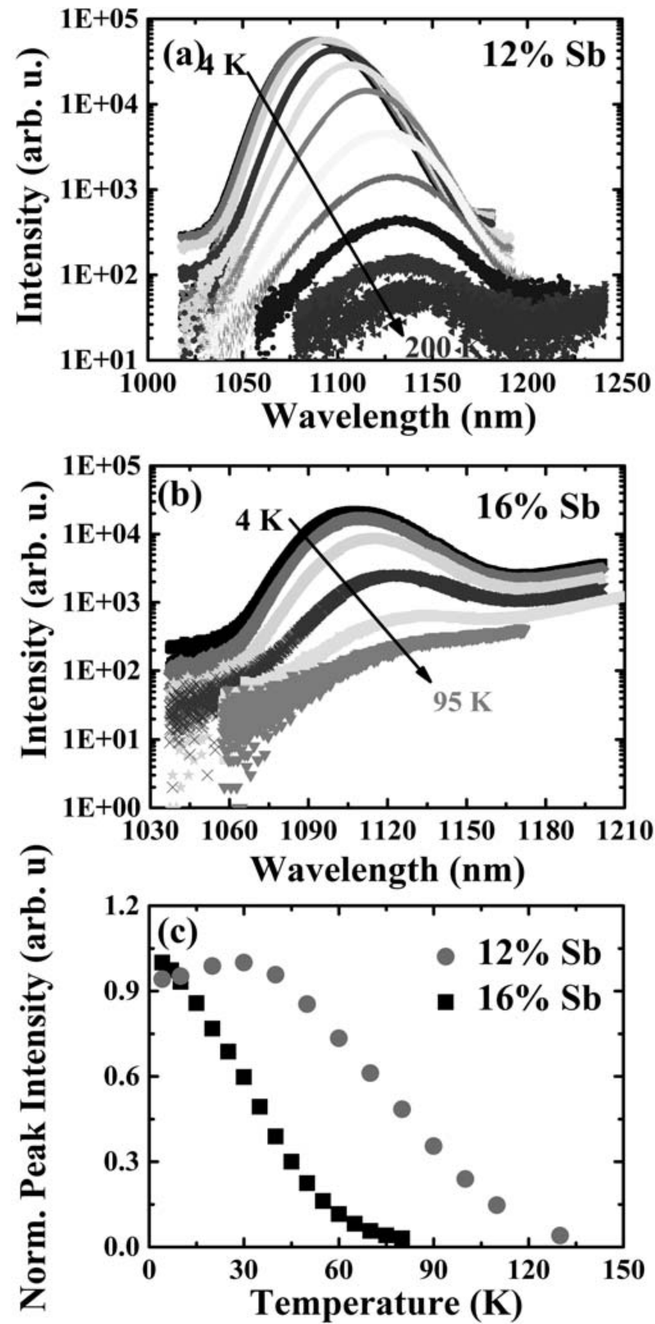

Figure 3.7: Temperature dependent *PL* at 4 K from a 3.0 ML $InAs/GaAs_{1-x}Sb_x$ QD structures with Sb compositions of (a) 12% and (b) 16%. (c) PL peak intensity for the 12% (black symbols) and 16% (red symbols) structures as a function of temperature..

the reduction of the PL; the lower energy peak related to the defects dominates the PL spectra when the temperature increases to 95 K. In contrast, the 12% sample starts to see the defect states above 160 K.

The increased lattice mismatch between the $GaAs_{1-x}Sb_x$ matrix and the GaAs substrate with increasing Sb composition in the matrix may explain the formation of the defects; more Sb in the matrix will reduce the critical thickness and facilitate defect formation. Those defects will capture the thermally activated carriers and reduce the radiative recombination.

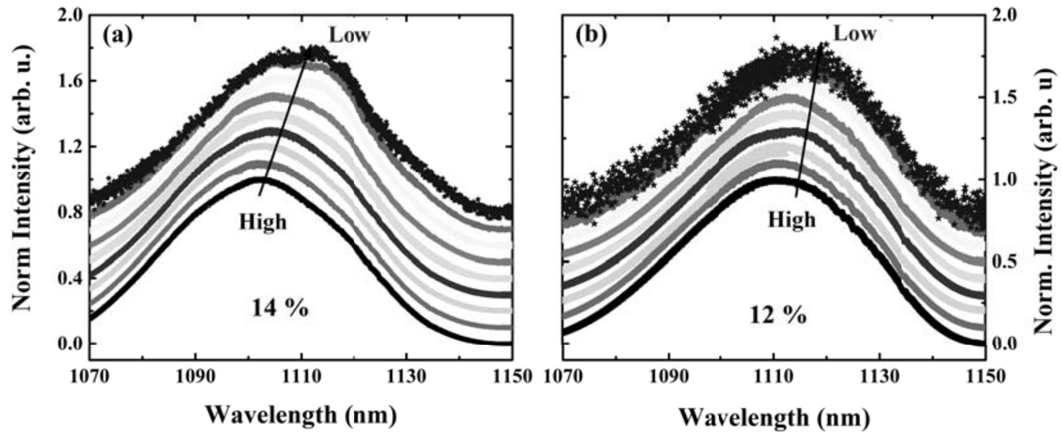

Figure 3.8: Power dependent μPL at 77 K from a 3.0 ML $InAs/GaAs_{1-x}Sb_x$ QD structures with Sb compositions of (a) 10% and (b) 14%.

77 K power dependent micro photoluminescence (μPL) was performed to further investigate the contribution of the band alignment transition (from type-I to type-II) to the intensity reduction. A blue shift is expected for type-II systems with increasing excitation power [79, 81, 82]. In type-II heterojunction structures, the electrons and holes are spatially separated into the two different materials.

With continuous photo-excitation, the accumulated photoexcited carriers electrons and holes at the interface will introduce an electric field that will bend the energy band edge. As the excitation power increases more carriers will accumulate near the interface, where band bending will occur and push the confinement states to higher energy levels. The *PL* peak energy is proportional to the cubic root of the excitation power [79, 81, 82]. In contrast, the photoexcited carriers are confined in the same material for a type-I structure; thus, there will be no such shift in the *PL* measurements with increasing excitation power.

77 K power dependent μPL for 3.0 ML InAs/$GaAs_{0.88}Sb_{0.12}$ and InAs/$GaAs_{0.86}Sb_{0.14}$ QD samples are shown in Figure 3.8. Both samples exhibit a blueshift as the exciation power increases. However, the $\sim$ 3 meV (1.113 - 1.116 eV) blueshift of the peak energy for InAs/$GaAs_{0.88}Sb_{0.12}$ QD sample (which is predicted to have a type-I band alignment) is significantly less than the $\sim$ 10 meV (1.115 - 1.125 eV) shift of the InAs/$GaAs_{0.86}Sb_{0.14}$ QD sample as the excitation power increases from 0.05 to 10 mW.

Figure 3.9 compares the peak energy vs. cubic root of excitation power plots of InAs/$GaAs_{0.88}Sb_{0.12}$ and InAs/$GaAs_{0.86}Sb_{0.14}$ QD samples, where the 14% QD sample exhibits a clearly linear trend indicating a type-II band alignment as predicted [42, 81]. The linear excitation power dependence of the 12% sample may be partially explained by the alloy fluctuations in this material system, where the localized states can trap and spatially separate the photoexcited carriers.

AFM is used to analyze the quality of the uncapped InAs QDs on a $GaAs_{1-x}Sb_x$ surface. The QD areal density as a function of the Sb composition is shown in

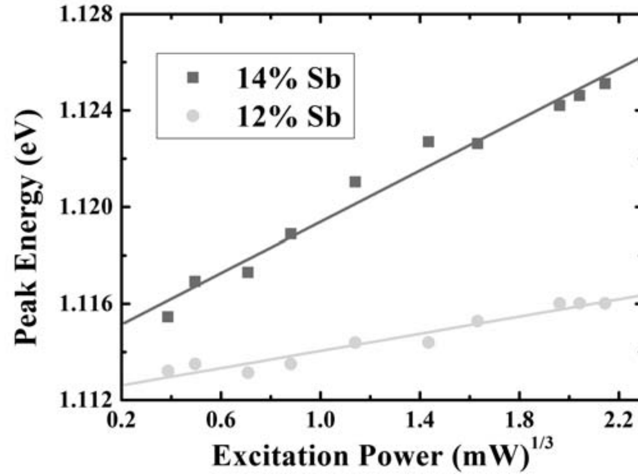

Figure 3.9: PL peak positions are shown for the QD structures with 12% (green symbols) and 14% (red symbols) as a function of the cubic root of the excitation power. Reprint from Yang et.al. *Solar Energy Materials and Solar Cells* 147 (2016): 94-100.

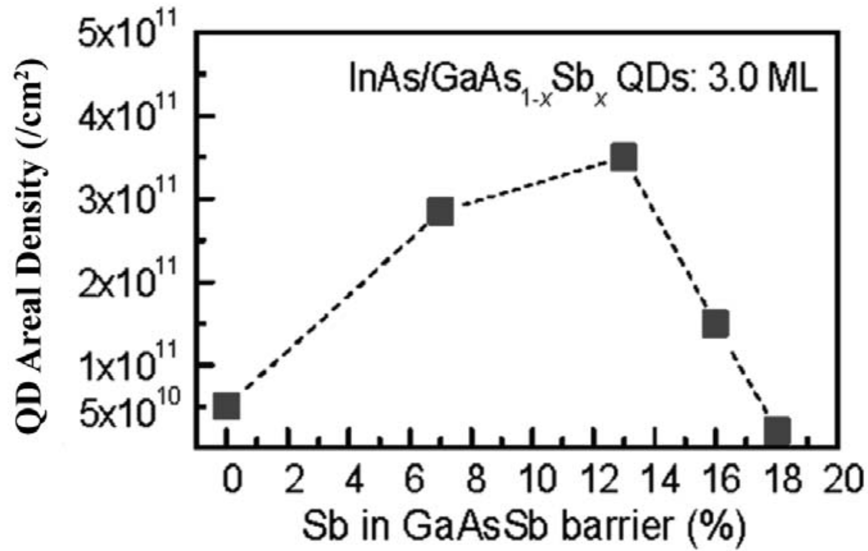

Figure 3.10: The QD areal density as a function of Sb composition in $GaAs_{1-x}Sb_x$ matrix . Reprint from M. C. Debnath, Yang et al. published paper *Journal of Applied Physics* 119.11 (2016): 114301.

Figure 3.10. The areal density reaches its maximum of 3.5 $\times 10^{11}/cm^2$ with 14% Sb in the matrix. The initial increase in areal density can be explained by the suppressed coalescence of some neighboring QDs [76]. By introducing Sb into the matrix, Sb atoms serve as a surfactant and lower the surface energy; therefore, prohibiting the nearby QDs from coalescing together to form larger QDs and decreasing the areal density. As the Sb composition goes above 14%, the smaller critical thickness will trigger dislocation formation in the QDs, resulting in larger relaxed QDs and a reduced areal density.

In summary, the 3.0 ML InAs deposition thickness and 14% Sb composition in the $GaAs_{1-x}Sb_x$ matrix are chosen as the optimal growth conditions for InAs/$GaAs_{1-x}Sb_x$ QD structures. Full solar cell structures with embedded InAs/$GaAs_{1-x}Sb_x$ QDs will be introduced and investigated in the next section.

3.2 Photoluminescence Characterization of Multilayer InAs/$GaAs_{1-x}Sb_x$ Quantum Dot Solar Cells

As shown in the previous section, high QD areal density and good uniformity have been demonstrated for optical InAs/$GaAs_{1-x}Sb_x$ QD reference samples. A 3.0 ML InAs deposition thickness and 14% Sb composition in the $GaAs_{1-x}Sb_x$ matrix are determined as the optimal growth conditions for InAs/$GaAs_{1-x}Sb_x$ QDs based on the AFM and *PL* measurements. However, a full solar cell structure with embedded InAs/$GaAs_{1-x}Sb_x$ QDs was not implemented.

In this section, four p-i-n GaAs solar cells with different intrinsic region

designs grown by MBE are discussed. Power and temperature dependent *PL* measurements are presented as a means to evaluate the material quality of these solar cells.

3.2.1 Experimental Details

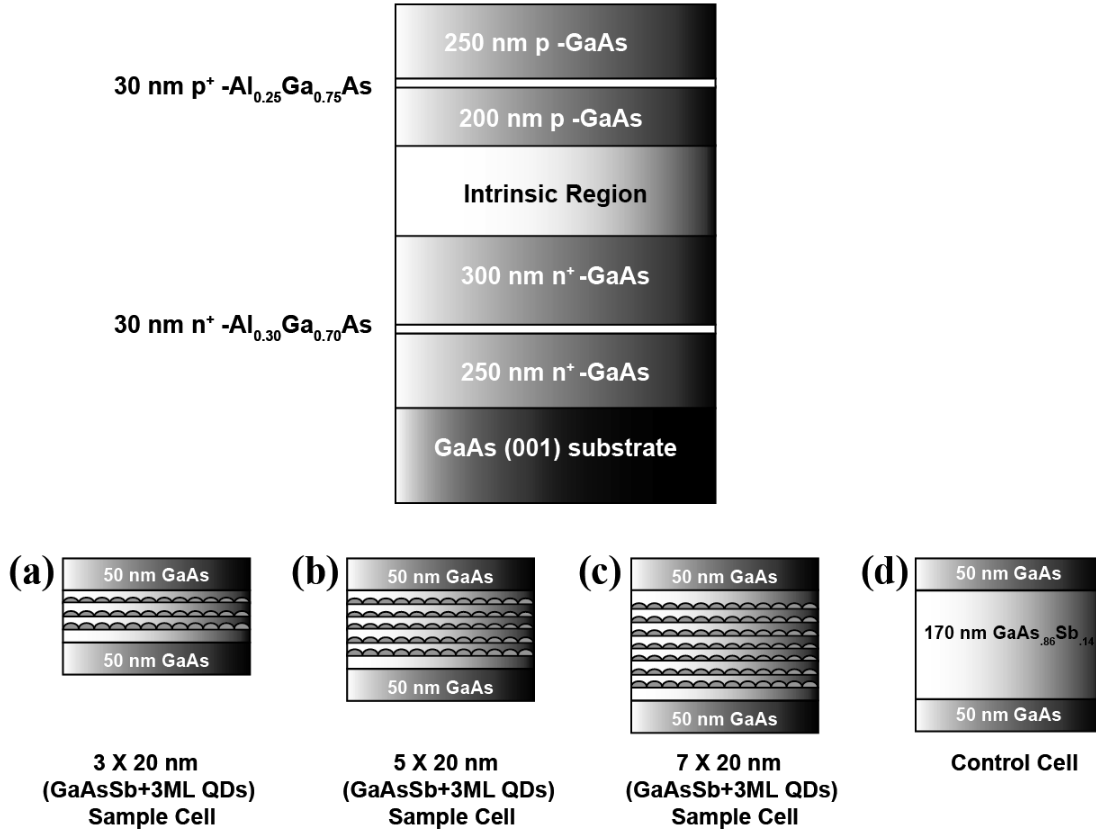

Figure 3.11: Schematic plot of p-i-n GaAs solar cell structures with four different intrinsic region designs: (a) 3 multi-layers, (b) 5 multi-layers, (c) 7 multi-layers of InAs/$GaAs_{0.86}Sb_{0.14}$ QDs, (d) 170 nm $GaAs_{0.86}Sb_{0.14}$.

A schematic plot of four comparative structures investigated in this section is presented in Figure 3.11. Four p-i-n GaAs solar cells with different intrinsic

designs were grown by MBE. The n-type base region of theses solar cells consists of 250 nm of n^+-type GaAs (1×10^{18} cm^{-3}) deposited on top of a n-type GaAs (001) substrate. A 30 nm n-$Al_{0.30}Ga_{0.70}As$ (5×10^{17} cm^{-3}) layer is introduced as a back-surface field layer. This is followed by a 300 nm n-type GaAs (2×10^{17} cm^{-3}) buffer layer, which completes the base region of the solar cell. The p-type emitter on top of the intrinsic region consists of a 200 nm p-GaAs (5×10^{17} cm^{-3}) and a 30 nm p^+-$Al_{0.25}Ga_{0.75}As$ (1×10^{18} cm^{-3}) window layer. The whole structure is then capped with 250 nm of p^{++}-GaAs (1×10^{19} cm^3) for a low resistive p-type contact. For the QD containing structures, the intrinsic region consists of two 50 nm GaAs layers sandwiching 3 (a), 5 (b), and 7 (c) periods of InAs QD layers in a $GaAs_{0.86}Sb_{0.14}$ matrix. Each individual period has a 20 nm $GaAs_{0.86}Sb_{0.14}$ layer upon which 3.0 ML of InAs is deposited to form the QDs. The final period of the QD stack is capped with a 30 nm $GaAs_{0.86}Sb_{0.14}$ layer; the total thickness of the intrinsic region is $\sim$ 230 nm, $\sim$ 250 nm, and $\sim$ 270 nm, respectively. The intrinsic region of the control cell (d) has two 50 nm GaAs layers sandwiching 170 nm of $GaAs_{0.86}Sb_{0.14}$. Temperature dependent and power dependent *PL* were performed using the experimental setup described in Chapter 2.

3.2.2 Experimental Results and Discussions

Normalized 4 K *PL* spectra of all four samples from 750 nm to 1450 nm are shown in Figure 3.12. Multiple transitions are observed in these samples. Peaks related to the GaAs-related transitions (~830 - 870 nm) are more pronounced in the control cell as compared with the QD cells. A broad low energy band is also seen

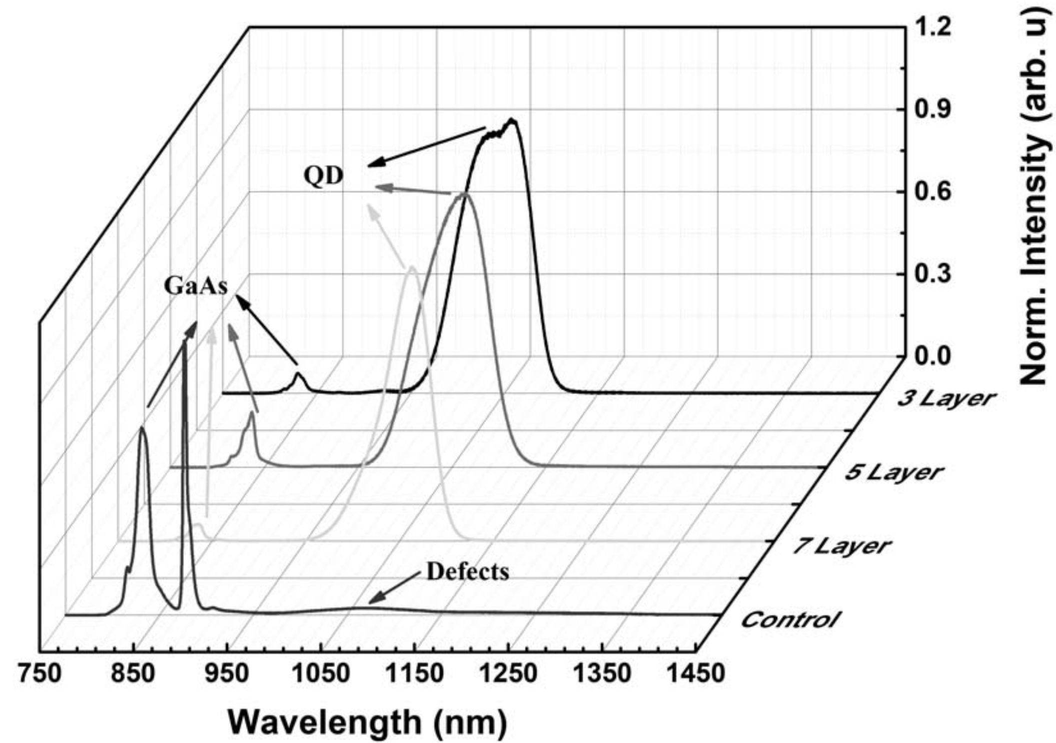

Figure 3.12: 4 K Normalized *PL* spectra of the 3 (black symbols), 5 (red symbols), 7 (green symbols) periods QD samples, and the control sample (blue symbols). Peaks related to QD transition and GaAs are labeled.

in the control cell, which is related to defect formation due to the lattice mismatch between the GaAs and $GaAs_{0.86}Sb_{0.14}$ matrix. The dominant peak (∼1050 - 1060 nm) seen in the three QD samples is related to $InAs/GaAs_{0.86}Sb_{0.14}$ QD transitions (VB to IB). The QD peak shows an asymmetric shape (a high energy shoulder) indicative of a multimodal behavior that is due to inhomogeneities in the QDs.

The multimodal behavior is more pronounced in the 3-layer sample than the other samples. As the number of stacked QD layers becomes larger, the tensile strain between the InAs and $GaAs_{0.86}Sb_{0.14}$ tends to relax [83, 84]; which results

in a formation of larger and more uniform QDs, thus a lower energy *PL*. The $GaAs_{0.86}Sb_{0.14}$ *PL* signals ($\sim$ 910 nm) are limited in the QD samples compared with the control cell, because of the fast relaxation of photoexcited carriers into the QDs which have a lower energy transition than the matrix material.

By comparing all the QD samples, it is clear that the FWHM of the QD peak decreases as the period of QD layer increases. For the 3-layer QD sample, the variation of the QD size is directly reflected in the strongest multimodal behavior, where two *PL* peaks are clearly observed. As more and more QD layers are introduced, the homogeneityof the QDs improves and is better in the 5-layer and 7-layer QD samples relative to the 3-layer sample. The narrowest linewidth is evident for the 7-layer sample, indicating the formation of the most uniform QDs in this sample. However, the number of QD layers cannot be increased infinitely, since the lattice mismatch between the substrate and matrix will introduce defects, which serves as recombination centers and reduce the performance of the solar cell efficiency in terms of increased recombination losses and degradation of the V_{oc}.

4 K PD *PL* measurements were used to probe further the multimodal behavior in the QDSCs. The log intensity as a function of wavelength for all samples is shown in Figure 3.13. The asymmetric shape of the QD samples indicates the existence of more than one *PL* peak (for convenience, labeled as high and low energy peak). Different subsets of QDs with various size, composition, and strain result in this multimodal behavior. As the excitation power increases, the high energy peak of the 3-layer sample is saturated, most likely due to the low QD density and limited distribution of small (high energy peak) QDs compared

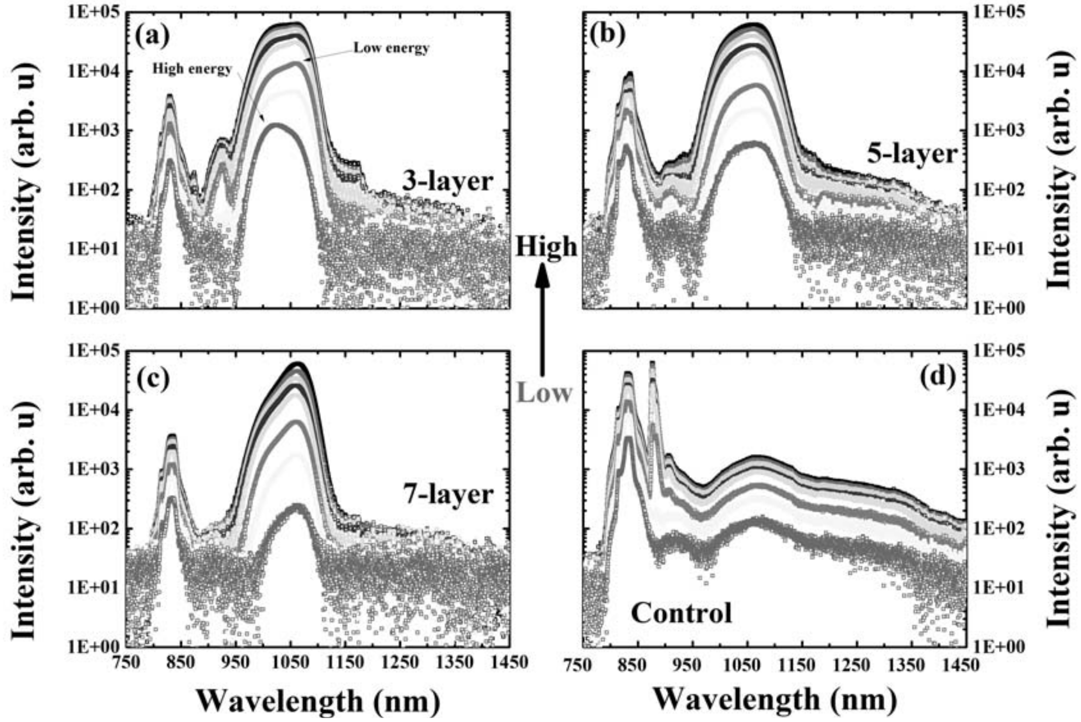

Figure 3.13: Power dependent *PL* measurement results of the (a) 3-layer, (a) 5-layer, (a) 7-layer QD cell, and (d) the control cell.

with the large (low energy peak) ones in the QD ensemble being probed. The high excitation power generates more photoexcited carriers which laterally diffuse into a larger area, therefore sampling a more meaningful statistical ensemble of QDs. With increased period of QD layers, the low energy peak dominates the *PL* spectra; This suggests the formation of more uniform QDs at upper QD layers, which is consistent with narrowest FWHM of 7-layer shown in Figure 3.12.

PL peak energies vs. the cubic root of the excitation power are shown in Figure 3.14 for the 5-layer and 7-layer samples (the 3-layer sample is excluded due to the strong bimodality, which perturbs the extracted peak energy positions). The peak energy increases when the excitation power increases. A linear relationship

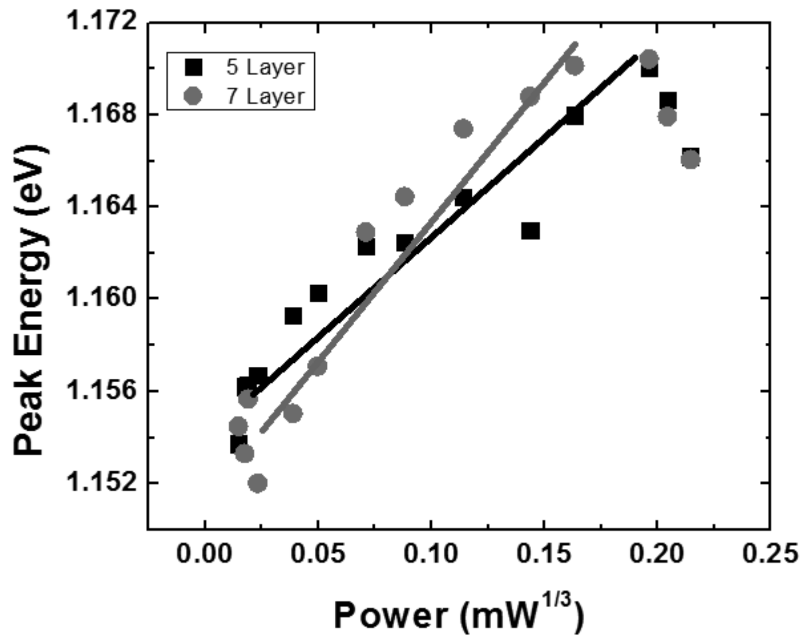

Figure 3.14: *PL* peak energies are shown for 5-layer (blue symbols) and 7-layer (red symbols) QD samples as a function of the cubic root of the excitation power.

between the peak positions and the cube root of the excitation power is observed, which is consistent with a type-II band alignment due to the 14% Sb composition in the matrix, as discussed in Chapter 3. The deviation of the peak energy from the linear trend at low excitation may be the result of the poor signal to noise ratio at such low excitation levels. Another possible reason may be alloy fluctuations, which introduce localized states in the samples that compete with the QD confinement states at low excitation power.

Figure 3.15 shows TD *PL* measurements of all samples from 4 K to 200 K. Peaks related to the GaAs-related transistion(s) seen in all three QD samples and the control sample show a red shift as a function of increasing temperature (830 -

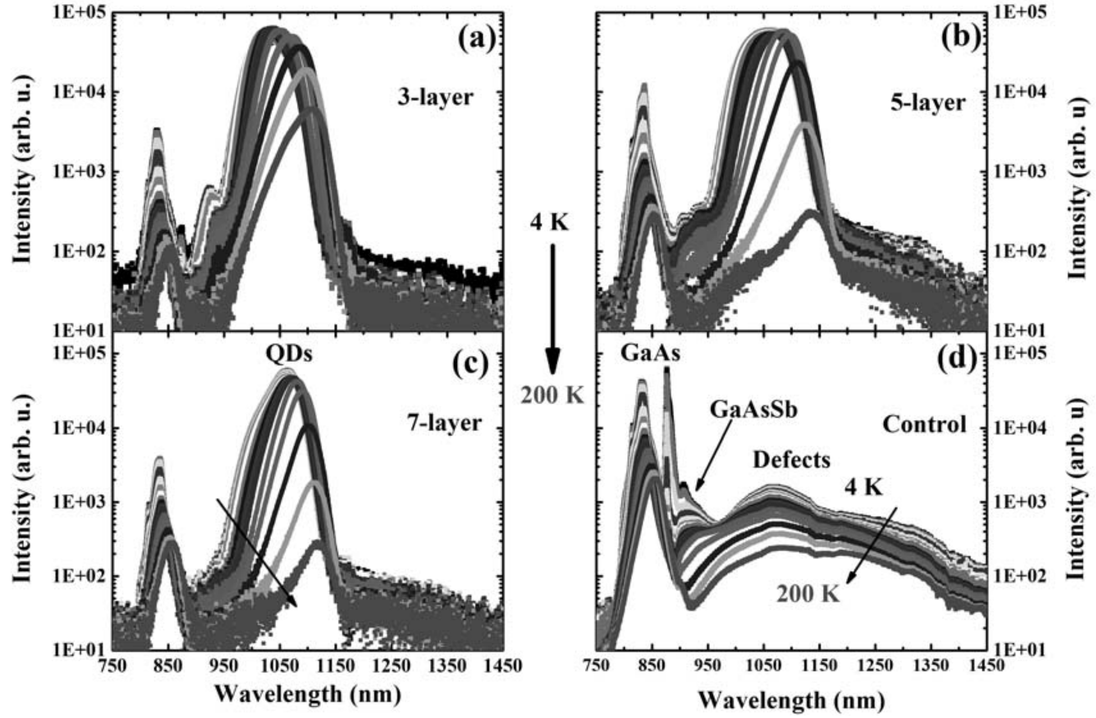

Figure 3.15: Temperature dependent PL measurement results of the (a) 3-layer, (a) 5-layer, (a) 7-layer QD cells, and (d) the control cell from 4 K to 200 K.

850 nm), which follows a standard Varshni shift [85]. The InAs/$GaAs_{0.86}Sb_{0.14}$ QD peak is seen in all three QD samples as expected (Figure 3.15 (a), (b), and (c)) similarly displays a red shift (1080 - 1120 nm) with increasing temperature. The peak intensity of the QD *PL* as a function of temperature is shown in Figure 3.16. The *PL* signal from $GaAs_{0.86}Sb_{0.14}$ is limited (not well-resolved) in the QD structure at low temperatures and becomes nonexistent with increasing temperatures; in comparison, the $GaAs_{0.86}Sb_{0.14}$ signal in the control cell displays a red shift and quenches quickly (Figure 3.15(d) 910 - 975 nm) due to the type-II band alignment. The broad defect-related band (950 - 1500 nm) seen in the 4 K measurement is evident in the control cell across the whole temperature range. In

contrast, the defect peak is relatively weak in the QD samples until 150 K.

The multimodal behavior in the QD samples is more prevalent at low temperature (4 - 120 K). At elevated temperatures (120 - 150 K), the extra thermal energy helps to redistribute the carriers among different subsets of QDs to the lowest energy levels, where the *PL* spectra are then dominated by the lower energy peak from the larger and more uniform QDs, which serve to reduce the FWHM with increasing temperature. As the temperature increases above 150 K, the FWHM broadens due perhaps to thermal broadening. The rapid quenching of the *PL* signal at high temperature is related to enhanced carrier escape processes at elevated temperatures. In addition, a broad peak related to defects becomes more evident for 5-layer and 7-layer samples at elevated temperatures (Figure 3.15 (b) and (c)). This defect band is attributed to dislocations in the $GaAs_{0.86}Sb_{0.14}$ matrix since the thickness of the intrinsic region exceeds that of the critical thickness (~10 nm based on theoretical calculation [86]) for strain relaxation in this system. In comparison, the defect band in the 3-layer sample (Figure 3.15 (a)) is not as pronounced (as in the other two QD samples), presumably due to the thinner intrinsic region, which will therefore contain less defects.

Figure 3.16 summarizes the *PL* peak intensity and peak energy as a function of temperature for all the samples. The 3-layer sample shows a ~30% increase in peak intensity up to 100 K and then the *PL* signal quenches rapidly (Figure 3.16 (a) black symbols). In comparison, the 5-layer and 7-layer samples remain relatively stable in terms of intensity (Figure 3.16 (a) red and green symbols). This difference further supports the suggestion that there is more inhomogeneity in the 3-layer

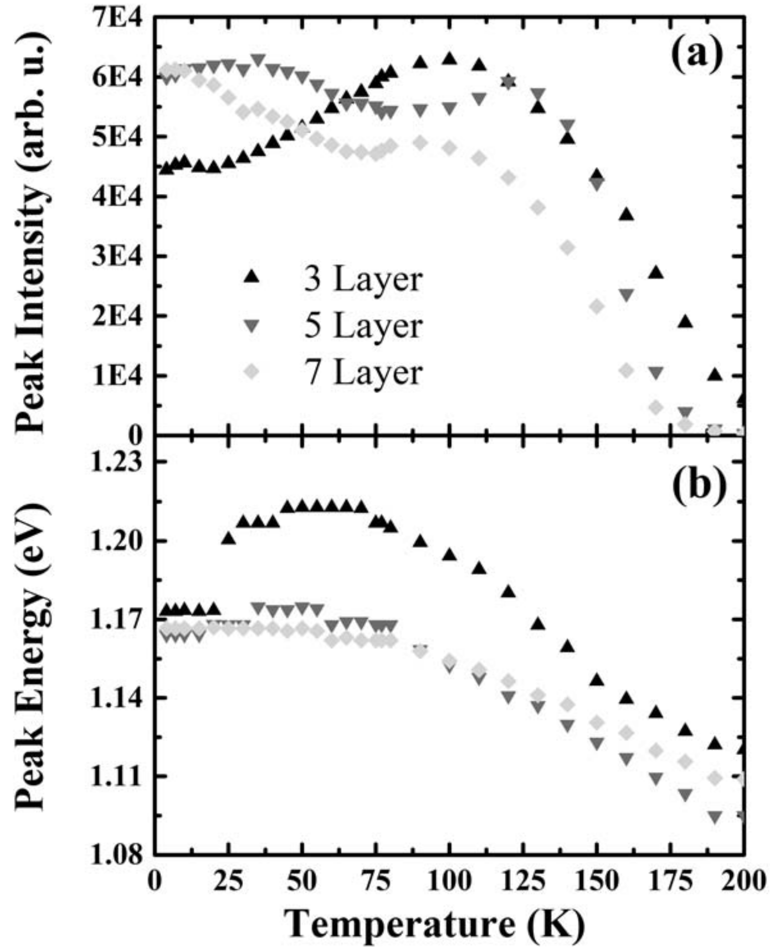

Figure 3.16: (a) Peak intensity and (b) peak energy as a function of temperature for the 3-, 5-, and 7-layer samples from 4 K to 200 K.

sample as compared to the other two QD samples, and is consistent with previous low temperature PD *PL* measurements; where the relative ratio of the high and low energy peak intensity only changes in the 3-layer sample. For the 3-layer sample, below 25 K, the low energy peak has the highest intensity. Afterwards the high energy peak becomes the brightest peak resulting in a jump in peak energy as shown in Figure 3.16 (a). As the temperature increases, the thermal energy enables thermal redistribution of carriers among the QDs to the most populated

QDs (smaller QDs) we are sampling. The deviation of the 3-layer sample from the other two samples suggest the inhomogeneties are clearly greater than for the rest.

This hypothesis is confirmed in the peak energy vs. temperature plot in Figure 3.16 (b). At low temperatures (4 - 25 K), the peak energy for all three samples are close to 1.17 eV. However, the peak energy of the 3-layer sample increases first and then decreases instead of following normal Varshni behavior. This "s-shape" behavior again indicates strong multimodal behavior. The initial increase in the peak energy with increasing temperature suggests enhanced thermal redistribution of carriers from larger QDs to smaller QDs with higher energy; the latter decrease just follows a normal Varshni trend due to the thermal expansion of the lattice. In contrast, the other two samples follow the Varshni trend with a slight "s-shape" evident in the 5-layer sample. This agrees well with the argument that the 7-layer sample has the most uniform QD distribution.

An Arrhenius fit is used to extract the activation energy related to the QD transition in the three QD samples. The fitting equation is given as:

$$I = \frac{I_0}{1 + a * exp(-E_a/k_bT) + b * exp(-E_b/k_bT)}, \tag{3.1}$$

where I_0 represents the integrated PL intensity at 4.2 K; a, b, E_a, and E_b are the coefficients and activation energies associated with various activation processes. k_b and T represent the Boltzmann constant and temperature, respectively.

An example of two activation energy Arrhenius fit is shown in Figure 3.17. The extracted activation energies and standard errors for all samples are summarized

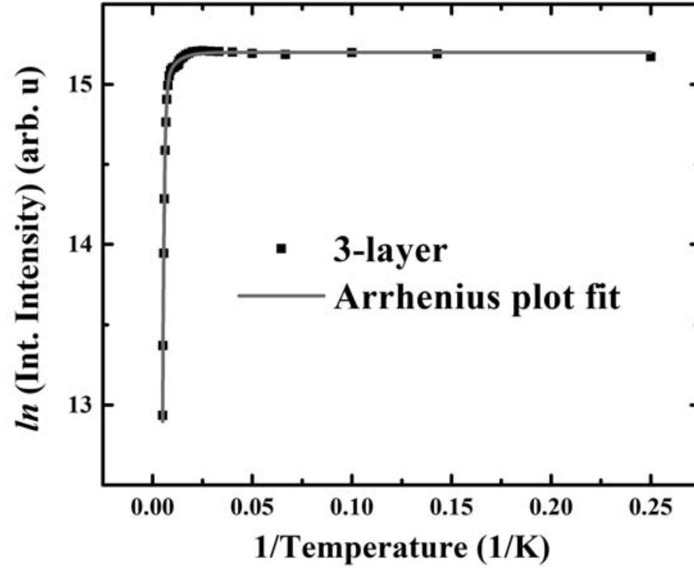

Figure 3.17: Example of two activation Arrhenius fit for 3-layer QD sample.

in Table 3.2.2.

The larger activation energy E_{a1} ($\sim$ 100meV) is very close to the conduction band offset between the QDs (1050 - 1060 nm $\sim$ 1.17 eV) and $GaAs_{0.86}Sb_{0.14}$ matrix (910 - 950 nm $\sim$ 1.30 eV). The slightly smaller E_{a1} for 7-layer sample may be related to the strain relaxation in the sample due to the thicker intrinsic region which results in a smaller energy gap for $GaAs_{0.86}Sb_{0.14}$, or a slight difference in composition as a result of non-uniform growth.

	3-layer		5-layer		7-layer	
Activation Energy	Value (meV)	Standard Error (%)	Value (meV)	Standard Error (%)	Value (meV)	Standard Error (%)
E_{a1}	112.78	0.447	124.85	0.543	95.82	0.297
E_{a2}	15.36	1.657	11.09	0.312	4.68	0.125

Table 3.1: Activation energies extracted from two activation energy Arrhenius plot fitting of three QD samples.

The origin of the activation energy E_{a2} is not well understood but may be associated with the energy barrier for photoexcited carriers that escape through defect-mediated mechanisms or may be due to the localization of photogenerated holes in alloy fluctuations. The reduction of E_{a2} indicates the difficulty for carriers to escape is as follows: 3-layer $>$ 5-layer $>$ 7-layer sample. This is consistent with the much faster quenching of the PL spectra for the 7-layer sample than the other two samples. As the thermally assisted escaped carriers see the defect-related recombination centers in the $GaAs_{0.86}Sb_{0.14}$ matrix, the defect band emerges and the radiative recombination from the QDs decreases as the non-radiative losses dominate. However, the QD transition in the 3-layer sample remains relatively bright even at 200 K; the larger E_{a2} prohibits the carriers from communicating with the defects in the matrix until a higher temperature is reached. This also suggests that more defects form in the matrix with increased period of the QD layer, since the intrinsic region exceeding the critical thickness results in the strain relaxation and the formation of dislocations in the $GaAs_{0.86}Sb_{0.14}$ matrix.

3.3 Conclusion

Two sets of optical $InAs/GaAs_{1-x}Sb_x$ QD samples were grown by MBE. Complementary AFM and PL measurements were used to characterize the quality of the QDs and to track a band alignment transition from type-I to type-II. By increasing the InAs deposition thickness, a maximum areal density of $\sim 3.5 \times 10^{11}/cm^2$ is achieved for the 3.0 ML $InAs/GaAs_{0.86}Sb_{0.14}$ QD sample, along with good

uniformity in both size (~ 2 nm) and shape (~ 15 nm). 4 K *PL* measurements show that the 3.0 ML sample also has the brightest *PL* and the narrowest FWHM, which are consistent with our AFM results that the 3.0 ML deposition is optimized in terms of material quality.

With a fixed 3.0 ML InAs deposition thickness, the Sb composition in the $GaAs_{1-x}Sb_x$ matrix was varied to probe the band alignment transition from type-I to type-II. A red shift of the *PL* peak is observed when increasing the Sb composition from 10% to 18%. Temperature dependent *PL* measurements of 12% and 16% samples show a much faster quenching of the *PL* for 16% sample, which suggests a transition to a type-II band alignment for the 16% sample. Moreover, a broad and dominant defect peak is seen at high temperatures. The formation of defect states at a higher Sb composition also results in a quenching of the PL signal.

To reduce the influence of defect states, the 12% and 14% Sb samples were studied using power dependent *PL* measurements. In type-II structures, the *PL* peak energy is proportional to the cube root of the excitation power as a result of escalation of band bending with accumulation of carriers near the interface. A blue shift is recognized in both 12% and 14% samples when the excitation power increases. However, the the blue shift for the 12% sample is three times smaller than for the 14% sample; this small blue shift is related to alloy fluctuations and inhomogeneities in the 12% sample. These results strongly indicate a band alignment transition from type-I to type-II around 14% Sb composition in the matrix. AFM results also indicate that the 14% sample has the highest areal

density and best uniformity.

Four p-i-n GaAs solar cells with different intrinsic region designs were grown by MBE. The material quality of these four solar cells were investigated using *PL* measurements. Inhomogeneities induced multimodality was found to account for the observed "s-shape" of the QD peak energies as a function of temperature. Faster quenching of *PL* spectra for devices with a thicker intrinsic region samples indicates the formation of more defects in these structures. These behaviors qualitatively suggest the defect states associated with the lattice mismatch between $GaAs_{0.86}Sb_{0.14}$ and GaAs account for the degradation of the quality of the materials.

Chapter 4

Electrical Characterization of InAs/$GaAs_{1-x}Sb_x$ Quantum Dots Solar Cells

In Chapter 3, we presented InAs/$GaAs_{1-x}Sb_x$ quantum dot optical samples with high QD areal density and reasonable uniformity. A 3.0 ML InAs deposition thickness and a 14% Sb composition in $GaAs_{1-x}Sb_x$ matrix are determined as the optimal growth conditions for a reference InAs/$GaAs_{1-x}Sb_x$ QD sample. Here, four GaAs p-i-n solar cells with different intrinsic region designs grown by MBE are presented. Power and temperature dependent *PL* measurements are used to evaluate the material quality and performance of these devices.

Defect states associated with the lattice mismatch between the $GaAs_{0.86}Sb_{0.14}$ layers and the GaAs substrate strongly affect material quality. In this chapter, we use a suite of experimental techniques including current-voltage (J-V), external quantum efficiency (*EQE*), and electroluminescence (*EL*) to investigate the influence of these defect states on the performance of the solar cell. Using a simple analysis, injection level dependent *EL* is used to probe the recombination losses in such a system with respect (and in parallel) to conventional PV characterization.

This chapter is partially based on Yang et al.'s paper published in *Solar Energy Materials and Solar Cells* 147 (2016): 94-100. and Yang et al.'s manuscript under review in *IEEE Journal of Photovoltaics*.

4.1 Experimental Details

Detailed structures of the investigated samples were illustrated in Chapter 3 (see Figure 3.11). All solar cell structures were processed following standard III-V wet-etch procedures at University College London. The processed solar cells were then mounted on top of a copper plate using silver epoxy. Finally, indium was used to bond Au wires onto the p-contacts. Temperature dependent *J-V*, *EQE*, and *EL* were performed using the experimental setups described in Chapter 2.

4.2 Experimental Results and Discussions

4.2.1 Current-Voltage Measurements

To better understand the quality of the devices with respect to the photovoltaic behavior, *J-V* measurements were performed. 77 K and room temperature *J-V* measurements for all four devices are presented in Figure 4.1. At 77 K, the control cell has a V_{oc} of $\sim$ 1.2 V under 1-sun illumination. In comparison, all of the QD samples have smaller V_{oc} with $\sim$ 1.14 V,$\sim$ 1.14 V, and $\sim$ 1.10 V for the 3-layer, 5-layer, and 7-layer devices under 1-sun illumination, respectively. The reduction of the V_{oc} is related to a combination of the fundamental nature of the additional recombination path introduced by the QDs in the active region [31] and a reduction of the bandgap. Also, all three QD samples show strong inhomogeneity, where multiple slopes around the inflection point are observed; however, this is not observed in the control cell due to the absence of the QD layers. At 77 K, the 7-layer QD sample has a fairly large series resistance (Figure 4.1 (a) black arrow),

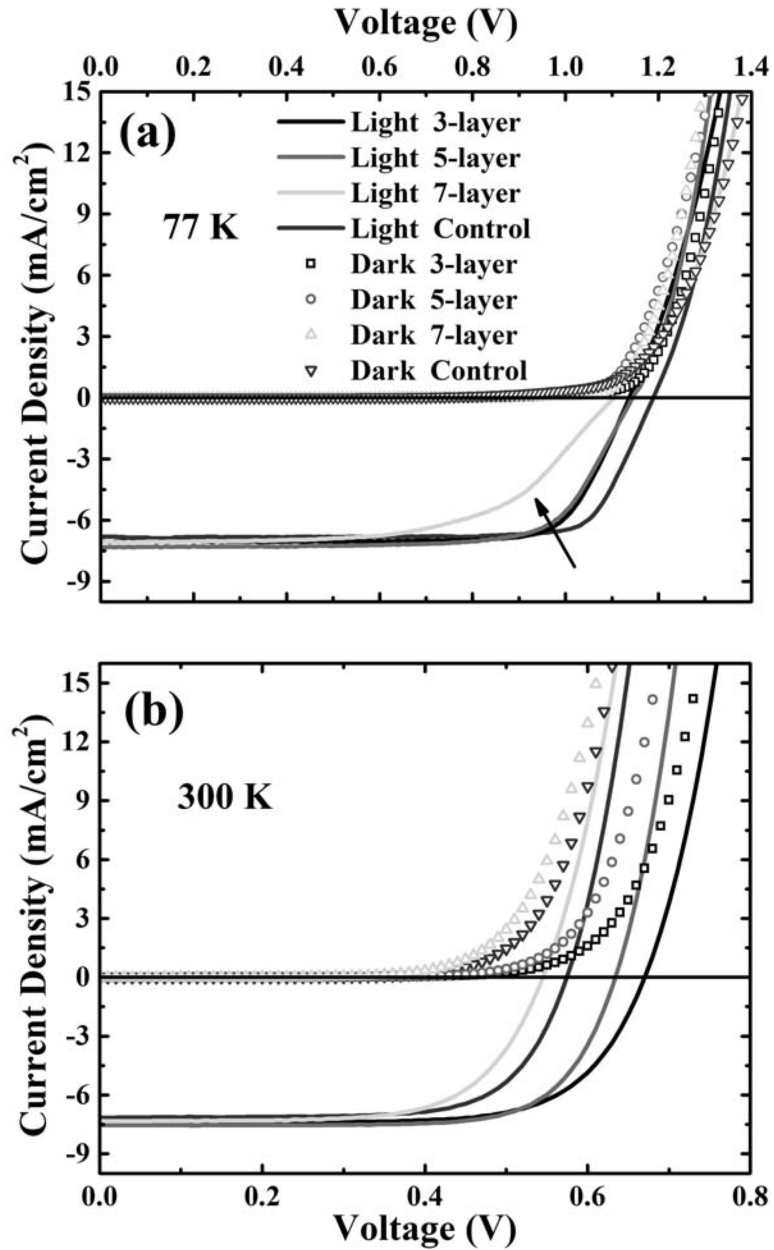

Figure 4.1: (a) 77 K and (b) room temperature J-V measurements; solid lines and open symbols represent the light and dark measurements respectively.

which significantly affects the overall fill factor and efficiency. Such a large series resistance is due to the inhibited carrier transfer at low temperature, whereby

photogenerated carriers are strongly localized in the QDs.

At 300 K, a dramatic reduction of V_{oc} is seen across all four devices with a larger reduction for samples with thicker intrinsic regions (5- and 7-layer samples). The thinnest QD sample (3-layer) has the largest V_{oc} - ~0.67 V. In contrast, both the control and 7-layer QD cells display the smallest V_{oc}s of $\sim$ 0.55 V and $\sim$ 0.57 V, respectively. This is consistent with the trend of the activation energy E_{a2} extracted from table 3.2.2, where the greater number of the stacked QD layers corresponds to a smaller the activation energy. A smaller activation energy allows for easier escape of carriers from the QDs, which can be subsequently captured by defects in the matrix material. This results in an increase of the recombination current and a decrease of the V_{oc}. The effects of the non-ideality or parasitic resistance also disappear at 300 K (Figure 4.1 (b)), which is attributed to the thermally enhanced carrier escape process from the QDs at higher temperatures.

Figure 4.2 (a), (b), (c), and (d) compare the *J*-*V* measurements for the three QD and control cells under illumination as a function of temperature. As seen in the 77 K and 300 K measurements, there are two main features evident in these data as the temperature increases: (1) a large reduction of V_{oc}; (2) the vanishing of series resistance and multimodality in the QD cells (Figure 4.2(a), (b), (c)).

At low temperatures (77 - 150 K), the effect of series resistance and the multimodal behavior is more pronounced in the QD cells, which reflects the increased carrier localization in the QD samples. This is consistent with TD *PL* measurements (see Figure 3.15 and 3.16 (a)) where the *PL* peak intensity remains relatively stable due to the isolation of photogenerated carriers in QDs

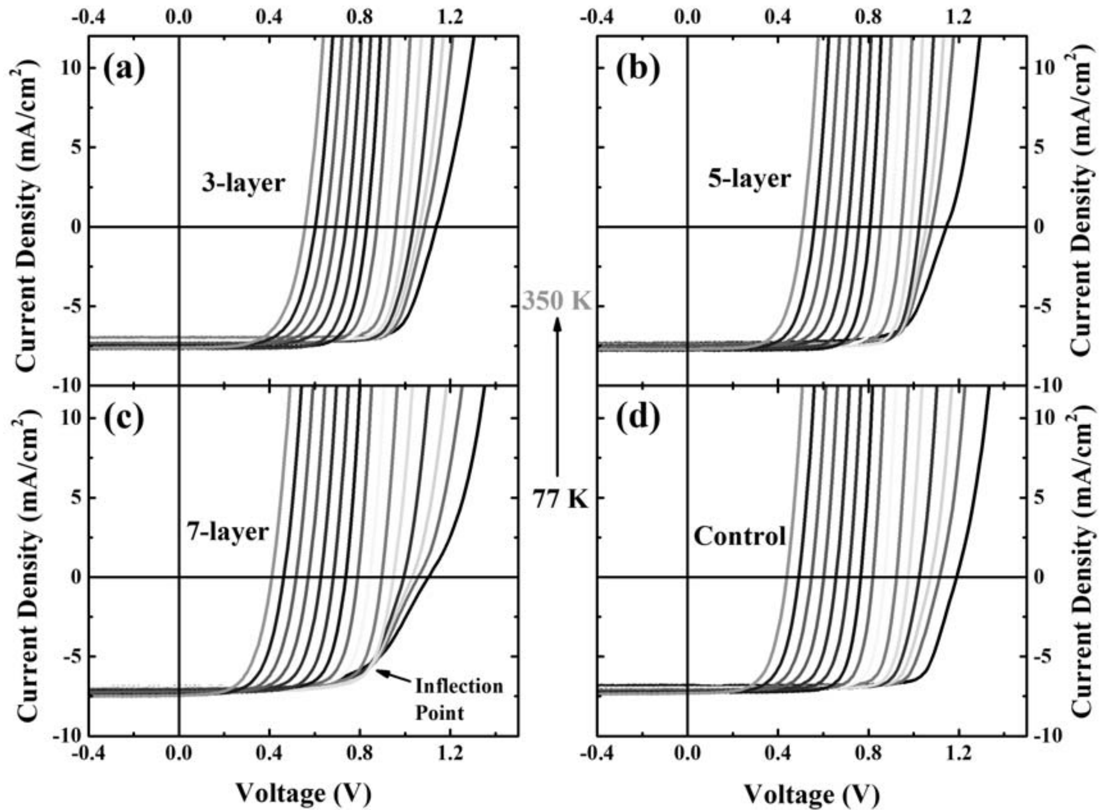

Figure 4.2: Temperature dependent J-V measurements for (a) 3-layer, (b) 5-layer, (c) 7-layer, and (d) control cell from 77 K to 350 K.

at lower temperatures. As the number of QD layers increases, the inflection point attributed to the higher series resistance induced by carrier localizations becomes more apparent. This is attributed to enhanced photon absorption in the sample with more QDs resulting in a larger portion of frozen photogenerated carriers. Although not dominant, localization in defects at lower temperatures also contributes to the resistance, which can be seen at low temperatures for the control structure in Figure 4.2 (d). As the temperature continues to increase, a dramatic reduction of V_{oc} is observed for all cells, which is much larger than the expected temperature dependent Varshni trend. A dVoc/dT plot is a commonly used metric

to compare the V_{oc} reduction as a function of temperature. In comparison with other types of solar cells including Si, GaAs, CdTe, etc. [87], the slope extracted for all four devices has a gradient above 250 K close to 2.7 mV/K, which is significantly larger than typical values of 1.6 - 2.3 mV/K seen in other cells [87]. Such a massive reduction of V_{oc} is directly related to a significant increase in the dark current and a reduction in the quality of the diode. This rising dark saturation current is attributed to increasing non-radiative recombination currents and results in the significant decrease in V_{oc}. The origin of the dark current losses is related to the defect and dislocation formation due to the lattice mismatch between GaAs and $GaAs_{0.86}Sb_{0.14}$.

The TD J-V measurements are summarized in Figure 4.3. Figure 4.3(a) compares the V_{oc} of the three QD (black squares, red circles, and green triangles) and control (blue triangles) cells. At low temperatures, the V_{oc} recorded for QD cells is smaller than the control cell under 1-sun illumination, which is expected due to a combination of the fundamental nature of the additional recombination path provided by the QDs in the active region [31] and a reduced bandgap as mentioned previously. However, the V_{oc}s for the control and 7-layer cells quench more rapidly than the 3-layer and 5-layer QD cells with increasing temperature. The V_{oc} reduction is proportional to the thickness of the intrinsic region, which reflects the increased dark current loss with thicker intrinsic region. This is consistent with the longer minority carrier transport required and the idea that the strain relaxation and dislocation density of the $GaAs_{0.86}Sb_{0.14}$ matrix and p-GaAs emitter increase due to the intrinsic region exceeding the critical thickness

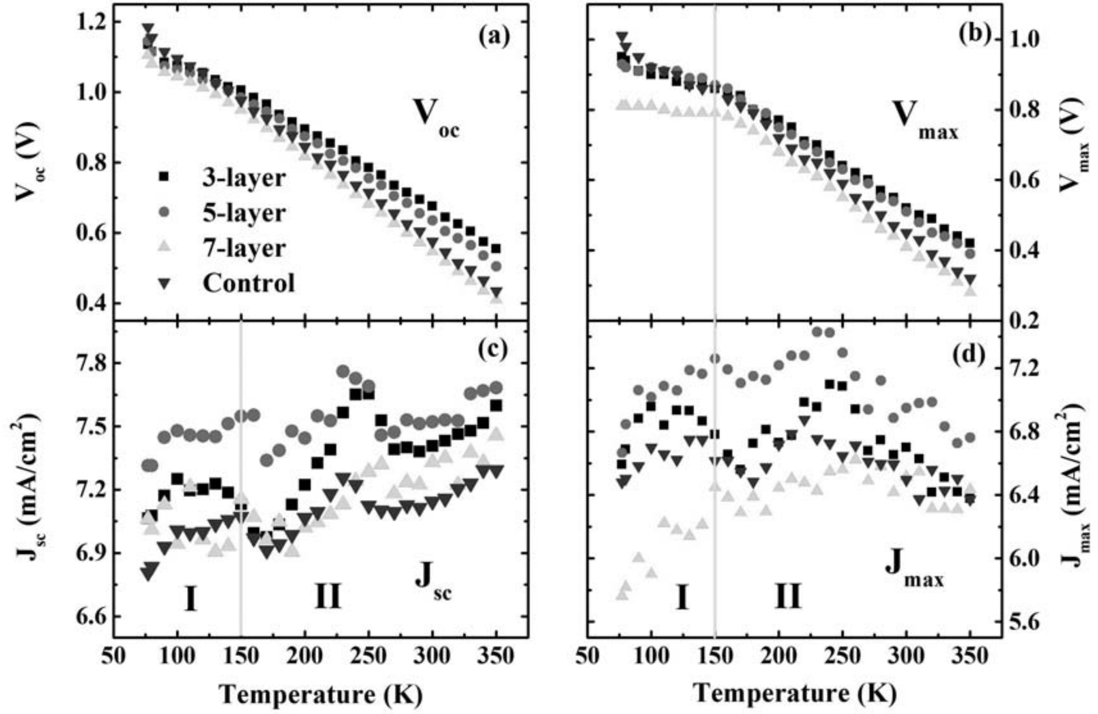

Figure 4.3: Extracted J-V parameters (a) V_{oc}, (b) V_{max}, (c) J_{sc}, (d) J_{max} as a function of temperature; black, red, green, and blue symbols represent the 3-layer, 5-layer, 7-layer and control cells respectively.

(estimated to be 10 nm based on a theoretical calculation for a 1.11% lattice mismatch between the GaAs and $GaAs_{0.86}Sb_{0.14}$ [86]) of the system.

Figure 4.3 (b) and (d) compare the V_{max} and J_{max} for the control and QD cells as a function of temperature, respectively. The V_{max} and J_{max} corresponds to the coordinates of the maximum power point of the illuminated J-V. For the QD cells, as the temperature increases from 77 K to 150 K (region **I**), a smaller reduction of V_{max} ($\sim$0.02 - $\sim$0.09 V) is observed compared with the control cell ($\sim$ 0.16 V). This difference in the behavior of the V_{max} and V_{oc} (77 - 150 K region **I**) with increasing temperature reflects the improvement in FF (see Figure 4.2),

since the introduced thermal energy at elevated temperatures enables thermal redistribution of carriers among the QDs and decreases the series resistance as observed at T < 150 K (Figure 4.3 (b) and (c)).

As the temperature keeps increasing above 150 K (region **II**), the thermally activated carriers are captured by the defect states in the $GaAs_{0.86}Sb_{0.14}$ matrix that are activated by the ionization of impurities at elevated temperature, and result in the recombination current loss. Now, the V_{max} for QD samples is similar to that of the control cell and all follow the steady decreasing trend of the V_{oc}.

These data indicate that at T < 150 K, where photogenerated carriers are localized in the QDs, the properties of the QD samples are mainly determined by carrier transport within the QDs. Above 150 K as carriers redistribute and escape the dots, the J-V characteristics are determined by the quality of the matrix, base, and emitter materials. This is consistent with the J_{sc}, J_{max}, V_{oc}, and V_{max} data from the QD samples in Figure 4.3 above 150 K. This also strongly correlates to the rapid quenching of the PL at T > 150 K (see Figure 3.16) due to the increased thermal activation of carriers from the QDs and a subsequent increase in the strength of Shockley-Read-Hall (SRH) recombination (as seen in the *EL* section).

In contrast, the V_{max} for the control cell follows the same trend of the V_{oc} at low temperatures, which suggests the absence of a strong localization of carriers; Thus, carriers in the control cell interact with non-radiative centers (defect states) more readily and the maximum power point decreases monotonically (reduction of the V_{max}) as more defect states become activated with increasing temperature.

Typically, a small increase in J_{sc} and J_{max} is expected due to the reduction of the effective bandgap of the solar cell structure. However, we've observed a complex behavior for J_{sc} and J_{max} (Figure 4.3 (b) and (c)), where J_{sc}/J_{max} has a local minimum around $\sim$ 170 K and then fluctuates with an increasing trend. This is a result of the competing process between the increased non-radiative recombination loss at higher temperatures (due to the deleterious defect states in the $GaAs_{0.86}Sb_{0.14}$ matrix [88]) and thermally escaped carriers from the QDs. Above 240 K, where the thermal escape takes the lead over the the non-radiative recombination, the J_{sc}/J_{max} keeps increasing.

The unconventional TD J-V measurement - where the V_{oc} decreases significantly without a noticeable enhancement of the J_{sc} - is consistent with the hypothesis that there is a thermally mediated transition from radiative to non-radiative processes in PL measurements above $\sim$ 120 K; at T $>$ 150 K, SRH processes completely dominate the recombination processes.

4.2.2 External Quantum Efficiency Measurements

Unlike the PL measurements that probes the radiative recombination of photogenerated carriers, EQE measurements reflect the absorption of photons and extraction of photogenerated carriers. Figure 4.4 shows the EQE results for the 3-layer (black line), 5-layer (red line), 7-layer (green line), and control (blue line) samples at 77 K, respectively. Carrier extraction from the GaAs (400 - 830 nm) layer and the $GaAs_{0.86}Sb_{0.14}$ matrix (830 - 930 nm) is present in all samples. The absorption edges (Figure 4.4) for these transitions are in good agreement with

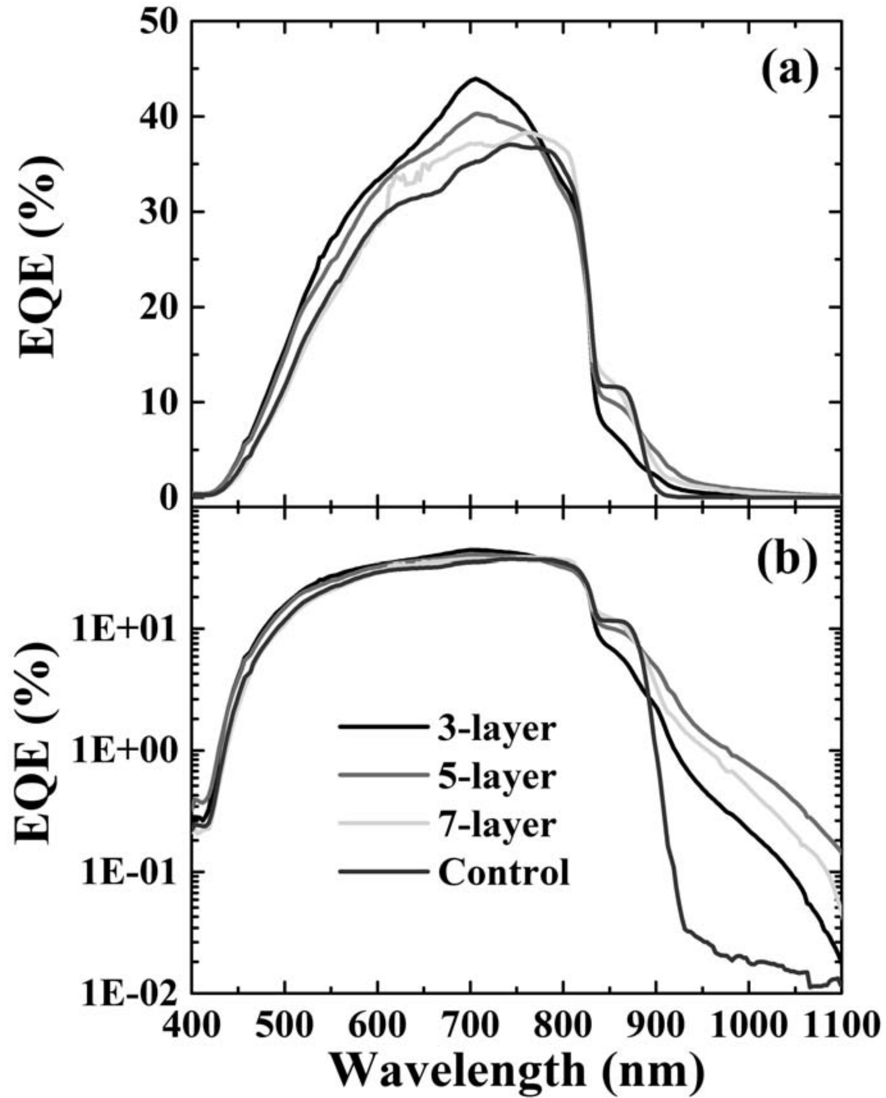

Figure 4.4: 77 K (a) linear scale and (b) log scale *EQE* measurements for the 3-layer (black line), 5-layer (red line), 7-layer (green line), and control cells (blue line).

the TD *PL* measurements where the GaAs and $GaAs_{0.86}Sb_{0.14}$ peaks are clearly evident in the control spectra (see Figure 3.15 (d)). The maximum *EQE* observed for all samples is around $\sim 40\%$, which is significantly lower than for the high quality GaAs materials even without anti-reflection coatings (around $\sim 65\%$ [89]).

This reduction of the EQE is attributed to the poor quality of the intrinsic and p-emitter regions, due to the formation of defects and dislocations induced by the 1.11% lattice mismatch between the GaAs substrate and $GaAs_{0.86}Sb_{0.14}$ matrix.

From Figure 4.4 (a) the carrier extraction from the $GaAs_{0.86}Sb_{0.14}$ matrix increases as the period of QD layers increases (black → green); such an increase is related to the thicker $GaAs_{0.86}Sb_{0.14}$ material in the 5- and 7-layer QD samples. The degradation (green → black) in the bulk GaAs region with thicker intrinsic region is consistent with more defects and dislocations in the matrix, which propagate into the GaAs emitter.

Despite bright *PL* indicating strong confinement of carriers in the QDs, all three QD samples show additional carrier extraction above ∼930 nm, which is not observed for the control cell. The enhanced extraction correlates to the QD transition (VB → IB). However, in order to preserve the V_{oc} the IB should not be coupled to CB continuum; thus, there should not be any carrier extraction in an ideal IBSC unless the two step photon absorption (TSPA) criteria is met. Since we have been using a "monochromatic" light, the carrier extraction from the QDs indicates that the IB is not isolated from the CB. The lack of an isolated IB is not a fundamental limitation of this system, but rather reflects the ability for carriers to escape from the QDs through either defect-mediated or tunneling processes.

As shown in Figure 4.5, TD *EQE* measurements were performed on all samples between 77 K and 350 K to further investigate the carrier extraction mechanisms. The absorption edge for both the GaAs and $GaAs_{0.86}Sb_{0.14}$ has a red shift which follows Varshni's relationship between the bandgap and the temperature. Apart

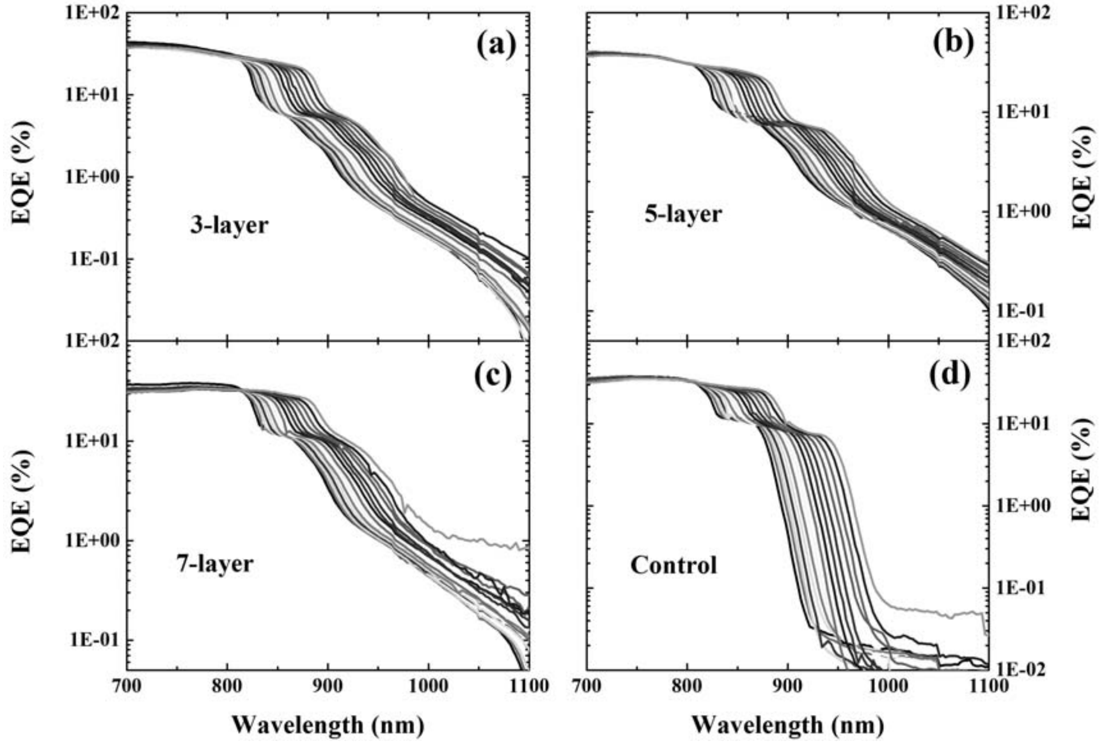

Figure 4.5: Temperature dependent *EQE* measurements for (a) 3-layer, (b) 5-layer, (c) 7-layer, and (d) control cells from 77 K to 350 K.

from the red shift, carrier extractions from QDs for all three QD samples also have a small enhancement (above $\sim$ 1040 nm). The possible explanation for this enhancement is the thermally assisted escape process, where the elevated temperature gives carriers sufficient thermal energy to escape from the QDs.

Figure 4.6 compares the *EQE* (black) and *PL* (red) spectra for the (a) control cell and (b) the 7-layer QD cell at 150 K. The correlation between the *EQE* and *PL* of the control cell indicates that the photogenerated carriers are indeed related to the GaAs (blue arrow) and $GaAs_{0.86}Sb_{0.14}$ (green arrow) transitions. Defect states observed in the *PL* measurements suggests the prevalence of defects in the control sample. As mentioned before, the intrinsic region of the control

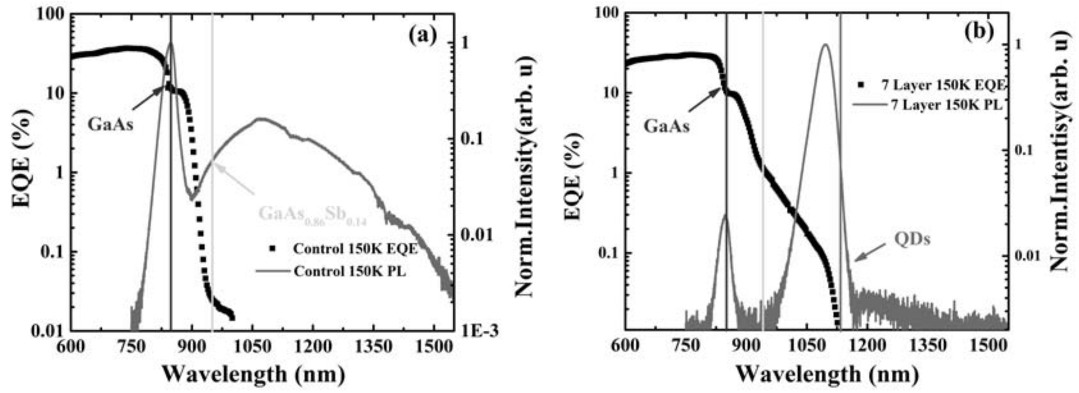

Figure 4.6: *PL* (red line) and *EQE* (black symbols) measurements for (a) control cell and (b) 7-layer QD cell at 150 K; GaAs, $GaAs_{0.86}Sb_{0.14}$, and QDs are labeled as blue, green, and red arrows respectively.

cell is $GaAs_{0.86}Sb_{0.14}$, which is 1.11% lattice mismatched with GaAs; without employing any strain balancing techniques, the matrix material contains many defects since the total thickness of the intrinsic region $\sim$ 270 nm is in excess of the critical value 10 $\sim$ 30 nm; these defects serve as non-radiative recombination centers (SRH recombination centers). As the temperature increases, the signal from $GaAs_{0.86}Sb_{0.14}$ quenches quickly; thermal broadening of both the GaAs peak and the defect band is also noted.

In comparison, the slight enhancement of the *EQE* related to the QD transition is observed in the 7-layer QD sample from $\sim$ 970 to 1100 nm. As the signal from the QDs dominate the whole *PL* spectra (Figure 4.6 (b)), both the $GaAs_{0.86}Sb_{0.14}$ and defect transitions are overwhelmed and therefore not as pronounced as in the control cell *PL* (Figure 4.6 (b)).

The noticeable mismatch between the absorption edge of the *EQE* and emission

edge of the *PL* for both cells may be explained by a slight temperature difference between the two cryostats we performed our *EQE* and *PL* measurements or that the *PL* reflects the lowest energy state while the absorption reflects the density of states.

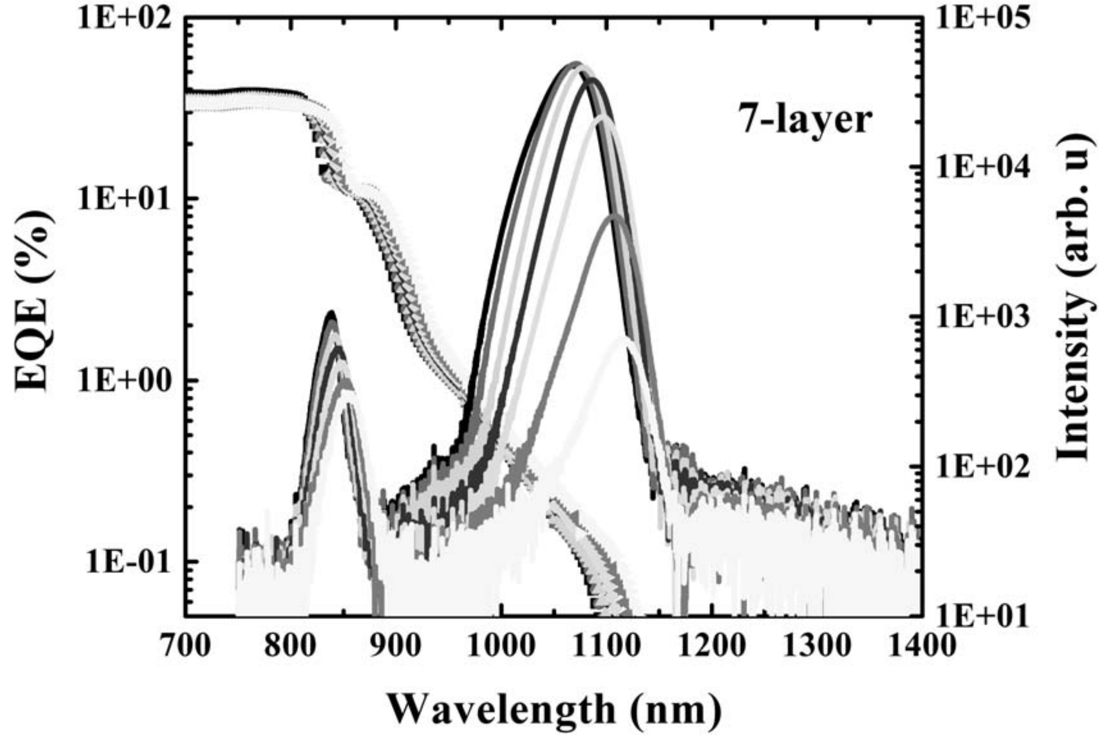

Figure 4.7: Temperature dependent *PL* (lines) and *EQE* (symbols) measurements for 7-layer QD sample.

To investigate the correlation between the recombination and collection of photogenerated carriers as a function of temperature, a comparison of the TD *PL* and the TD *EQE* data recorded between 77 K and 270 K for the 7-layer QD sample is shown in Figure 4.7. The QD transitions are evident in both measurements with a strong correlation between the two spectra. The red shift of both *PL* peak and *EQE* signals related to the GaAs and QDs is a result of the reduction of

the energy gap due to the thermal expansion of the lattice. The enhancement of *EQE* with increased temperature is driven by the thermally assisted carrier escape process and coincides with the rapid quenching of the *PL* signals at high temperatures. The carriers gain enough energy ($>$ *Activation energy* E_{a2}) to overcome the barriers within the QDs, and escape into the $GaAs_{0.86}Sb_{0.14}$ to be collected as photocurrent or recombine in the defect channels.

4.2.3 Electroluminescence Measurements

In addition to *PL* measurements, *EL* measurements were performed on the cells. An *EL* signal is not observed from 800 nm to 1700 nm for the control cell; the lack of an *EL* signal suggests that the delocalization and spatial redistribution of carriers in the intrinsic region and the efficient non-radiative recombination dominates in this control cell. Low injection level *EL* measurements for the 3-layer sample are also missing here due to poor contact issues after rebonding the Au wire onto the sample. This section will therefore only focus on the 5-layer and 7-layer QD samples.

Figure 4.8 shows *EL* spectra with different current injection levels for the 5-layer QD cell at 77 K (a), 150 K (b), and 210 K (c). A blue shift is observed for 77 K and 150 K measurements as the current injection increases; which correlates with the multimodal behavior of the QDs. As seen in the low temperature *PL* measurements, the nonuniform $InAs/GaAs_{0.86}Sb_{0.14}$ QDs exhibit an asymmetrical shape in the *PL* spectra due to competing subsets of QDs: a larger size has a smaller energy and vice versa. By increasing the injection level, lower energy

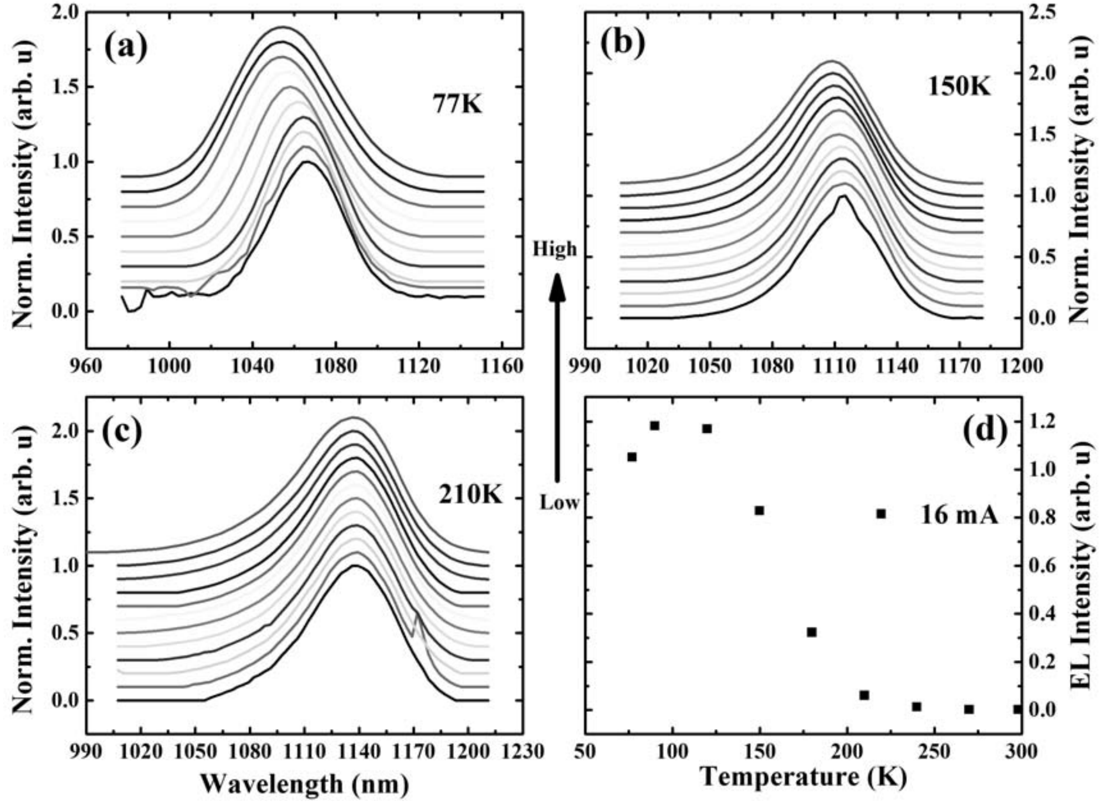

Figure 4.8: Current injection level dependent *EL* measurements for 5-layer QD sample at (a) 77 K (1 - 207 mA), (b) 150 K (1 - 207 mA), and (c) 210 K (1 - 207 mA); (d) The *EL* intensity at 16 mA injection level as a function of temperature.

states are saturated and the peak position reflects contributions from both the small and large QDs. At higher temperatures (above 150 K), the additional thermal energy redistributes the carriers among the QDs and results in a single degenerate energy level. Thus, the peak position remains relatively constant at the elevated injection level as evident in Figure 4.8(c), which shows the *EL* at 210 K. The peak intensity with a 16 mA injection level as a function of temperature is summarized in Figure 4.8(d). The peak intensity is relatively stable below 150

K; while quenching rapidly above 150 K.

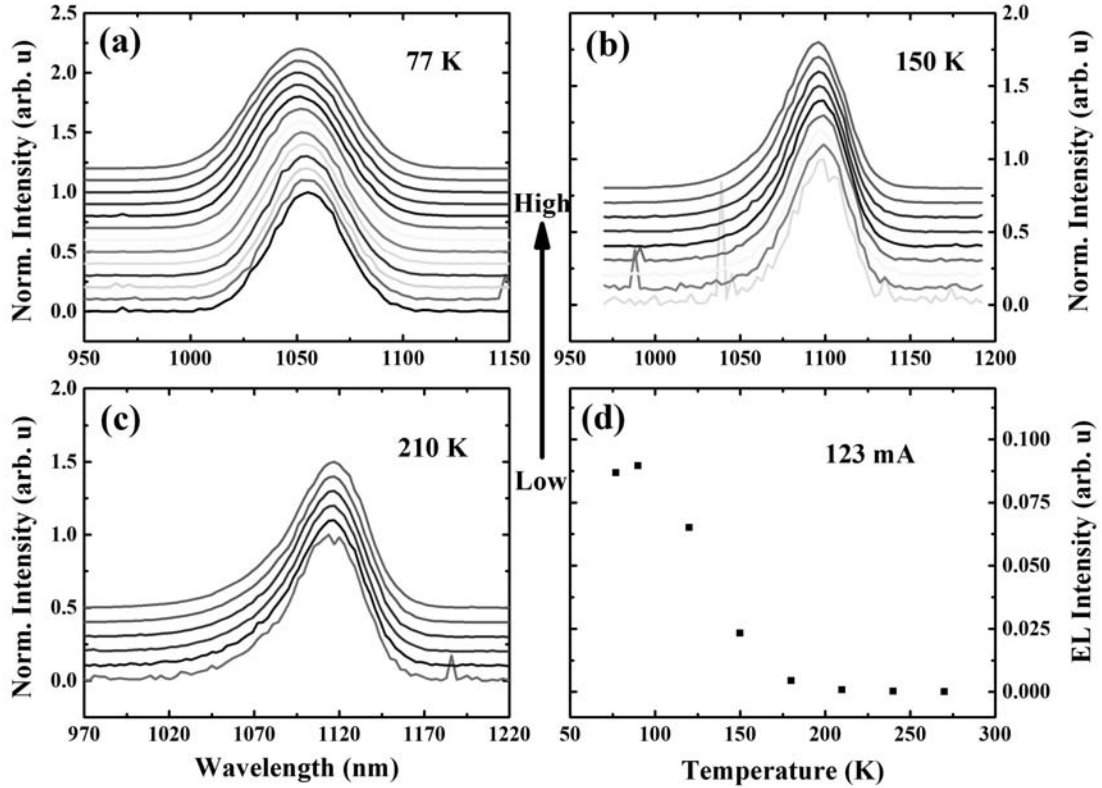

Figure 4.9: Injection level dependent *EL* measurements for 7-layer QD sample at (a) 77 K, (b) 150 K, and (c) 210 K; (d) The *EL* intensity at 123 mA injection level as a function of temperature.

In comparison, *EL* spectra with different current injection levels for the 7-layer QD cell at 77 K (a), 150 K (b), and 210 K (c) are shown in Figure 4.9. At 77 K, a blue shift is observed with increasing injection level similar to the 5-layer sample. However, such a blue shift is not seen at 150 K, which indicates efficient carrier redistribution and formation of degenerate energy levels at a lower temperature than for the 5-layer sample. This is consistent with the lower activation E_{a2} (see Table 3.2.2) extracted from the TD *PL* measurements (Figure 3.15).

The *EL* intensity with a 123 mA injection level as a function of temperature is

shown in Figure 4.9 (d). A fast quenching of the *EL* signal is observed above 120 K. This behavior, along with the rapid reduction of the *PL* intensity seen in TD *PL* measurements (Figure 3.16 (a)) provides further evidence for efficient carrier escape at elevated temperatures (> 120 K).

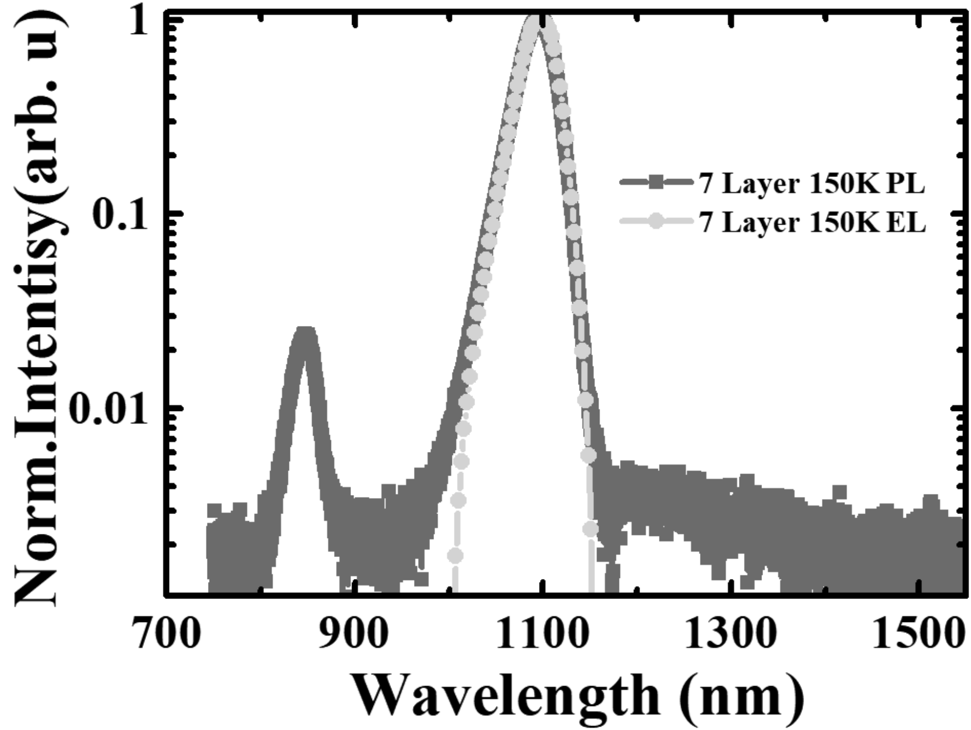

Figure 4.10: PL (red), and EL (green) spectra for 7-layer QD cell at 150 K.

Figure 4.10 compares the *PL* (red) and *EL* (green) spectra for the 7-layer QD cell at 150 K. At 150 K, the QD transition seen in the *EL* agrees with *PL* spectrum. However, the transitions related to GaAs (∼ 830 nm) and $GaAs_{0.86}Sb_{0.14}$ (∼ 910 nm) seen in the *PL* are absent from *EL* spectrum. The lack of these transitions in the *EL* spectrum reflects the direct injection of the carriers into the QDs or active regions. Since the wavelength of the excitation source used in the *PL* is 632.8 nm (higher energy than the GaAs bandgap), the top p-GaAs emitter and QDs are

probed simultaneously [31]; A large portion of the photons is absorbed within the emitter, which coupled with the spatial separation of the electrons and holes in the type-II QDs, contributes to *PL* from the continuum regions significantly.

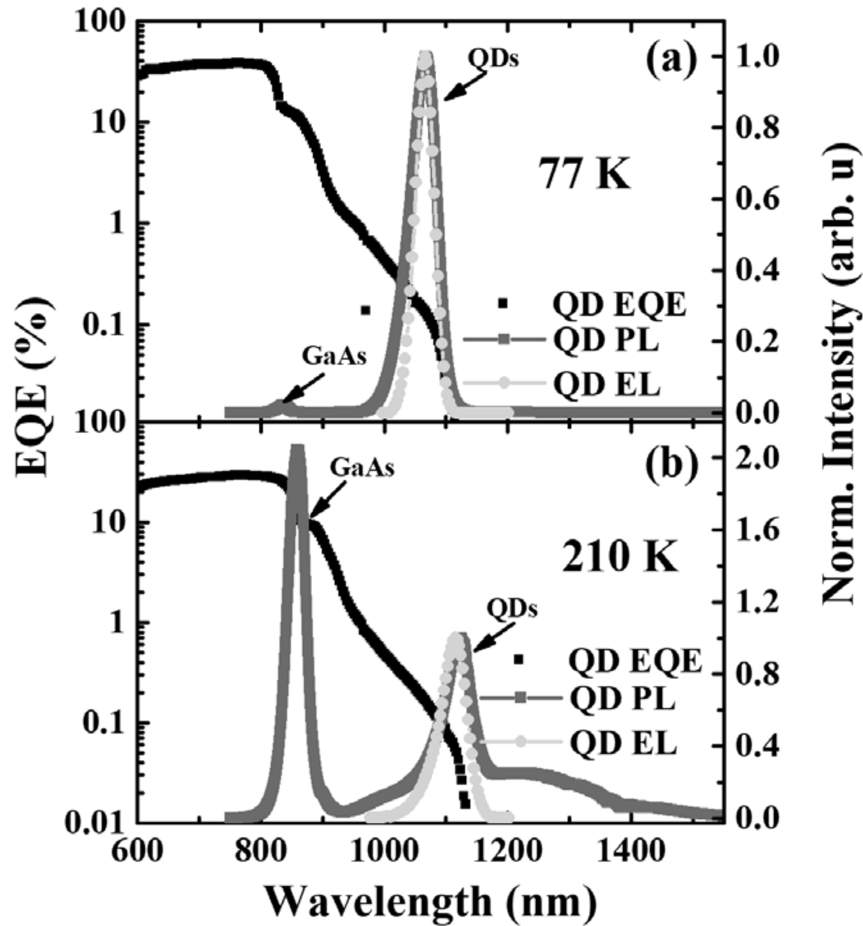

Figure 4.11: PL (red), and EL (green) spectra for 7-layer QD cell at (a) 77 K, and (b) 210 K. Reprinted from Yang et al. *IEEE JPV* (in press).

A comparison of the *EQE*, *PL*, and *EL* of the QD cell at 77 K (a) and 210 K (b) indicates that the enhancement of the photocurrent as seen in the *EQE* comes from the QD transition (above 950 nm) in the active region of the device. The PL and EL spectra have been normalized to the QD peak. At 77 K, the

QD transition dominates the *PL* spectra; the absence of GaAs and $GaAs_{0.86}Sb_{0.14}$ signals in the *EL* measurements suggests the QDs have more efficient radiative recombination than the matrix and emitter materials.

At 210 K, the peak intensity of the QDs has a three orders of magnitude reduction and the low energy defect states (950 - 1550 nm) become evident and contribute to the *PL* spectra. As the temperature is increased above 210 K, the defect band transition dominates the *PL* and quenches the QD transition. The lack of the defect band in *EL* measurements is due to the direct injection and relatively large carrier concentration in the active region.

Based on the *PL*, *EL*, and *EQE* measurements, the carrier recombination processes are divided into two regimes: (1) a low temperature regime, where the carriers are isolated in the QDs and the radiative recombination within the QDs is more efficient; (2) a higher temperature ($>$ 120 - 150 K) region, where the elevated temperature introduces additional thermal energy which facilitates carrier escape from the QDs, reduces radiative recombination, and increases SRH recombination through thermally activated defect states or the ionized impurities in the matrix material.

To further investigate this hypothesis of thermally mediated transition from radiative to non-radiative processes, the spontaneous emission in *EL* measurements is analyzed to determine the nature and dominant mechanisms of the recombination processes at different temperatures. The current injected into an electrical device

can be approximated by [90]:

$$I = eV(An + Bn^2 + Cn^3) + I_{leak}. \quad (4.1)$$

Where A, B, and C are coefficients for single carrier recombination (n), radiative recombination (n^2), and Auger recombination (n^3), respectively [90]. V is the volume of the active region. A single carrier recombination is usually due to the non-radiative recombination processes via traps and defects (SRH) [90]; radiative recombination is associated with the spontaneous emission. Normally, spontaneous emission is approximated by the EL (below the lasing threshold for laser devices). The total integrated spontaneous emission rate L has a linear relationship with the radiative recombination n^2. Thus, the carrier concentration n is directly proportional to $L^{1/2}$. Then, equation 4.1 can be rewritten as [90]:

$$I \propto n^z \propto L^{1/2^z}. \quad (4.2)$$

When the current from the radiative recombination $eV \times Bn^2$ dominates, the z-factor will be close to 2 ($\propto n^2$). However, if z is close to 1 ($\propto n$), this indicates the injected current is lost in terms of SRH recombination current $eV \times An$. By plotting $ln(I) - ln(L^{1/2})$, the z-factor is extracted directly from the slope of a linear fit to determine the nature of the dominant recombination processes.

The $ln(I) - ln(L^{1/2})$ plots for the 7-layer QD sample at various temperatures are shown in Figure 4.12 (a). The linear fits of the plots with increasing temperature clearly display different gradients: a steeper slope reflects a larger z-factor. Figure 4.12 (b) summarizes the z-factors for the 5-layer and 7-layer QD samples as a function of temperature. The difference of the slopes suggests different dominant

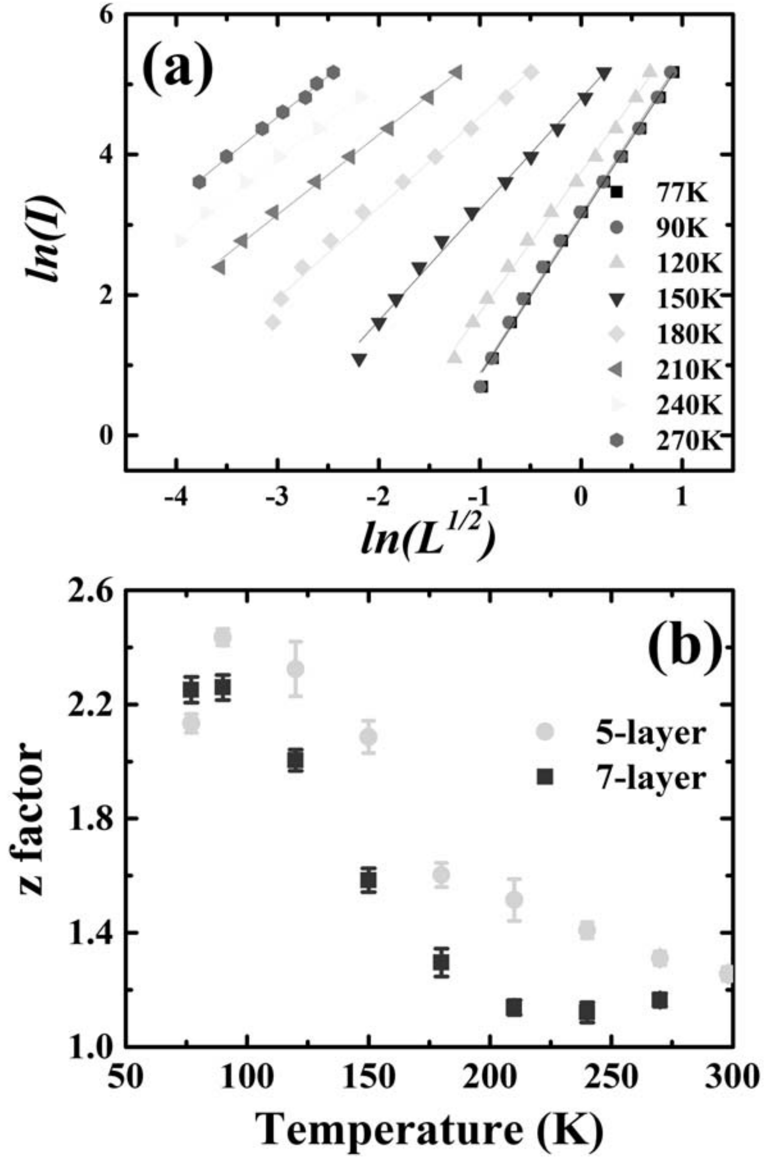

Figure 4.12: (a) $ln(I) - ln(L^{1/2})$ plots for the 7-layer QD sample at various temperatures; (b) z-factors extracted for 5-layer and 7-layer QD samples.

recombination process in different temperature regimes. At low temperature (T $<$ 150 K for 5-layer sample and $<$ 120 K for 7-layer sample), z-factors of $\sim$ 2 are observed, which indicates that the radiative recombination process is dominant. Although a z-factor larger than 2 suggests a contribution of the non-radiative

Auger recombination, which may be invoked at T < 100 K in Figure 4.12 (b), such processes are not considered significant here. Auger processes are usually problematic at high injection levels for small bandgap materials. However, Auger processes are considered negligible due to the relatively large IB and VB separation and high radiative recombination rate. Here, a value of $z > 2$ at T < 120 K is rather attributed to multimodality in the QDs at lower temperatures (see Figure 4.8 and Figure 4.9).

At the high temperature regime (T > 150 K for 5-layer sample and > 120 K for 7-layer sample), a rapid reduction of the z-factor towards $z = 1$ is evident. Such a behavior indicates that SRH (non-radiative) recombination becomes dominant, which is consistent with the rapid quenching of the EL and PL intensity and the massive reduction of the V_{oc} above 150 K. Compared with the 7-layer sample, the relatively larger z-factor observed for the 5-layer sample reflects a larger activation energy E_{a2} (Table 3.2.2) which corresponds to a weaker thermally activated escape process.

The temperature dependent z-factor behavior further supports the hypothesis that there is a thermally activated transition from radiative to non-radiative processes with increasing temperatures. Above 150 K, thermally activated carriers from the QDs are trapped in SRH recombination centers in the matrix and thus not collected effectively, similar to the limited performance of the control cell. At higher temperature, higher injection currents are required to produce reasonable EL. This behavior provides further evidence for the localization of non-intentional impurities at lower temperatures; these activated impurities at

higher temperatures increase the concentration of SRH recombination centers.

4.3 Conclusion

In this chapter, four p-i-n GaAs solar cells with different intrinsic region designs were investigated using complementary *EL*, *EQE*, and *J-V* measurements. Defect states associated with the 1.11% lattice mismatch between $GaAs_{0.86}Sb_{0.14}$ and GaAs account for the limited performance of the solar cell. The hypothesis that there is a transition from radiative to non-radiative dominant recombination is proposed and supported by the rapid quenching of the *PL* and *EL* intensity, along with a simultaneous decrease in the z-factor from 2 to 1 (above 150 K) in the spontaneous emission analysis. Such a performance degradation with increasing temperatures is a result of the thermal activation of the defects or ionization of impurities in the lattice. These results further suggest the prevalence of non-radiative processes at elevated temperatures in these systems, which qualitatively correlates with the TD *EQE* and *J-V* data presented.

Chapter 5

Investigation of the Non-linearity of the Diode Characteristics in PbS/ZnO Quantum Dot Solar Cells

Quantum dots have been suggested as promising materials for potential photovoltaic applications. The InAs/GaAsSb quantum dot solar cells studied in the previous two chapters have been investigated to achieve higher efficiencies, but are still relatively expensive. However, numerous groups have been working to implement colloidal quantum dots for low cost thin film solar cell applications.

Lead chalcogenide quantum dots (such as PbS [60–63], PbSe [64,65]) have been used to fabricate CQD solar cells and have shown improvement in both efficiency and stability over the past few years. Dr. Sargent's group has now achieved a power conversion efficiency (PCE) more than 11.4% [70]. The relatively high efficiencies and low cost solution synthesis techniques make lead chalcogenide QDs a promising candidate for solar cell applications. Incorporation of MEG processes [66, 67] and tandem structures [68] in lead chalcogenide QD solar cells (referred as "CQD solar cells" later in this chapter) has the potential to further improve the efficiency of these CQD solar cells.

However, several artifacts such as a strong leakage or reverse bias "turn on" [91, 92] and a crossover characteristic when comparing dark and light J-V measurements [91, 92] degrade the performance of CQD solar cells and result in a PCE significantly lower than the Shockley-Queisser limit [8]. The defect states

formed on the QD surface pin the Fermi level at mid-gap states [91,93,94], leading to a formation of a Schottky barrier between the QD layer and the metal contacts; such a non-ideal barrier hinders the carrier transport and induces a non-ohmic transport behavior which deteriorates the performance of these solar cells.

In this chapter, the transport and optical properties of PbS/ZnO solar cells were studied with current-voltage, external quantum efficiency, absorbance, capcitance-voltage, and impedance measurements. A phenomenological description that incorporates back-to-back diodes with leaky resistances [91] has been used to model and qualitatively describe the non-ohmic behavior observed in both forward and reverse bias from these solar cells.

This chapter is based on the Yang et al. published paper *ACS Applied Materials & Interfaces* 9.15 (2017): 13269-13277.

5.1 Experimental Details

5.1.1 PbS/ZnO Quantum Dot Thin Film Deposition and Solar Cell Fabrications

Colloidal PbS QDs synthesis. 0.46 g of lead oxide (PbO), 2.0 g of oleic acid (OA) and 12.5 g of 1-octadecene (ODE) were added to a three-neck flask. The mixture was heated to 120°C while stirring under a N_2 purge. 210 μL of hexamethyldisilathiane [TMS], was mixed with 2 mL of ODE in a glove bag over-pressured with N_2. Then, using a syringe the TMS solution was rapidly injected into the hot PbO/OA/ODE solution flask. Soon after the mixture turned

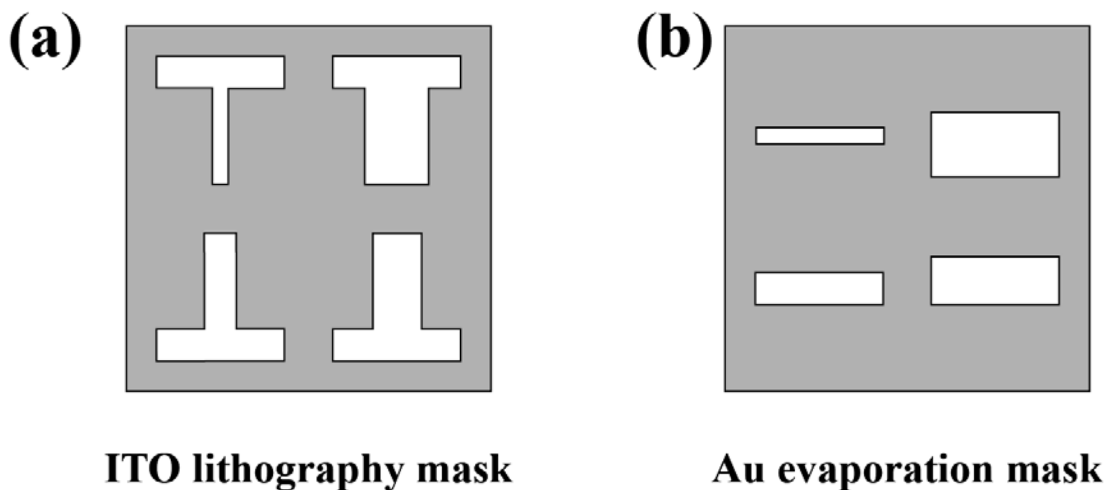

Figure 5.1: Schematics of (a) photo-lithography mask for patterning ITO substrate and (b) evaporation mask for thermal evaporation of top contact.

black, by removing the heater and putting the flask in a cold water bath - the reaction was ceased. The synthesized PbS QDs solution were cooled to room temperature. Next, the reaction solution were precipitated with acetone and then centrifuged. Afterwards, the clear supernatant was decanted. Hexane and methanol were used three times for additional purifications. Finally, the QDs capped with long OA ligand were suspended in toluene (70 mg/mL).

ITO prepattern. Photo-lithography was used to prepattern the indium tin oxide (ITO) coated glass substrates. First, the ITO substrate was cleaned in each solvent for 10 mins using an ultrasonic bath; the order of solvent used is Decon Neutrad detergent, acetone, and isopropanol. The substrate was then baked at 150°C for 10 mins to remove residue moisture. Photoresist AZ-5214E was then spin-coated on the substrate at 4000 RPM for 40 seconds. The substrate was

then soft baked for 60 seconds at 95°C on a hot plate to remove the solvents and harden the photoresist film. Next, the photoresist was exposed with ultraviolet (UV) radiation for 2.5 seconds using a standard Xenon bulb (275 W) via a mask as shown in Figure 5.1 (a) to define the ITO back electrodes. The substrate was then baked on a hot plate for 90 seconds at 120°C to activate the crosslinking agent and create a pattern that is insoluble in etchant and developer. This process was then followed by a flood exposure under UV radiation for 50 seconds without the mask to make the previous unexposed photoresist soluble in developer. The unwanted photoresist was then removed in MF-726 developer for 60 seconds. The sample is then rinsed with deionized (DI) water for 2 minutes and dried with N_2 gas. The ITO substrate was then immersed in an etchant solution composed of $HCl{:}H_2{:}HNO_3$ (with a volume metric ratio 4:2:1, respectively) for 10 mins to remove the unwanted ITO. The patterned substrate was sonicated in acetone and isopropanol to remove the photoresist pattern. Finaly, Decon Neutrad detergent, deionized water, 5% NaOH, deionized water, and isopropanol were used in succession to clean the ITO.

Device fabrication. ZnO nanocrystals in n-butyl acetate (Sigma Aldrich Inc.) were spin-coated on top of the prepatterned ITO/Glass substrate and annealed at 700°C for 10 s. A PbS QD film was deposited onto the ZnO film via a standard layer-by-layer spin-coating process: firstly, 200 μL of PbS QD solution (diluted to 25 mg/mL) was spun at 2000 RPM; secondly, to exchange the long chain OA ligand with a short chain ligand, 200 μL of 1,2-ethanedithiol (EDT short chain

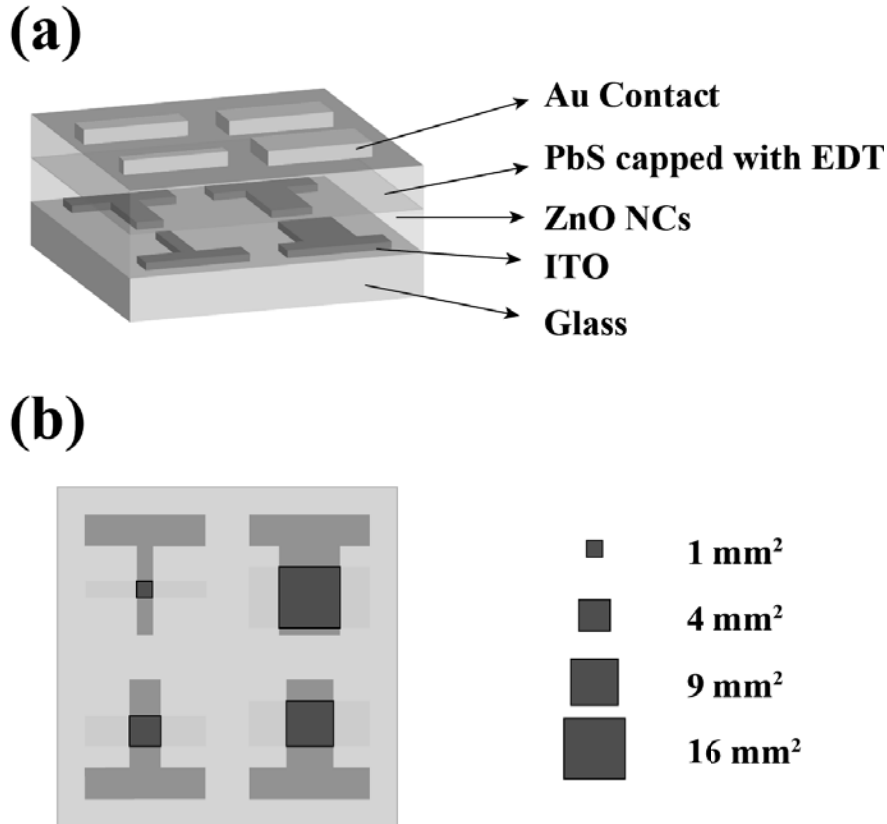

Figure 5.2: Schematic (a) Off-axis and (b) top views of the PbS/ZnO QD solar cells.

ligand)-acetonitrile solution was dropped on the film and then spun at 2000 RPM to exchange the cap ligand; thirdly, acetonitrile and hexane solvents were spun sequentially at 2000 RPM to wash away the excess QDs and EDT. This process was repeated 10 times. Finally, a shadow mask (Figure 5.1 (b)) was used to define four rectangular Au contacts; the Au deposition was accomplished at a deposition rate of 2 Å/s and base pressure of 4×10^{-7} Torr using a Kurt J. Lesker Nano 36 thermal evaporator. The thickness of ZnO and PbS layers are 134 ± 4 nm and 185 ± 5 nm, respectively; based on cross-sectional scanning electron microscopy carried out on similar structures. A schematic of the device architecture is shown Figure 5.2. Four solar cells with four different areas (Figure 5.3 (b) red squares)

were made at the same time.

Another graduate student M. D. C Whitaker in our lab and Prof. Lloyd Bumm helped with the fabrication of PbS/ZnO CQD solar cells.

5.1.2 Characterization techniques

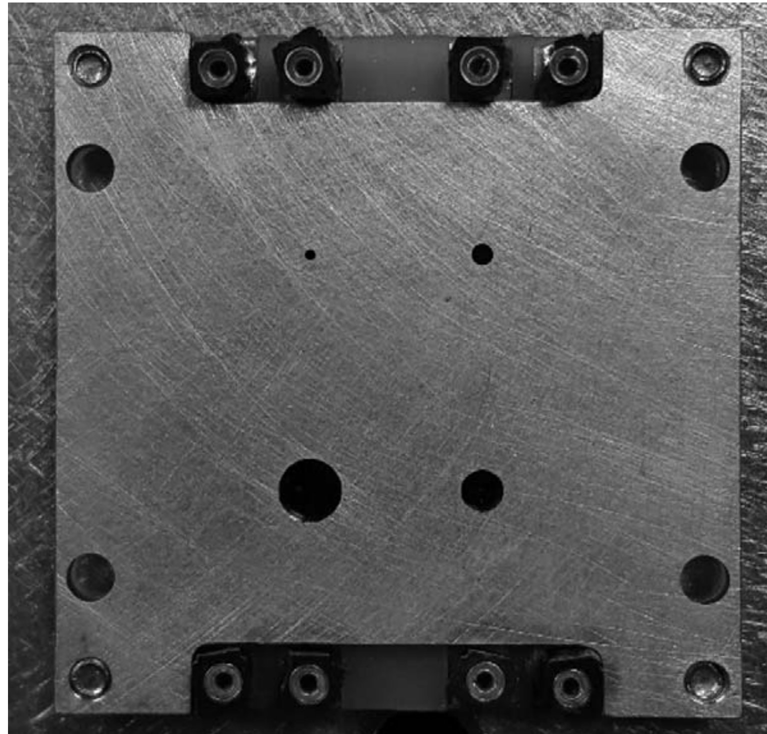

Figure 5.3: PbS/ZnO QD solar cells with exposure masks on for electrical measurements.

J-V, *EQE*, *C-V* and impedance spectroscopy measurements were performed using the setup described in Chapter 2. A mask with illuminated area smaller than the actual device is used to minimize the edge effects. The final PbS/ZnO QDSC is shown in Figure 5.3. A Cary 50 Conc UV-Visible spectrophotometer was used for the PbS QD solution absorbance measurements.

5.2 Experimental Results and Discussions

5.2.1 Absorption Measurements

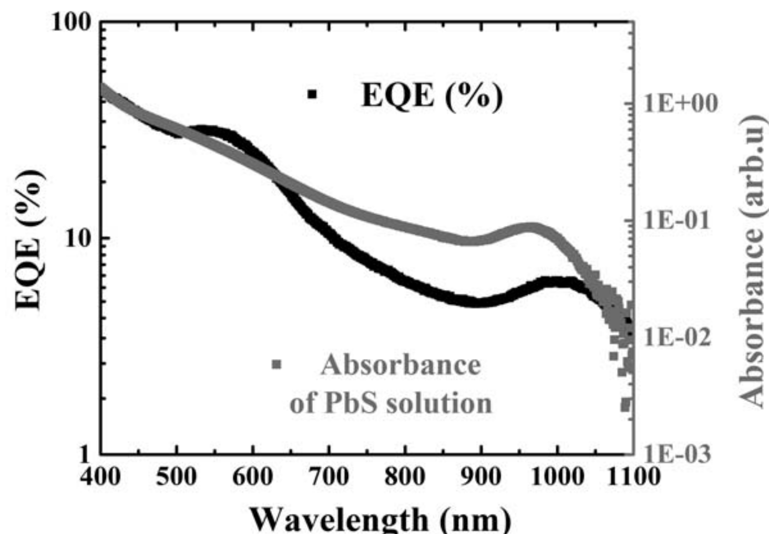

Figure 5.4: PbS/ZnO QD solar cells with exposure masks on for electrical measurements. Reprint from Yang et.al. *ACS Applied Materials & Interfaces* 9.15 (2017): 13269-13277.

Figure 5.4 displays the absorbance measurements (red) of the PbS QD in toluene and the *EQE* measurements (black) of the PbS/ZnO solar cells from 400 nm to 1100 nm. Both of these absorption measurements show a similar energy spectra. The absorbance measurement (red) exhibits a well-defined excitonic peak $\sim$ 970 nm; in contrast, the photogenerated carriers extracted from the PbS QD layer show an excitonic peak centered at 1030 nm in the *EQE* (black). Such an offset of the excitonic peak position reflects a difference in confinement of the PbS QD solution and the solar cell structure. As noted in the experimental details, the PbS QDs in toluene are capped with OA ligands to protect the QDs while

EDT is used in the PbS QD layer to enhance the conductivity of the PbS QD film. OA is a longer ligand than EDT as such, it provides greater confinement since the QDs are less coupled.

5.2.2 *Current-Voltage* Analysis

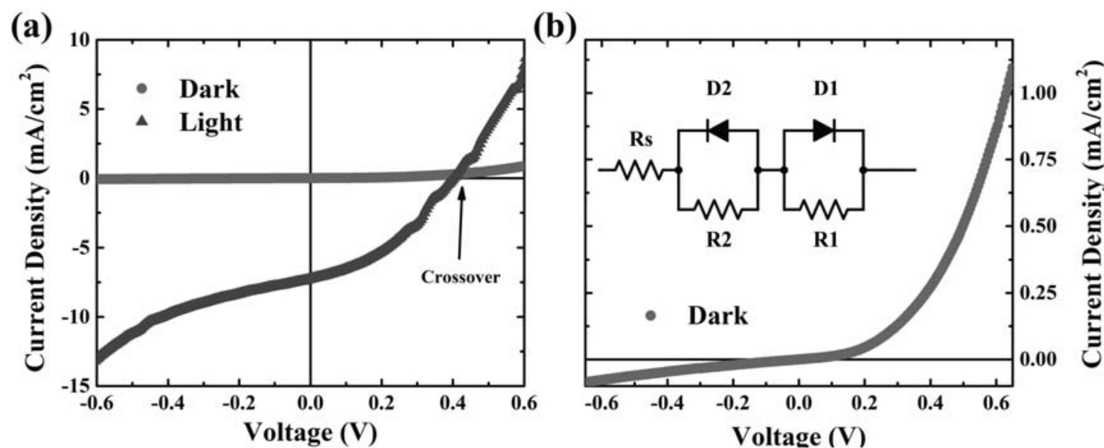

Figure 5.5: (a) Dark and Light *J-V* measurement results; (b) Zoom in of Dark *J-V* measurement data, inset is the back to back diode model used to predict this dark *J-V* behavior. Reprint from Yang et al. *ACS Applied Materials & Interfaces* 9.15 (2017): 13269-13277

The *J-V* measurement results under both dark and illuminated (1-sun) conditions are shown in Figure 5.5 (a). Three distinctive features are observed from these data: first, a high leakage current under high reverse bias (light *J-V*), which results in a relatively low $J_{sc} \sim 7.4\ mA/cm^2$; second, the dark and light *J-V* curves crossover above the $V_{oc} \sim 0.42$ V (arrow in Figure 5.5 (a)); third, there is rectification under both reverse and forward bias conditions (more noticeable in light *J-V* curve). These behaviors suggest the existence of an unintentional

barrier to carrier transport, which serves as a second diode in series to the main p-n heterojunction: n-ZnO/p-PbS junction. The origin of the second diode is most likely related to a Schottky barrier formed at the PbS/Au interface due to Fermi level pinning. This second diode shifts the global dark operating voltage of the device to a higher voltage. The 1-sun illumination helps to passivate the trap states at the interfaces and recover the true operating voltage, resulting in a crossover between the dark and light J-V curves. Such a crossover is not unusual in these type of devices, it has also been reported by several other groups as well [91, 92, 95].

Figure 5.5 (b) is a magnified plot of the dark J-V, which further illustrates the leakage current that is evident at high reverse bias; the leakage current observed in the dark measurement is similar to the illuminated measurement (Figure 5.5 (a)), also indicating unintentional rectification of a second diode in the structure. Due to the different polarity of the competing rectifications, a back to back diode model (Figure 5.5 (b) inset) is used to develop a phenomenological description of the ZnO/PbS solar cell J-V behavior. D1 and D2 represent the main heterojunction (n-ZnO/p-PbS) and unintentional second diode, respectively; R1 and R2 are the associated shunt resistances. Rs represents the series resistance of the whole device. The shunt resistance R2 associated with this second junction (in reverse bias) results in a loss of photogenerated current and therefore a smaller J_{sc} than with a conventional ohmic contact.

Figure 5.6 shows the dark $J - V$ measurement (black symbol) at 300 K and a

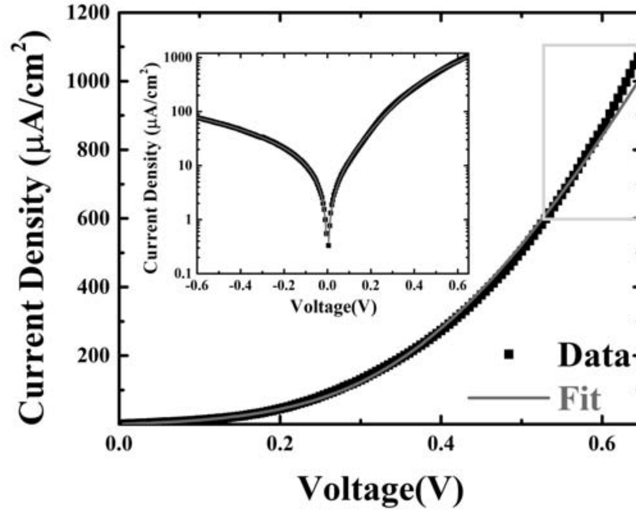

Figure 5.6: One diode model fitting for dark J-V measurements (data - black symbols, fitting - redline); inset is the semi-log plot of dark J-V data. Reprint from Yang et al. *ACS Applied Materials & Interfaces* 9.15 (2017): 13269-13277

theoretical fit (red-line) based on Equation 5.1

$$J = J_0 \cdot [exp(\frac{q(V - IR_s)}{n_k T}) - 1] + \frac{V - IR_s}{R_{sh}}, \tag{5.1}$$

is used to fit the data. J_0, R_s, R_{sh}, n, k, and T represent the dark saturation current, series resistance, shunt resistance, ideality factor, Boltzmann constant and temperature, respectively. For an ideal diode, an ideality factor of $n = 1$ suggests SRH (one carrier) or direct band to band (1 minority carrier) recombination in the bulk region (not the depletion region); an ideality factor of $n = 2$ suggests two-carrier recombination in the space charge region. The forward bias and reverse bias regime are fit separately due to the existence of double diodes. The competing processes between the carrier drift-diffusion and recombination in space charge or

neutral region normally result in ideality factors between 1 and 2.

By fitting the dark J-V curve a value of $n = 3.54$ is extracted. Generally, $n > 2$ is considered unphysical for a single homogeneous junction, but has been attributed to the contribution of multiple rectifying diodes in series in less homogeneous systems; it has been discussed extensively in the literature, particularly for GaN-based LEDs [96, 97]. The Shockley diode equation can be rewritten as the summation of multiple Shockley equations:

$$V = \sum_i V_i = \frac{kT}{q} \sum_i [n_i(\ln J - \ln J_{0,i})], \tag{5.2}$$

where, multiple diodes are denoted by index i; J_0, k, and T represent the reverse saturation current, Boltzmann constant, and temperature, respectively. n_i is the ideality factor for junction i. In structures that have multiple competing diode behaviors, the effective n for the device is then [96, 98–100]:

$$n = \sum_i n_i. \tag{5.3}$$

The V_{oc} extracted (∼0.41 V) is significantly lower than bandgap of the PbS QDs (1.2 eV). Based on Equation 2.1:

$$V_{oc} = \frac{nkT}{q} \ln(\frac{J_P}{J_0}), \tag{5.4}$$

the small V_{oc} is attribute to a high dark saturation current J_0. Such a reduction of V_{oc} can also be explained by an increase of the SRH recombination current. The leakage of the dark J-V curve in the reverse bias regime (Figure 5.6) suggests defect-assisted carrier tunneling directly across the junction which is often assisted by defects [97, 101, 102]. The high density of surface states of PbS QDs serves as

a shallow tunneling channel; under reverse bias, the large electric field across the PbS/ZnO interface facilitates defect mediated tunneling process and results in large current transport analogous to the avalanche breakdown processes.

Figure 5.7: Schematic band alignments of both main junction (1) and Schottky diode (2) at equilibrium

As has been described previously, a Schottky diode at the PbS/Au interface accounts for the multiple diode behavior and high ideality factor. A schematic band diagram of the PbS/ZnO solar cell in equilibrium is illustrated in Figure 5.7. The main n-ZnO/p-PbS heterojunction and p-PbS/Au Schottky diode are labeled as junctions 1 and 2. This unintentionally formed Schottky diode and the main heterojunction operate in series. Ideally, the PbS/Au contact should be ohmic allowing efficient extraction of photogenerated carriers. However, the large surface to volume ratio of the PbS QDs and prevalence of surface states in these nanostructures result in Fermi level pinning (Figure 5.7 black dots

) [91, 93, 94, 103] and a barrier to hole extraction from the active region in equilibrium, as illustrated in Figure 5.7. Since the EDT capped PbS QDs are nominally p-type, the consequent diode at the PbS/Au contact interface is a p-type Schottky diode in a serial connection to the main heterojunction with the *opposite polarity* as shown in the inset to Figure 5.5 (b).

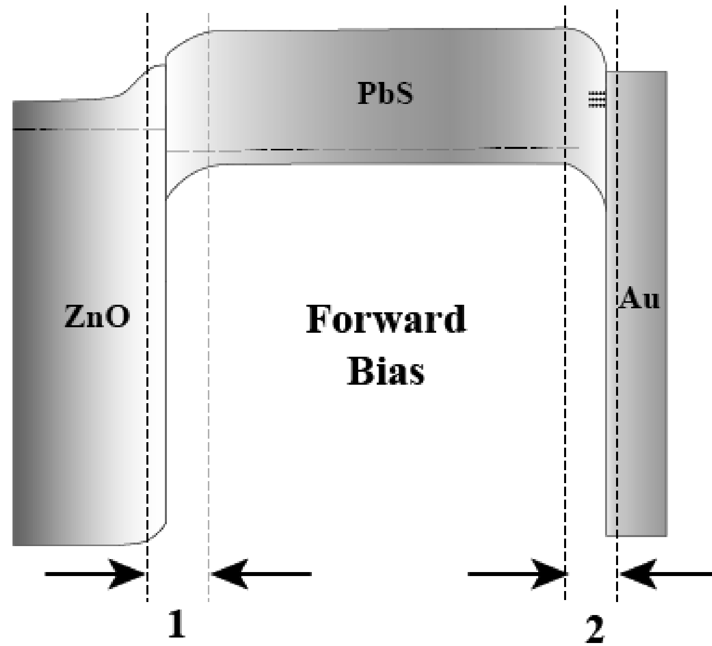

Figure 5.8: Schematic band alignments of both main junction (1) and Schottky diode (2) at forward bias.

Figure 5.8 shows the schematic band alignments for both the main heterojunction and the p-type Schottky diode under forward bias (reverse bias for the Schottky diode). Under forward bias conditions, the depletion width of the heterojunction (junction 1 in Figure 5.8) is reduced, while simultaneously - the depletion width of the p-type Schottky diode (junction 2 in Figure 5.8) increases

due to interfacial states present at this junction. As the applied forward bias voltage increases to a critical level, the actual reverse bias across the Schottky junction results in a narrowing of the Schottky barrier, allowing holes to tunnel through the PbS/Au interface by thermionic field emission [104]. This results in an excessive current across the device (shown in Figure 5.6 green square) in the nominal forward direction of the PbS/ZnO heterojunction.

This hypothesis is consistent with the observed crossover (see Figure 5.5) of dark and illuminated J-V curves, where the *additional* Schottky barrier is resistive to the holes transport until a critical forward bias (actual reverse bias for Schottky diode) which enables efficient thermionic field emission of holes. Those surface states are passivated by the photogenerated carriers under illumination and reduce the influence of Fermi-level pinning near the PbS/Au interface; therefore, effectively lowering the Schottky barrier height in comparison with dark measurements. This qualitative description also coincides with the lack of a natural logarithmic J-V characteristics under illumination that has been observed by several groups [91–94]. To address the Fermi level pinning at the PbS/Au interface, MoO_x has been used to passivate the PbS/Au interface states, resulting in an improved quality of the rectification [92], albeit with an increased series resistance.

The band alignment for the two junctions under reverse bias (actual forward bias for the Schottky diode) is illustrated in Figure 5.9. Under reverse bias conditions, the depletion width of n-ZnO/p-PbS junction increases, and the large electric field across the active layer inhibits the majority carrier transport: the device will be nominally off. In contrast, the reverse bias (actual forward bias)

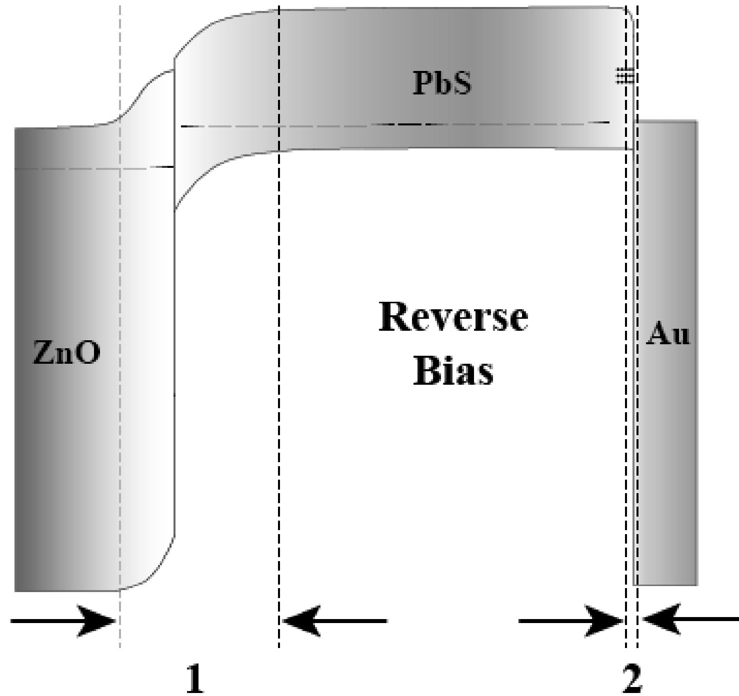

Figure 5.9: Schematic band alignments of both the main junction (1) and Schottky diode (2) at reverse bias.

across the PbS/Au interface reduces the depletion width and the Schottky barrier height at this junction, allowing efficient carrier injection from the contact. As the reverse bias increases, the field across the main PbS/ZnO junction will increase and offset the quasi Fermi level splitting to a critical level in which majority carriers can directly tunnel through the main junction, resulting in a reverse breakdown. Such a reverse breakdown is reflected in our *J-V* measurements (Figure 5.5 (b)) with increasing reverse voltage, it is also seen even in those PbS QD solar cells with high efficiencies; where, a relatively small (in comparison with silicon solar cells and III-V solar cells) reverse bias (-1 $\sim$ -2 V) voltage results in

a strong leakage current and an avalanche-type breakdown.

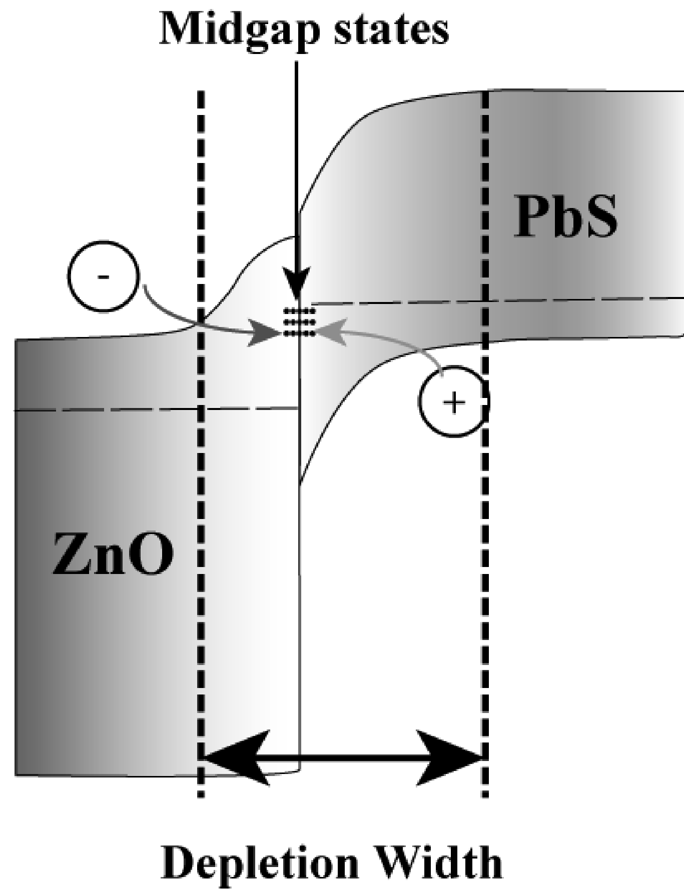

Figure 5.10: Schematic plot of defect mediated tunneling mechanism across the PbS/ZnO heterojunction.

The origin of this breakdown is related to the midgap state assisted tunneling process. Figure 5.10 illustrates the defect mediated tunneling mechanism across the PbS/ZnO heterojunction. The combination of vacancies at the ZnO surface [105] and unpassivated surface states of PbS QD surface contribute to a huge number of midgap interfacial states at the PbS/ZnO junction [106]. When the reverse bias is high enough to make the barrier thin enough, injected electrons and holes will tunnel through the midgap states, resulting in a leakage current. Such

a leakage current is evident in Figure 5.5 (a) and (b) with increasing reverse voltage; this significantly degrades the PCE in terms of the reduced photocurrent J that can be extracted (light J-V in Figure 5.5 (a)). Surface treatments for ZnO [106–108] have been used to improve the photocurrent extraction and reduce the shunting [92, 109]. An UV photodoped ZnO layer sees an increase of doping concentrations and helps push the depletion region more into the p-type PbS QD layer [109], which facilitates the hole extraction through a improved electric field within the PbS layer.

5.2.3 Mott-Schottky Analysis

Mott-Schottky (MS) analysis is used to further study the electrical properties of PbS/ZnO solar cells. By measuring the response of C-V, the doping densities and built-in potential can be determined by performing a linear fit of the MS plot ($1/C^2$-V plot). The depletion region has no free carriers and there are equal number of diffused minority carriers in both the p- and n- portions of the space charge region for a normal p-n junction in equilibrium. A variation of bias will change the depletion width and total number of carriers in the space charge region, this results in a change of capacitance behavior. Such a C-V characteristic can be modeled by a parallel plate capacitor. The depletion width w of a parallel plate capacitor is given by [110]:

$$w = \frac{A\epsilon}{C}, \tag{5.5}$$

Where C represents capacitance, ϵ and A are the permittivity and device area, respectively.

The depletion capacitance of a p-n junction is described by [110]:

$$\begin{aligned} C &= \frac{\epsilon}{w} \\ &= \sqrt{\frac{q\epsilon}{2\epsilon(V_{bi} - V)} \frac{N_a N_d}{N_a + N_d}}, \end{aligned} \tag{5.6}$$

where N_a, N_d, and V_{bi} are acceptor, donor concentration, and built-in potential of the p-n junction. For semiconductor-metal junctions, N_d is typically $>>$ N_a thus, the depletion width of the junction can be approximated by:

$$w = \sqrt{\frac{2\epsilon(V_{bi} - V)}{qN_a}}. \tag{5.7}$$

Combining equation 5.5 and 5.7, the C-V relationship is then expressed in terms of the Mott-Schottky Equation:

$$\frac{1}{C^2} = \frac{2(V_{bi} - V)}{A^2 q\epsilon N_a}. \tag{5.8}$$

Electric properties such as V_{bi} and N_a can be determined through a linear fit of Mott-Schottky plot ($1/C^2$-V plot).

C-V measurement data and corresponding $1/C^2$-V plots at five different frequencies are shown in Figure 5.11 (a) and (b), respectively. The response of C-V and MS plots are dependent on the modulation frequency. Both the capacitance value and the shape of the C-V and $1/C^2$-V curves change with increased frequency. Such a dispersion in the capacitance indicates that the charging and discharging processes of carriers are affected by the modulation frequency, which suggests trapping and detrapping of carriers related to the localized states is introduced by the defects in these type of devices. Material systems with prevalence of localized states, such as CQD [111] devices, organic

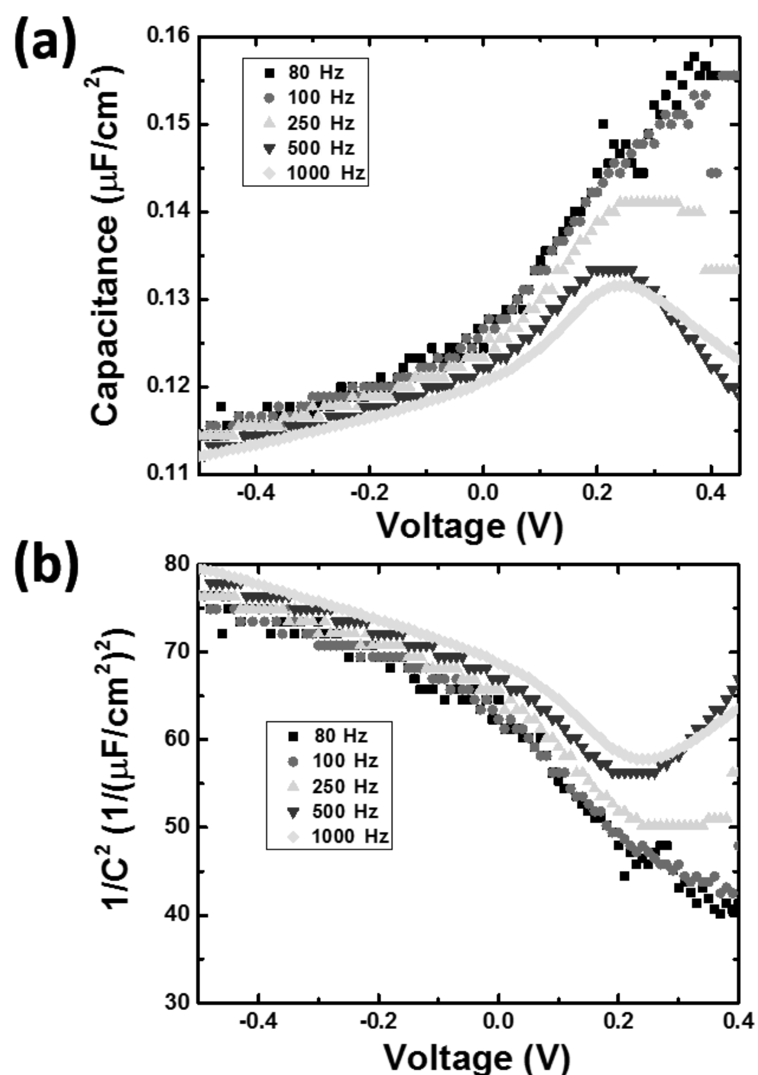

Figure 5.11: (a) C-V and (b) corresponding $1/C^2$-V plot at different sweeping frequencies (black (80 Hz), red (100 Hz), green (250 Hz), blue (500 Hz), and cyan (1 kHz)). Reprint from Yang et al. *ACS Applied Materials & Interfaces* 9.15 (2017): 13269-13277.

devices [112], nitrides [113], and CIGS [114] have also seen similar dispersive behaviors.

In C-V measurements of CQD and organic solar cells, the depletion capacitance

and the capacitance from the charging and discharging of defect states are probed simultaneously. Since the typical response time of a solar cell is given by $\tau = RC$, the increased capacitance due to the defect states will limit the response time [106,112]. At higher modulation frequencies, the carriers trapped in defects cannot respond to the fast AC signals, therefore they do not contribute to the measured capacitance, which allows only measurement of the bulk and depletion capacitance. Figure 5.11 (a) shows the C-V at five frequencies. With frequencies above 250 Hz, the normal shape of the depletion capacitance is recovered. The depletion width of the heterojunction reduces as the applied bias voltage increases from negative to positive (- 0.5 V to 0.5 V in Figure 5.11 (a)). Since the depletion capacitance is inversely proportional to the depletion width, the total capacitance increases until the external bias overtakes the built-in potential - where the depletion capacitance rapidly quenches to zero. A peak at ~ 0.25 V reflects the built-in potential of the devices, which is consistent with value reported by other groups [95,103,106]. The residual capacitance measured above built-in potential is related to the chemical potential of the devices [115].

At frequencies below 250 Hz, the capacitance from the trapping and detrapping carriers to or from the defects changes the shape of the C-V characteristics. The quenching of the capacitance above V_{bi} is not observed. In contrast, the capacitance continues to increase. The large defect and trap densities dominate the capacitive behavior. Both the defects associated with the surface states of the QDs and ZnO nanocrystals and the depletion capacitance due to the p-PbS/Au Schottky diode contribute to the low frequency capacitance under forward bias.

The MS plot shown in Figure 5.11 (b) deviates from a normal MS plot for a Schottky diode. Based on equation 5.8, the depletion capacitance is proportional to $\sqrt{(V_{bi} - V)}$ [110]. The V_{bi} is then extracted from the intercept of the x-axis of a linear fit of the MS plot. A $V_{bi} \geq 0.85$ V is observed, though very similar to the data reported in reference [95]; the value is perturbed by the charging and discharging of the defect states and voltage drop across multiple interfaces. These effects can be treated as a constant capacitance across the device [106, 111]. As reported by S. Willis et al. [111], with a constant capacitance subtracted (in our case 0.10 $\mu F/cm^2$) from the C-V measurements, values of $V_{bi} = 0.258$ V and $N_a = 1.2 \times 10^{17}\ cm^{-3}$ are extracted. These numbers are consistent with those reported elsewhere [95, 103, 106, 116].

Although MS analysis has been used successfully in PbS CQD solar cells [117], the prevalence of deep traps [103] in the PbS QDs and ZnO nanocrystals requires care when interpreting these data. The value of the background doping concentration N_a is bias dependent, since the applied bias will change the position of quasi Fermi level enabling passivation of the the states responsible for Fermi-level pinning by the injected carriers. Similarly, for the PbS/ZnO CQD solar cells, the bias dependent doping concentration behavior is found to account for the change of the gradient of the $1/C^2$ dependence with applied bias as seen in Figure 5.11 (a) and (b) .

Frequency dependent EQE measurements for a ZnO/TBAI-PbS/EDT-PbS quantum dot solar cell at high efficiency are plotted in Figure 5.12. The inset is a magnified image in of the EQE spectra, where a low frequency measurement

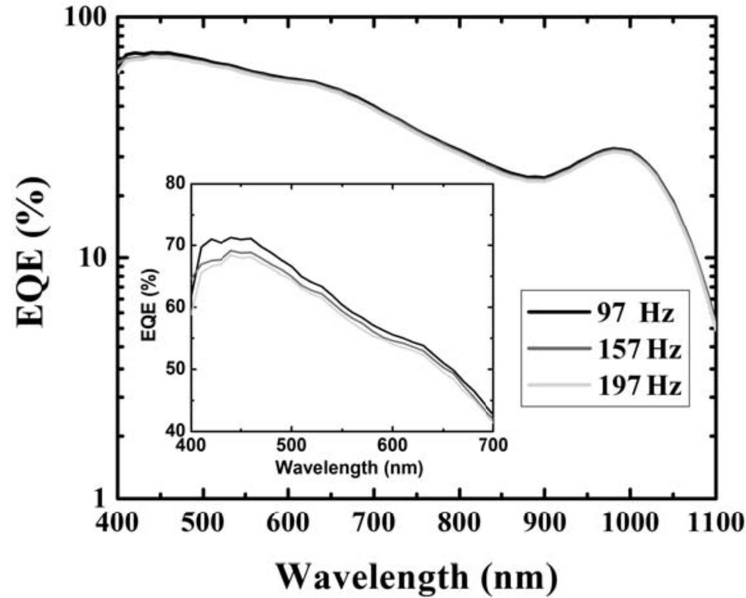

Figure 5.12: *EQE* measurements of a ZnO/TBAI-PbS/EDT-PbS quantum dot solar cell at modulation frequencies (black (97 Hz), red (157 Hz), and green (197 Hz); inset is a zoom in of the *EQE* spectra

enables a greater portion of the photogenerated carriers to be extracted rather than being perturbed by traps, resulting in a higher *EQE*. The higher frequency measurements lead to a lower *EQE*, which is attributed to the contribution of traps that prevent carrier extraction at high frequency.

5.2.4 Impedance Spectroscopy Analysis

Impedance spectroscopy (IS) is used to further investigate the system response of the PbS/ZnO solar cells as a function of AC signals. The impedance (inductance and capacitance) of the system is probed by the a small oscillation signal (20 mV on the order of kT); the impedance has both magnitude and phase, which is

dependent upon frequency. Since the dynamic of the diffusion and transport of carriers in photovoltaic devices under AC signals can be modeled by capacitive and resistive elements, IS has been used by several groups to investigate the parasitic resistance and minority carrier lifetime in solar cells [115, 118–120].

Two RC equivalent circuits shown in Figure 5.13 are used to model the back-to-back diodes as illustrated in the inset to Figure 5.6. R_1 and R_2 represent

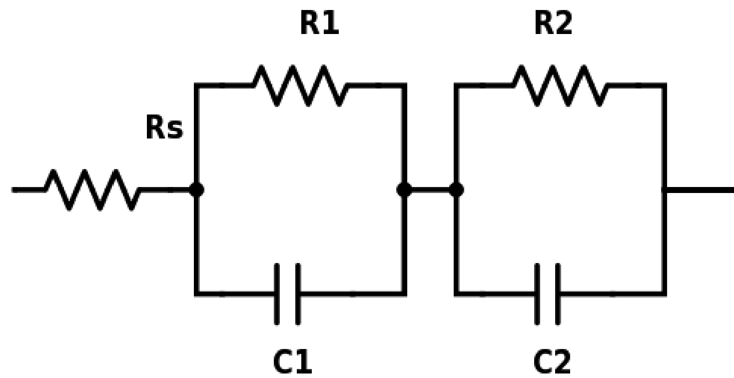

Figure 5.13: Two RC equivalent circuits modeling the back-to-back diodes.

the recombination resistances which are associated with the carrier transport losses in the device (generating heat), and C_1 and C_2 are related to the depletion capacitance induced by the charging and discharging processes. R_s represent the series resistance of the sample. The total impedance of this system is given by:

$$Z(\omega) = R_s + \frac{1}{\frac{1}{R_1} + j\omega C_1} + \frac{1}{\frac{1}{R_2} + j\omega C_2}. \tag{5.9}$$

The magnitude of the real and imaginary parts of the impedance are written as:

$$Z'(\omega) = R_s + \frac{R_1}{1 + (\omega R_1 C_1)^2} + \frac{R_2}{1 + (\omega R_2 C_2)^2}, \tag{5.10}$$

and

$$-Z''(\omega) = \frac{\omega C_1 R_1^2}{1 + (\omega R_1 C_1)^2} + \frac{\omega C_2 R_2^2}{1 + (\omega R_2 C_2)^2}, \tag{5.11}$$

respectively.

The Nyquist plots for IS measurements under reverse, zero, and forward bias conditions are shown in Figure 5.14, which can be used to extract the capacitance and system reponse from fitting the IS. The IS measurement is a frequency dependent measurement, where the Z' is plotted counter-clockwise from low frequency to high frequency against the Z''. The frequency range probed here is from 50 Hz to 13 MHz. Figure 5.14 (a) compares the IS data under zero and forward bias. Increasing the forward bias from 0 V to 0.5 V dramatically shrinks the Nyquist plot. The reduction in the magnitude of the impedance arc in forward bias is consistent with the dark J-V curve (see Figure 5.5 (b)), where 0 V corresponds to high resistance - low current and 0.5 V low resistance - high current ($R = dV/dJ$, where $R \propto 1/J$). This indicates a reduction of the total resistance, as expected in forward bias, where the decrease in the built-in potential of the diode allows efficient transport of majority carriers. An increase in the capacitance is also expected due to the reduced depletion width under forward bias [121].

Typically, applying a reverse bias to the system will increase the depletion width ($w = \sqrt{\frac{2\epsilon(V_{bi}-V)}{qN_a}}$). The wider depletion width will serve as a barrier for

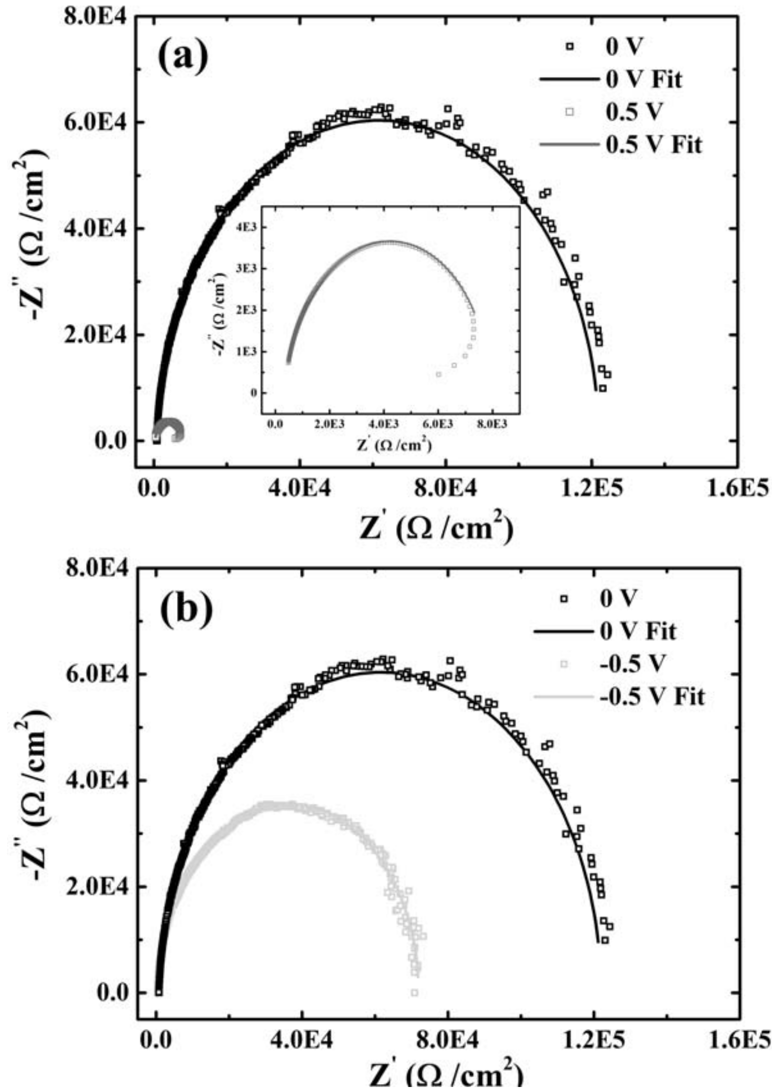

Figure 5.14: Nyquist plots for impedance spectroscopy measurements under (a) forward and zero bias, (b) reverse and zero bias. Black, red, and green represent the zero, forward, and reverse bias data. Open symbols and lines represent the measurement data and fitting data, respectively. Inset to (a) is a zoom-in Nyquist plot under forward bias.

majority carriers and inhibit the carrier transport across the device. Thus, the resistance of the whole device should be equal or larger than the resistance under zero bias. However, it is clear that reverse biasing the sample at - 0.5 V also

reduces the total impedance for the majority of the arc, which is clear from the point where the two arcs separate (Figure 5.14 (b)). The reduction of the impedance under reverse bias further supports the hypothesis of the formation of a second diode in reverse, which is effectively "turned-on" when a forward bias is applied across the PbS/Au Schottky junction, leasing to a break down of the main heterojunction through midgap state mediated tunneling processes. This band alignment under reverse bias is illustrated schematically in Figure 5.9 where the applied field is opposing the built-in potential of the PbS/Au interface increases and reflects the "effective turn-on" evident in the J-V measurements shown in Figure 5.5 (b) under high(er) reverse bias conditions across the whole device. This behavior reflects the combination of enhanced current injection from the Au-contact and PbS film and the avalanche break-down through defect-mediated tunneling at higher reverse bias.

An Electrochemical Impedance Spectroscopy (EIS) program [122] is used to further extract physical information from the IS results by fitting the data with a two RC circuit model. Figure 5.14 (a) and (b) shows the impedance spectra and the EIS fits for biases of -0.5 V (green), 0 V (black), and 0.5 V (red), respectively. The data is shown as symbols and the EIS fits as lines. Under forward bias, an inductive behavior is observed (a strong roll over at low frequencies in Figure 5.14 (a) inset), which is attributed to the minority carrier injection from the contact [123]. A similar inductive behavior has been observed in other devices including p-n junctions [123] and organic photovoltaics [124].

The inductive behavior under forward bias is usually observed in the fourth

		Main Junction (n-ZnO/p-PbS)			Schottky Junction (p-PbS/Au)		
Bias(V)	$R_s(\Omega/cm^2)$	$C_1(nF/cm^2)$	$R_1(\Omega/cm^2)$	$\tau_1(\mu s)$	$C_2(nF/cm^2)$	$R_2(\Omega/cm^2)$	$\tau_2(\mu s)$
Reverse	331.9 ± 4.3	9.2 ± 0.2	71200 ± 3100	653.6	0.52 ± 0.02	425.9 ± 9.7	0.22
Zero	835.4 ± 1.5	10.50 ± 0.04	120700 ± 1300	1267.7	70.1 ± 3.6	358 ± 39	25.07
Forward	377.5 ± 1.1	12.90 ± 0.01	7157 ± 19	92.3	61.20 ± 0.46	254.3 ± 3.8	21.68

Table 5.1: Parameters extracted from IS fitting. Reprint from Yang et al. *ACS Applied Materials & Interfaces* 9.15 (2017): 13269-13277.

quadrant in a Nyquist-plot. However, this behavior is not present in our samples. There are possibly two explanations: First, the frequency dependent capacitance under forward bias as shown in Figure 5.11 (a) leads to a reduction of capacitance as a function of increasing frequency. This larger capacitance at lower frequencies will decrease the real part of the impedance (see Equation 5.10). Second, in comparison with other reports that the inductive element is in series with the RC circuit, the inductive element in our model is more likely to be in series with the main junction but in parallel with the Schottky diode. This could also decrease the real part of the impedance without changing the sign of the imaginary part (Equation 5.10 and 5.11). Further investigation is needed to fully understand this behavior.

Table 5.1 summarizes the parameters extracted from the fitting. The Nyquist plot at zero bias shown in Figure 5.14 is fitted with two RC circuits. The depletion capacitance for p-n junction is given by Equation 5.6:

$$C = \sqrt{\frac{q\epsilon}{2\epsilon(V_{bi}-V)}\frac{N_a N_d}{N_a+N_d}}.$$

The acceptor concentration N_a for these two diodes is determined by the PbS-EDT CQDs thus, can be treated as the same. Since the electron concentration in the Au contact is larger than the ZnO NCs, the extracted capacitance of the Schottky diode (C_2) is larger (70.1 nF/cm^2) than that of the main n-ZnO/p-PbS junction ($C_1 = 10.5\ nF/cm^2$). Due to the opposite polarities of these two junctions in the device, a reverse bias across the main n-ZnO/p-PbS junction reflects a forward bias across the Schottky diode (vice versa for forward bias across the main diode). For the Schottky diode, a reverse (forward) bias will increase (decrease) the depletion width and reduce (increase) the device capacitance. The behavior of C_2 mimics the Schottky diode capacitance behavior at these three bias.

As shown in Figure 5.14 (a), the forward bias with respect to the main n-ZnO/p-PbS junction is in fact a reverse bias to the p-PbS/Au Schottky diode; thus, the C_2 extracted is smaller than the capacitance under zero bias. When switching to a reverse bias across the whole device, a larger C_2 is expected due to the decreased depletion width. However, we have seen a much smaller capacitance. The most likely explanation for such a behavior is related to the "turn on" of the Schottky diode; such a "turn on" will close the depletion width and eliminate the capacitance associated with the depletion region of the Schottky diode.

The depletion capacitance of the n-ZnO/p-PbS junction (C_1) reduces under reverse bias conditions, this reflects an increase in depletion width as expected. Under forward bias conditions, an increases in capacitance (see Table 5.1) is expected based on the MS description the p-n diode. However, if the applied forward bias exceeds the built-in potential, a sudden reduction of the depletion

capacitance is expected since the depletion region is closed. A forward bias IS measurement at + 0.5 V is well above the built-in potential $\sim$ 0.25 V based on the literature [95, 103, 106, 116] and our adjusted C-V results; however, the expected loss of the depletion capacitance is not observed (see Table 5.1). A possible explanation for this retention of capacity despite the absence of the depletion region is that the capacitance C_1 - rather than simply reflecting the depletion capacitance of the main junction - is derived from a combination of both n-ZnO/p-PbS depletion capacitance and a background capacitance associated with the defects in the QD film and at the interfaces; which generates the constant capacitance that also serves to produce the larger than expected V_{bi} as observed in the $C - V$ measurements (see Figure 5.11). At high biases above V_{bi}, the capacitance is dominated by this bulk contribution, which also perturbs the gradient of the $1/C^2 - V$ MS spectra (See Figure 5.11 (b)). A similar behavior in terms of larger than expected V_{bi} and therefore background doping concentrations, $N_a \approx 10^{17} cm^{-3}$, have been observed previously by several groups [95, 103, 106]; which is again consistent with a deep level in the QD films related to surface traps in the PbS CQDs [103, 125].

As stated above, the resistance associated with a normal p-n junction is expected to remain constant or increase as a function of applied reverse bias. However, the parallel resistance R_1 for the main n-ZnO/p-PbS junction decreases with increasing applied reverse bias, which is unusual but coincides with both our J-V measurements (reverse bias “turn on” or rectification) and the shrinkage of the Nyquist plot under reverse bias. The reduction of the effective resistance R_1

can be explained by the "leaky paths" introduced by the tunneling channels from the midgap states.

The product $R \cdot C$ gives the time constant (τ) for the circuit. τ typically is used to represent the minority carrier lifetime in forward bias, as carriers diffuse through the QD film. Here, however, τ accounts more generally for the time constant for charging and discharging of the defects or traps under different biases. In Table 5.1, τ_1 and τ_2 represent the time constants for the main n-ZnO/p-PbS junction and the Schottky diode produced at the PbS/Au interface, respectively. Under reverse bias, the minimal value of τ_2 suggests that the Schottky barrier has a negligible effect on the dynamics of the of carrier transport across the PbS/Au interface, since there will be no barrier for holes to cross the junction. At zero and forward bias, a larger τ_2 is evident, which is attributed to the limited hole transport across the PbS/Au junction. Hole transport across the junction is limited by the thermionic emission rate and Schottky barrier height under those conditions.

For the main n-ZnO/p-PbS heterojunction, a combination of field-aided extraction and defect mediated tunneling that facilitates carrier (electron) extraction contribute to the reduction of τ_1 under reverse bias. Under forward bias, the reduction of τ_1 is related to the "turn-on" of the device and saturation of the defect and interfacial states at higher injection levels. This description of the temporal dynamics of the carrier transport extracted from the IS measurements is supported by and consistent with the non-ideality of the $C-V$ measurements; as well as, the shunting and rectification observed in reverse bias in the $J-V$

measurements.

5.3 Conclusion

In this chapter, a suite of transport characterization techniques including current-voltage, capacitance-voltage, and impedance spectroscopy are used to investigate the effect of the interfaces and intrinsic surface states in an ITO/ZnO/PbS/Au colloidal quantum dot solar cell.

The low minority carrier diffusion length induced by losses associated with Shockley-Reed-Hall recombination processes (through interface states and midgap states associated with surface states on the PbS QDs) is the main factor limiting the performance of the CQD solar cells [64, 70, 93]. The non-monotonic behavior and dispersion in C-V measurements reflect the prevalence of these defect states. The long response time of the system under different biases suggest the carrier dynamics are dominated by these defect states. To further increase the performance of the CQD solar cells, better engineering of the interface states and surface state passivation are of great importance.

Chapter 6

Summary and Future Work

For the last few decades, substantial impacts for physical and biological systems, such as: the shrinkage of glaciers, rising sea levels, and an increase in frequency of severe tropical storms have been attributed to global warming with ("high") confidence. Despite some remaining debate, numerous scientific investigations suggest that there is a strong correlation between global warming and greenhouse gas (GHG) emissions.

Emissions of CO_2 have contributed 78% of the total GHG emission increase over the past five decades. In 2016, 35% of the CO_2 emission in the U.S. came from electricity generation. As a renewable energy source solar energy has a limitless and abundant supply, is accessible in most geographic areas, and much cleaner as compared to conventional fossil fuels, which have limited reserves, and require significant time to form. Therefore, incorporation of more solar energy into the power grid will help to reduce total CO_2 emissions, and reduce global warming.

Currently, solar energy is economically viable in areas where the infrastructure is limited, or the GHG emissions are restricted by governmental policy. To further facilitate the deployment of solar energy at the Tera-watt scale, higher efficiency and lower cost solar cells are still required. The efficiency of first generation - wafer based solar cells, and second generation - thin film solar cells are limited by the Shockley-Queisser limit for single bandgap solar cells. Third generation solar cells

are emerging technologies, which have been predicted to achieve power conversion efficiency beyond the Shockley-Queisser limit. Nanostructured materials have been investigated extensively for the past few decades as candidate systems for third generation photovoltaics. In this dissertation, nanostructured semiconductor quantum dots are studied for their potential applications for next-generation photovoltaics.

This dissertation specifically focused on the incorporation of $InAs/GaAs_{1-x}Sb_x$ quantum dots in high efficiency intermediate band solar cells, and lower cost PbS/ZnO thin film colloidal quantum dot solar cells. The operating principles of these two types of solar cells were introduced in Chapter 1. The intermediate band solar cell has the potential to improve the photovoltaic performance by increasing the total photogenerated current through a two step sub-bandgap photon absorption process. Solution synthesis techniques potentially give PbS/ZnO thin film colloidal quantum dot solar cells the advantage of low manufacturing costs, are of particular interest for building integrated-PV. Though these two types of QDSCs fall into two different categories, they share some of the same physical characteristics and therefore the same issues drive their operation and inhibit their potential commercial viability e.g. the prevalence of non-radiative recombination losses. The focus here was to study the physics behind those limiting factors, and to determine the subtle role of impurity and defect related processes, radiative and non-radiative losses, and their role on carrier extraction in theses systems.

In Chapter 3, two sets of MBE grown $InAs/GaAs_{1-x}Sb_x$ QD samples, one set with various InAs deposition thicknesses and the other set with different percentage

of Sb composition in the barrier materials were investigated, to determine the optimal growth conditions in terms of QD density and uniformity. Complementary atomic force microscopy (AFM) and photoluminescence (PL) measurements were used to characterize the quality of the QDs and to track the band alignment transition from type-I to type-II. A maximal areal density of $\sim 3.5 \times 10^{11}\ /cm^2$ was achieved for the 3.0 ML InAs/$GaAs_{0.86}Sb_{0.14}$ QD sample, along with reasonable uniformity in terms of both size and shape. A band alignment transition from type-I to type-II is evident when the Sb composition in the matrix reaches 14%. As such, 3.0 ML of InAs deposition and 14% Sb composition in the $GaAs_{1-x}Sb_x$ matrix were chosen as the optimal growth conditions for InAs/ $GaAs_{1-x}Sb_x$ QDSCs.

Four p-i-n GaAs solar cells with different intrinsic region designs were then grown, also by MBE. The material qualities of these four solar cells were initially investigated using PL measurements. Multimodal behavior due to sample inhomogeneities was observed via the appearance of an "s-shape" dependence of the QD peak energy as a function of temperature. Fast quenching of the PL spectra for samples with a thicker intrinsic region indicated the formation of a larger defect density in those samples. These behaviors qualitatively suggest that the defect states associated with the lattice mismatch between $GaAs_{0.86}Sb_{0.14}$ and GaAs account for the degradation of the quality of the materials investigated.

In Chapter 4, electrical characterization techniques including electroluminescence (EL), external quantum efficiency (EQE), and current-density-voltage (J-V) measurements were used to investigate the transport properties of the four solar

cells. Defect states associated with the lattice mismatch between $GaAs_{0.86}Sb_{0.14}$ and GaAs were again proposed to account for the limited performance of these solar cell devices. A hypothesis, that there is a transition from radiative to non-radiative recombination with increasing temperature is supported by the rapid quenching of both the PL and EL intensities, along with a simultaneous decrease in the z-factor extracted from spontaneous emission analysis from 2 to 1, above 150 K. It is suggested that such performance degradation with increasing temperature is facilitated by the thermal activation of the defects or ionization of impurities in the matrix and emitter regions of the solar cells. These results further suggest the prevalence of non-radiative processes at elevated temperatures in these systems, which are also qualitatively correlated with the anomalously large reduction of V_{oc} and appearance of unusual J_{sc} behavior in temperature dependent J-V measurements.

A suite of transport characterization techniques including current-voltage, capacitance-voltage, and impedance spectroscopy were used to investigate the effect of the interfaces and intrinsic surface states in an ITO/ZnO/PbS/Au colloidal quantum dot solar cell in Chapter 5. The negative influence on the carrier transport, the operating conditions of the CQD solar cell, and mechanisms therein, were also presented. The Schottky barrier formed at the PbS/Au interface results in Fermi level pinning that induces a non-linearity in the diode characteristic of this solar cell architecture. The low minority carrier diffusion length induced by losses associated with Shockley-Reed-Hall recombination processes through the presence of interface states, and via midgap states associated with surface states

on the PbS QDs are the main factor limiting the performance of the CQD solar cells. Non-monotonic behavior and dispersion in C-V measurements further reflect the prevalence of these defect states, and the long response time of the system under different biases suggest the carrier dynamics are dominated by trapping and de-trapping processes related to the defect states. To further increase the performance of the CQD solar cells, better engineering of the interface states and surface state passivation are therefore of great importance.

For InAs/GaAsSb QDSCs, additional experiments including concentration measurements and power dependent laser induced J-V measurements are currently being performed to further probe the nature and role of the defect states in these systems. These measurements will yield more information about the dynamics of the defect states (e.g., defect mediated tunneling mechanisms and the prevalence of thermal escape processes) as a function of the number of photogenerated carriers. To improve the performance of the QDSCs, better strain engineering is also required. Instead of using a GaAs substrate, an InP substrate has been proposed, which would be preferred since its compressive strain with respect to the GaAsSb could be engineered to compensate the tensile strain between the GaAsSb and InAs, which potentially could resolve the issues induced by the defect formation due to the lattice mismatch between the GaAs and GaAsSb. InP also has an improved spectral overlap with the AM 1.5G solar spectrum.

PbS/ZnO CQD solar cells suffer from a significant performance loss due to the surface and interfacial states. A better understanding of the ZnO is also of great importance. The doping density of ZnO affects the properties of the

main n-ZnO/p-PbS heterojunction interface and the depletion width in the PbS CQD layer. A ZnO Schottky device would be useful to determine the doping density by Mott-Schottky analysis. However, the sophisticated properties of ZnO nanocrystals have so far resulted in unsuccessful Schottky devices, and further work into the nature of these systems is required. Another area to be investigated centers on the ligands used for the PbS QD thin-film, since these ligands affect the surface passivation, doping concentration, and the band alignment with respect to the ZnO and Au interfaces. As such, a better surface preparation would help to reduce the negative effect of surface states and reduce the effects of the Schottky junction near the metal contact. Future work focuses on the characterizations of PbS QD solar cells with different capping ligands and advance chemical treatments of the various interfaces in the system.

References

[1] Rajendra K Pachauri, Myles R Allen, Vicente R Barros, John Broome, Wolfgang Cramer, Renate Christ, John A Church, Leon Clarke, Qin Dahe, and Purnamita Dasgupta. *Climate change 2014: synthesis report. Contribution of Working Groups I, II and III to the fifth assessment report of the Intergovernmental Panel on Climate Change*. IPCC, 2014.

[2] US EIA. Electric Power Annual 2015. Report, Washington DC: Energy Information Administration, United States Department of Energy, 2016.

[3] REN21. Renewables 2017 Global Status Report. Report, Paris: REN21 Secretariat, 2017.

[4] US EIA. Levelized Cost and Levelized Avoided Cost of New Generation Resources in the Annual Energy Outlook 2017. Report, Washington DC: Energy Information Administration, United States Department of Energy, 2017.

[5] Nancy M. Haegel, Robert Margolis, Tonio Buonassisi, David Feldman, Armin Froitzheim, Raffi Garabedian, Martin Green, Stefan Glunz, Hans-Martin Henning, Burkhard Holder, Izumi Kaizuka, Benjamin Kroposki, Koji Matsubara, Shigeru Niki, Keiichiro Sakurai, Roland A. Schindler, William Tumas, Eicke R. Weber, Gregory Wilson, Michael Woodhouse, and Sarah Kurtz. Terawatt-scale photovoltaics: Trajectories and challenges. *Science*, 356(6334):141–143, 2017.

[6] BW Research Partnership. U.S. Energy and Employment Report. Report, Washington DC: United States Department of Energy, 2017.

[7] BW Research Partnership. U.s. energy and employment report. Report, Washington DC: United States Department of Energy, 2016.

[8] William Shockley and Hans J. Queisser. Detailed Balance Limit of Efficiency of pn Junction Solar Cells. *Journal of Applied Physics*, 32(3):510–519, 1961.

[9] Martin A Green. *Third generation photovoltaics*. Springer, 2006.

[10] Louise C. Hirst and Nicholas J. Ekins-Daukes. Fundamental losses in solar cells. *Progress in Photovoltaics: Research and Applications*, 19(3):286–293, 2011.

[11] Martin A. Green. Third generation photovoltaics: Ultra-high conversion efficiency at low cost. *Progress in Photovoltaics: Research and Applications*, 9(2):123–135, 2001.

[12] D. M. Chapin, C. S. Fuller, and G. L. Pearson. A new silicon pn junction photocell for converting solar radiation into electrical power. *Journal of Applied Physics*, 25(5):676–677, 1954.

[13] Kunta Yoshikawa, Hayato Kawasaki, Wataru Yoshida, Toru Irie, Katsunori Konishi, Kunihiro Nakano, Toshihiko Uto, Daisuke Adachi, Masanori Kanematsu, Hisashi Uzu, and Kenji Yamamoto. Silicon heterojunction solar cell with interdigitated back contacts for a photoconversion efficiency over 26%. *Nature Energy*, 2:17032, 2017.

[14] Martin A. Green, Yoshihiro Hishikawa, Wilhelm Warta, Ewan D. Dunlop, Dean H. Levi, Jochen Hohl-Ebinger, and Anita W. H. Ho-Baillie. Solar cell efficiency tables (version 50). *Progress in Photovoltaics: Research and Applications*, 25(7):668–676, 2017.

[15] Fraunhofer Institute of Solar Energy. Multicrystalline Silicon Solar Cell with 21.9 Percent Efficiency, Feb 20, 2017 2017.

[16] Fraunhofer Institute for Solar Energy Systems. Photovoltaics Report. Report, Fraunhofer Institute for Solar Energy, 2017.

[17] P. T. Chiu, D. C. Law, R. L. Woo, S. B. Singer, D. Bhusari, W. D. Hong, A. Zakaria, J. Boisvert, S. Mesropian, R. R. King, and N. H. Karam. 35.8% space and 38.8% terrestrial 5J direct bonded cells. In *2014 IEEE 40th Photovoltaic Specialist Conference (PVSC)*, pages 0011–0013, 2014.

[18] Fraunhofer Institute for Solar Energy Systems. New world record for solar cell efficiency at 46% French-German cooperation confirms competitive advantage of European photovoltaic industry, Dec 1, 2014 2014.

[19] Sascha van Riesen, Martin Neubauer, Alexander Boos, Miguel Munoz Rico, Christophe Gourdel, Sven Wanka, Rainer Krause, Pascal Guernard, and Andreas Gombert. New module design with 4-junction solar cells for high efficiencies. *AIP Conference Proceedings*, 1679(1):100006, 2015.

[20] Tetsuo Soga. *Nanostructured materials for solar energy conversion*. Elsevier, 2006.

[21] Bradley D. Fahlman. *Nanomaterials*, pages 457–583. Springer Netherlands, Dordrecht, 2011.

[22] A. D. Yoffe. Low-dimensional systems: quantum size effects and electronic properties of semiconductor microcrystallites (zero-dimensional systems) and some quasi-two-dimensional systems. *Advances in Physics*, 42(2):173–262, 1993.

[23] Petra Reinke. *Inorganic nanostructures: properties and characterization.* John Wiley & Sons, 2012.

[24] Konstantin Moiseev, Yana Parkhomenko, and Vladimir Nevedomsky. Uniform insb quantum dots buried in narrow-gap inas(sb,p) matrix. *Thin Solid Films*, 543:74–77, 2013.

[25] P. P. Pompa, L. Martiradonna, A. Della Torre, L. Carbone, L. L. del Mercato, L. Manna, M. De Vittorio, F. Calabi, R. Cingolani, and R. Rinaldi. Fluorescence enhancement in colloidal semiconductor nanocrystals by metallic nanopatterns. *Sensors and Actuators B: Chemical*, 126(1):187–192, 2007.

[26] SamsungUS. Samsung QLED TV with Quantum Dots: Features & Accessories, 2017.

[27] Inc. QDlaser. Product and Service Portfolio, 2017.

[28] Antonio Luque and Antonio Martí. Increasing the Efficiency of Ideal Solar Cells by Photon Induced Transitions at Intermediate Levels. *Physical Review Letters*, 78(26):5014–5017, 1997. PRL.

[29] Antonio Luque, Antonio Martí, and Colin Stanley. Understanding intermediate-band solar cells. *Nature Photonics*, 6(3):146–152, 2012. 10.1038/nphoton.2012.1.

[30] Antonio Luque and Antonio Martí. The Intermediate Band Solar Cell: Progress Toward the Realization of an Attractive Concept. *Advanced Materials*, 22(2):160–174, 2010.

[31] Ramiro í, A. Martí, E. Antolín, and A. Luque. Review of Experimental Results Related to the Operation of Intermediate Band Solar Cells. *IEEE Journal of Photovoltaics*, 4(2):736–748, 2014.

[32] Y. Okada, N. J. Ekins-Daukes, T. Kita, R. Tamaki, M. Yoshida, A. Pusch, O. Hess, C. C. Phillips, D. J. Farrell, K. Yoshida, N. Ahsan, Y. Shoji, T. Sogabe, and J.-F. Guillemoles. Intermediate band solar cells: Recent progress and future directions. *Applied Physics Reviews*, 2(2):021302, 2015.

[33] SM Hubbard, CD Cress, CG Bailey, RP Raffaelle, SG Bailey, and DM Wilt. Effect of strain compensation on quantum dot enhanced GaAs solar cells. *Applied Physics Letters*, 92(12):123512, 2008.

[34] Greg Jolley, Hao Feng Lu, Lan Fu, Hark Hoe Tan, and Chennupati Jagadish. Electron-hole recombination properties of $In_{0.5}Ga_{0.5}As$/GaAs quantum dot solar cells and the influence on the open circuit voltage. *Applied Physics Letters*, 97(12):123505, 2010.

[35] KA Sablon, JW Little, KA Olver, Zh M Wang, VG Dorogan, Yu I Mazur, GJ Salamo, and FJ Towner. Effects of AlGaAs energy barriers on InAs/GaAs quantum dot solar cells. *Journal of Applied Physics*, 108(7):074305, 2010.

[36] Paul J Simmonds, Ramesh Babu Laghumavarapu, Meng Sun, Andrew Lin, Charles J Reyner, Baolai Liang, and Diana L Huffaker. Structural and optical properties of InAs/AlAsSb quantum dots with gaas (sb) cladding layers. *Applied Physics Letters*, 100(24):243108, 2012.

[37] RB Laghumavarapu, A Moscho, A Khoshakhlagh, M El-Emawy, LF Lester, and DL Huffaker. GaSb/GaAs type II quantum dot solar cells for enhanced infrared spectral response. *Applied Physics Letters*, 90(17):173125, 2007.

[38] Sabina Hatch, Jiang Wu, Kimberly Sablon, Phu Lam, Mingchu Tang, Qi Jiang, and Huiyun Liu. InAs/GaAsSb quantum dot solar cells. *Optics express*, 22(103):A679–A685, 2014.

[39] FK Tutu, IR Sellers, MG Peinado, CE Pastore, SM Willis, AR Watt, T Wang, and HY Liu. Improved performance of multilayer InAs/GaAs quantum-dot solar cells using a high-growth-temperature GaAs spacer layer. *Journal of Applied Physics*, 111(4):046101, 2012.

[40] A Martí, E Antolín, CR Stanley, CD Farmer, N López, P Díaz, E Cánovas, PG Linares, and A Luque. Production of photocurrent due to intermediate-to-conduction-band transitions: a demonstration of a key operating principle

of the intermediate-band solar cell. *Physical Review Letters*, 97(24):247701, 2006.

[41] Y Cheng, M Fukuda, VR Whiteside, MC Debnath, PJ Vallely, TD Mishima, MB Santos, K Hossain, S Hatch, HY Liu, et al. Investigation of InAs/GaAs$_{1-x}$Sb$_x$ quantum dots for applications in intermediate band solar cells. *Solar Energy Materials and Solar Cells*, 147:94–100, 2016.

[42] Michael Y Levy and Christiana Honsberg. Nanostructured absorbers for multiple transition solar cells. *IEEE Transactions on Electron Devices*, 55(3):706–711, 2008.

[43] R. B. Laghumavarapu, M. El-Emawy, N. Nuntawong, A. Moscho, L. F. Lester, and D. L. Huffaker. Improved device performance of InAsGaAs quantum dot solar cells with GaP strain compensation layers. *Applied Physics Letters*, 91(24):243115, 2007.

[44] Christopher G. Bailey, David V. Forbes, Ryne P. Raffaelle, and Seth M. Hubbard. Near 1 V open circuit voltage InAs/GaAs quantum dot solar cells. *Applied Physics Letters*, 98(16):163105, 2011.

[45] Kimberly A. Sablon, John W. Little, Vladimir Mitin, Andrei Sergeev, Nizami Vagidov, and Kitt Reinhardt. Strong Enhancement of Solar Cell Efficiency Due to Quantum Dots with Built-In Charge. *Nano Letters*, 11(6):2311–2317, 2011.

[46] Yoshitaka Okada, Takayuki Morioka, Katsuhisa Yoshida, Ryuji Oshima, Yasushi Shoji, Tomoya Inoue, and Takashi Kita. Increase in photocurrent by optical transitions via intermediate quantum states in direct-doped InAs/GaNAs strain-compensated quantum dot solar cell. *Journal of Applied Physics*, 109(2):024301, 2011.

[47] Yasushi Shoji, Kohei Narahara, Hideharu Tanaka, Takashi Kita, Katsuhiro Akimoto, and Yoshitaka Okada. Effect of spacer layer thickness on multi-stacked InGaAs quantum dots grown on GaAs (311)B substrate for application to intermediate band solar cells. *Journal of Applied Physics*, 111(7):074305, 2012.

[48] Pablo G. Linares, Antonio Martí, Elisa Antolín, Corrie D. Farmer, Íñigo Ramiro, Colin R. Stanley, and Antonio Luque. Voltage recovery in intermediate band solar cells. *Solar Energy Materials and Solar Cells*, 98:240–244, 2012.

[49] Lothar Nordheim. Zur Elektronentheorie der Metalle. I. *Annalen der Physik*, 401(5):607–640, 1931.

[50] Weyers Markus, Sato Michio, and Ando Hiroaki. Red Shift of Photoluminescence and Absorption in Dilute GaAsN Alloy Layers. *Japanese Journal of Applied Physics*, 31(7A):L853, 1992.

[51] W. Shan, W. Walukiewicz, J. W. Ager, E. E. Haller, J. F. Geisz, D. J. Friedman, J. M. Olson, and S. R. Kurtz. Band Anticrossing in GaInNAs

Alloys. *Physical Review Letters*, 82(6):1221–1224, 1999.

[52] J. Wu, W. Walukiewicz, and E. E. Haller. Band structure of highly mismatched semiconductor alloys: Coherent potential approximation. *Physical Review B*, 65(23):233210, 2002.

[53] Nazmul Ahsan, Naoya Miyashita, Muhammad Monirul Islam, Kin Man Yu, Wladek Walukiewicz, and Yoshitaka Okada. Two-photon excitation in an intermediate band solar cell structure. *Applied Physics Letters*, 100(17):172111, 2012.

[54] N. Ahsan, N. Miyashita, M. M. Islam, K. M. Yu, W. Walukiewicz, and Y. Okada. Effect of Sb on GaNAs Intermediate Band Solar Cells. *IEEE Journal of Photovoltaics*, 3(2):730–736, 2013.

[55] Weiming Wang, Albert S. Lin, and Jamie D. Phillips. Intermediate-band photovoltaic solar cell based on ZnTe:O. *Applied Physics Letters*, 95(1):011103, 2009.

[56] Tooru Tanaka, Masaki Miyabara, Yasuhiro Nagao, Katsuhiko Saito, Qixin Guo, Mitsuhiro Nishio, Kin M. Yu, and Wladek Walukiewicz. Photocurrent induced by two-photon excitation in ZnTeO intermediate band solar cells. *Applied Physics Letters*, 102(5):052111, 2013.

[57] Jinn-Kong Sheu, Feng-Wen Huang, Yu-Hsuan Liu, P. C. Chen, Yu-Hsiang Yeh, Ming-Lun Lee, and Wei-Chih Lai. Photoresponses of manganese-doped

gallium nitride grown by metalorganic vapor-phase epitaxy. *Applied Physics Letters*, 102(7):071107, 2013.

[58] P. G. Linares, A. Mart, E. Antoln, I. Ramiro, E. Lpez, E. Hernndez, D. Fuertes Marrn, I. Artacho, I. Tobas, P. Grard, C. Chaix, R. P. Campion, C. T. Foxon, C. R. Stanley, S. I. Molina, and A. Luque. Extreme voltage recovery in GaAs:Ti intermediate band solar cells. *Solar Energy Materials and Solar Cells*, 108:175–179, 2013.

[59] Yasuhiro Shirasaki, Geoffrey J. Supran, Moungi G. Bawendi, and Vladimir Bulovic. Emergence of colloidal quantum-dot light-emitting technologies. *Nat Photon*, 7(1):13–23, 2013.

[60] Chia-Hao M Chuang, Patrick R Brown, Vladimir Bulovi, and Moungi G Bawendi. Improved performance and stability in quantum dot solar cells through band alignment engineering. *Nature materials*, 13(8):796, 2014.

[61] Gi-Hwan Kim, F Pelayo Garcia de Arquer, Yung Jin Yoon, Xinzheng Lan, Mengxia Liu, Oleksandr Voznyy, Zhenyu Yang, Fengjia Fan, Alexander H Ip, and Pongsakorn Kanjanaboos. High-efficiency colloidal quantum dot photovoltaics via robust self-assembled monolayers. *Nano letters*, 15(11):7691–7696, 2015.

[62] Huan Liu, David Zhitomirsky, Sjoerd Hoogland, Jiang Tang, Illan J. Kramer, Zhijun Ning, and Edward H. Sargent. Systematic optimization of quan-

tum junction colloidal quantum dot solar cells. *Applied Physics Letters*, 101(15):151112, 2012.

[63] Xinzheng Lan, Oleksandr Voznyy, Amirreza Kiani, F Pelayo Garca de Arquer, Abdullah Saud Abbas, GiHwan Kim, Mengxia Liu, Zhenyu Yang, Grant Walters, and Jixian Xu. Passivation using molecular halides increases quantum dot solar cell performance. *Advanced Materials*, 28(2):299–304, 2016.

[64] Woojun Yoon, Janice E Boercker, Matthew P Lumb, Diogenes Placencia, Edward E Foos, and Joseph G Tischler. Enhanced open-circuit voltage of PbS nanocrystal quantum dot solar cells. *Scientific reports*, 3, 2013.

[65] Germ Garcia-Belmonte, Antoni Munar, Eva M. Barea, Juan Bisquert, Irati Ugarte, and Roberto Pacios. Charge carrier mobility and lifetime of organic bulk heterojunctions analyzed by impedance spectroscopy. *Organic Electronics*, 9(5):847–851, 2008.

[66] Justin B Sambur, Thomas Novet, and BA Parkinson. Multiple exciton collection in a sensitized photovoltaic system. *Science*, 330(6000):63–66, 2010.

[67] Octavi E Semonin, Joseph M Luther, Sukgeun Choi, Hsiang-Yu Chen, Jianbo Gao, Arthur J Nozik, and Matthew C Beard. Peak external photocurrent quantum efficiency exceeding 100% via MEG in a quantum dot solar cell. *Science*, 334(6062):1530–1533, 2011.

[68] Joshua J Choi, Whitney N Wenger, Rachel S Hoffman, YeeFun Lim, Justin Luria, Jacek Jasieniak, John A Marohn, and Tobias Hanrath. SolutionProcessed Nanocrystal Quantum Dot Tandem Solar Cells. *Advanced Materials*, 23(28):3144–3148, 2011.

[69] Ryan W. Crisp, Gregory F. Pach, J. Matthew Kurley, Ryan M. France, Matthew O. Reese, Sanjini U. Nanayakkara, Bradley A. MacLeod, Dmitri V. Talapin, Matthew C. Beard, and Joseph M. Luther. Tandem Solar Cells from Solution-Processed CdTe and PbS Quantum Dots Using a ZnTeZnO Tunnel Junction. *Nano Letters*, 17(2):1020–1027, 2017. PMID: 28068765.

[70] Mingjian Yuan, Mengxia Liu, and Edward H. Sargent. Colloidal quantum dot solids for solution-processed solar cells. *Nature Energy*, 1:16016, 2016.

[71] ASTM International. ASTM E490-00a(2014), Standard Solar Constant and Zero Air Mass Solar Spectral Irradiance Tables. Report, ASTM International, 2014.

[72] ASTM International. ASTM G173-03(2012), Standard Tables for Reference Solar Spectral Irradiances: Direct Normal and Hemispherical on 37° Tilted Surface. Report, ASTM International, 2012.

[73] Oliver Heaviside. *Electromagnetic theory*, volume 3. Cosimo, Inc., 2008.

[74] Simon M Sze and Kwok K Ng. *Physics of semiconductor devices*. John wiley & sons, 2006.

[75] Evgenij Barsoukov and J Ross Macdonald. *Impedance spectroscopy: theory, experiment, and applications*. John Wiley & Sons, 2005.

[76] M. C. Debnath, T. D. Mishima, M. B. Santos, Y. Cheng, V. R. Whiteside, I. R. Sellers, K. Hossain, R. B. Laghumavarapu, B. L. Liang, and D. L. Huffaker. High-density InAs/$GaAs_{1x}Sb_x$ quantum-dot structures grown by molecular beam epitaxy for use in intermediate band solar cells. *Journal of Applied Physics*, 119(11):114301, 2016.

[77] Y. Cheng, M. Fukuda, V. R. Whiteside, M. C. Debnath, P. J. Vallely, T. D. Mishima, M. B. Santos, K. Hossain, S. Hatch, H. Y. Liu, and I. R. Sellers. Investigation of InAs/$GaAs_{1x}Sb_x$ quantum dots for applications in intermediate band solar cells. *Solar Energy Materials and Solar Cells*, 147:94–100, 2016.

[78] K. Suzuki, R. A. Hogg, and Y. Arakawa. Structural and optical properties of type II GaSb/GaAs self-assembled quantum dots grown by molecular beam epitaxy. *Journal of Applied Physics*, 85(12):8349–8352, 1999.

[79] O. Ostinelli, G. Almuneau, and W. Bchtold. Photoluminescence and band offset of type-II AlGaAsSb/InP heterostructures. *Semiconductor Science and Technology*, 21(5):681, 2006.

[80] C. Y. Jin, H. Y. Liu, S. Y. Zhang, Q. Jiang, S. L. Liew, M. Hopkinson, T. J. Badcock, E. Nabavi, and D. J. Mowbray. Optical transitions in type-II

InAsGaAs quantum dots covered by a GaAsSb strain-reducing layer. *Applied Physics Letters*, 91(2):021102, 2007.

[81] Keun-Yong Ban, Darius Kuciauskas, Stephen P. Bremner, and Christiana B. Honsberg. Observation of band alignment transition in InAs/GaAsSb quantum dots by photoluminescence. *Journal of Applied Physics*, 111(10):104302, 2012.

[82] Claude Weisbuch and Borge Vinter. *Quantum semiconductor structures: fundamentals and applications*. Academic press, 2014.

[83] Yeongho Kim, Keun-Yong Ban, Chaomin Zhang, Jun Oh Kim, Sang Jun Lee, and Christiana B Honsberg. Efficiency enhancement in InAs/GaAsSb quantum dot solar cells with GaP strain compensation layer. *Applied Physics Letters*, 108(10):103104, 2016.

[84] HY Liu, IR Sellers, RJ Airey, MJ Steer, PA Houston, DJ Mowbray, J Cockburn, MS Skolnick, B Xu, and ZG Wang. Room-temperature, ground-state lasing for red-emitting vertically aligned InAlAs/AlGaAs quantum dots grown on a GaAs (100) substrate. *Applied physics letters*, 80(20):3769–3771, 2002.

[85] Yatendra Pal Varshni. Temperature dependence of the energy gap in semiconductors. *physica*, 34(1):149–154, 1967.

[86] JW Matthews. Defects associated with the accommodation of misfit between crystals. *Journal of Vacuum Science and Technology*, 12(1):126–133, 1975.

[87] Priyanka Singh and N Mr Ravindra. Temperature dependence of solar cell performance-an analysis. *Solar Energy Materials and Solar Cells*, 101:36–45, 2012.

[88] CR Brown, NJ Estes, VR Whiteside, B Wang, K Hossain, TD Golding, M Leroux, M Al Khalfioui, JG Tischler, CT Ellis, et al. The effect and nature of N–H complexes in the control of the dominant photoluminescence transitions in uv-hydrogenated GaInNAs. *RSC Advances*, 7(41):25353–25361, 2017.

[89] Li-Ko Yeh, Kun-Yu Lai, Guan-Jhong Lin, Po-Han Fu, Hung-Chih Chang, Chin-An Lin, and Hau He Jr. Giant efficiency enhancement of gaas solar cells with graded antireflection layers based on syringelike zno nanorod arrays. *Advanced Energy Materials*, 1(4):506–510, 2011.

[90] Alistair F Phillips, Stephen J Sweeney, Alfred R Adams, and Peter JA Thijs. The temperature dependence of 1.3-and 1.5-/spl mu/m compressively strained InGaAs (P) mqw semiconductor lasers. *IEEE Journal of selected topics in quantum electronics*, 5(3):401–412, 1999.

[91] Jianbo Gao, Joseph M. Luther, Octavi E. Semonin, Randy J. Ellingson, Arthur J. Nozik, and Matthew C. Beard. Quantum Dot Size Dependent J-V Characteristics in Heterojunction ZnO/PbS Quantum Dot Solar Cells. *Nano Letters*, 11(3):1002–1008, 2011.

[92] Patrick R. Brown, Richard R. Lunt, Ni Zhao, Timothy P. Osedach, Darcy D. Wanger, Liang-Yi Chang, Moungi G. Bawendi, and Vladimir Bulović. Improved Current Extraction from ZnO/PbS Quantum Dot Heterojunction Photovoltaics Using a MoO_3 Interfacial Layer. *Nano Letters*, 11(7):2955–2961, 2011.

[93] Illan J Kramer and Edward H Sargent. The architecture of colloidal quantum dot solar cells: materials to devices. *Chemical reviews*, 114(1):863–882, 2013.

[94] Jianbo Gao, Craig L. Perkins, Joseph M. Luther, Mark C. Hanna, Hsiang-Yu Chen, Octavi E. Semonin, Arthur J. Nozik, Randy J. Ellingson, and Matthew C. Beard. n-Type Transition Metal Oxide as a Hole Extraction Layer in PbS Quantum Dot Solar Cells. *Nano Letters*, 11(8):3263–3266, 2011.

[95] Zhiwen Jin, Aiji Wang, Qing Zhou, Yinshu Wang, and Jizheng Wang. Detecting trap states in planar PbS colloidal quantum dot solar cells. *Scientific Reports*, 6:37106, 2016.

[96] Jay M. Shah, Y.-L. Li, Th. Gessmann, and E. F. Schubert. Experimental analysis and theoretical model for anomalously high ideality factors (n>>2.0) in AlGaN/GaN p-n junction diodes. *Journal of Applied Physics*, 94(4):2627–2630, 2003.

[97] A. Chitnis, A. Kumar, M. Shatalov, V. Adivarahan, A. Lunev, J. W. Yang, G. Simin, M. Asif Khan, R. Gaska, and M. Shur. High-quality pn junctions

with quaternary AlInGaN/InGaN quantum wells. *Applied Physics Letters*, 77(23):3800–3802, 2000.

[98] Di Zhu, Jiuru Xu, Ahmed N. Noemaun, Jong Kyu Kim, E. Fred Schubert, Mary H. Crawford, and Daniel D. Koleske. The origin of the high diode-ideality factors in gainn/gan multiple quantum well light-emitting diodes. *Applied Physics Letters*, 94(8):081113, 2009.

[99] M. Brtzmann, U. Vetter, and H. Hofsss. BN/ZnO heterojunction diodes with apparently giant ideality factors. *Journal of Applied Physics*, 106(6):063704, 2009.

[100] Cheng-Xin Wang, Guo-Wei Yang, Hong-Wu Liu, Yong-Hao Han, Ji-Feng Luo, Chun-Xiao Gao, and Guang-Tian Zou. Experimental analysis and theoretical model for anomalously high ideality factors in ZnO/diamond p-n junction diode. *Applied Physics Letters*, 84(13):2427–2429, 2004.

[101] Leo Esaki. New Phenomenon in Narrow Germanium $p-n$ Junctions. *Physical Review*, 109(2):603–604, 1958.

[102] A. G. Chynoweth, W. L. Feldmann, and R. A. Logan. Excess Tunnel Current in Silicon Esaki Junctions. *Physical Review*, 121(3):684–694, 1961.

[103] D. Bozyigit, S. Volk, O. Yarema, and V. Wood. Quantification of Deep Traps in Nanocrystal Solids, Their Electronic Properties, and Their Influence on Device Behavior. *Nano Letters*, 13(11):5284–5288, 2013.

[104] E. H. Rhoderick. Metal-semiconductor contacts. *IEEE Proceedings I - Solid-State and Electron Devices*, 129(1):1, 1982.

[105] RJ Collins and DG Thomas. Photoconduction and surface effects with zinc oxide crystals. *Physical Review*, 112(2):388, 1958.

[106] Shawn M. Willis, Cheng Cheng, Hazel E. Assender, and Andrew A. R. Watt. The Transitional Heterojunction Behavior of PbS/ZnO Colloidal Quantum Dot Solar Cells. *Nano Letters*, 12(3):1522–1526, 2012.

[107] Frank Verbakel, Stefan CJ Meskers, and Ren AJ Janssen. Electronic memory effects in diodes of zinc oxide nanoparticles in a matrix of polystyrene or poly (3-hexylthiophene). *Journal of Applied Physics*, 102(8):083701, 2007.

[108] William K Liu, Kelly M Whitaker, Kevin R Kittilstved, and Daniel R Gamelin. Stable photogenerated carriers in magnetic semiconductor nanocrystals. *Journal of the American Chemical Society*, 128(12):3910–3911, 2006.

[109] Jiang Tang, Kyle W Kemp, Sjoerd Hoogland, Kwang S Jeong, Huan Liu, Larissa Levina, Melissa Furukawa, Xihua Wang, Ratan Debnath, and Dongkyu Cha. Colloidal-quantum-dot photovoltaics using atomic-ligand passivation. *Nature materials*, 10(10):765–771, 2011.

[110] Dieter K Schroder. *Semiconductor material and device characterization*. John Wiley & Sons, 2006.

[111] Shawn Willis. *Advanced Optoelectronic Characterisation of Solar Cells.* Oxford University, 2011.

[112] Thomas Kirchartz, Wei Gong, Steven A. Hawks, Tiziano Agostinelli, Roderick C. I. MacKenzie, Yang Yang, and Jenny Nelson. Sensitivity of the mottschottky analysis in organic solar cells. *The Journal of Physical Chemistry C*, 116(14):7672–7680, 2012.

[113] I. R. Sellers, W.-S. Tan, K. Smith, S. Hooper, S. Day, and M. Kauer. Wide depletion width of 1 eV GaInNAs solar cells by thermal annealing. *Applied Physics Letters*, 99(15):151111, 2011.

[114] P. K. Paul, K. Aryal, S. Marsillac, T. J. Grassman, S. A. Ringel, and A. R. Arehart. Identifying the source of reduced performance in 1-stage-grown cu(in, ga)se_2 solar cells. In *2016 IEEE 43rd Photovoltaic Specialists Conference (PVSC)*, pages 3641–3644, 2016.

[115] Ivan Mora-Sero, Germa Garcia-Belmonte, Pablo P. Boix, Miguel A. Vazquez, and Juan Bisquert. Impedance spectroscopy characterisation of highly efficient silicon solar cells under different light illumination intensities. *Energy & Environmental Science*, 2(6):678–686, 2009.

[116] Mark J Speirs, Dmitry N Dirin, Mustapha Abdu-Aguye, Daniel M Balazs, Maksym V Kovalenko, and Maria Antonietta Loi. Temperature dependent behaviour of lead sulfide quantum dot solar cells and films. *Energy & Environmental Science*, 9(9):2916–2924, 2016.

[117] Joseph M. Luther, Matt Law, Matthew C. Beard, Qing Song, Matthew O. Reese, Randy J. Ellingson, and Arthur J. Nozik. Schottky Solar Cells Based on Colloidal Nanocrystal Films. *Nano Letters*, 8(10):3488–3492, 2008.

[118] Y. Y. Proskuryakov, K. Durose, M. K. Al Turkestani, I. Mora-Ser, G. Garcia-Belmonte, F. Fabregat-Santiago, J. Bisquert, V. Barrioz, D. Lamb, S. J. C. Irvine, and E. W. Jones. Impedance spectroscopy of thin-film CdTe/CdS solar cells under varied illumination. *Journal of Applied Physics*, 106(4):044507, 2009.

[119] Adam Pockett, Giles E Eperon, Timo Peltola, Henry J Snaith, Alison Walker, Laurence M Peter, and Petra J Cameron. Characterization of planar lead halide perovskite solar cells by impedance spectroscopy, open-circuit photovoltage decay, and intensity-modulated photovoltage/photocurrent spectroscopy. *The Journal of Physical Chemistry C*, 119(7):3456–3465, 2015.

[120] Juan Bisquert. A variable series resistance mechanism to explain the negative capacitance observed in impedance spectroscopy measurements of nanostructured solar cells. *Physical Chemistry Chemical Physics*, 13(10):4679–4685, 2011.

[121] Boris D. Chernomordik, Ashley R. Marshall, Gregory F. Pach, Joseph M. Luther, and Matthew C. Beard. Quantum dot solar cell fabrication protocols. *Chemistry of Materials*, 2016.

[122] Ragoisha G. A Bondarenko A. S. *Progress in chemometrics research*, page 89102. Nova Publishers, 2005.

[123] Toshio Misawa. Impedance of bulk semiconductor in junction diode. *Journal of the Physical Society of Japan*, 12(8):882–890, 1957.

[124] G Kron, T Egerter, JH Werner, and U Rau. Electronic Transport in dye-sensitized nanoporous tiO2 solar cells comparison of electrolyte and solid-state devices. *The Journal of Physical Chemistry B*, 107(15):3556–3564, 2003.

[125] Vlad Sukhovatkin, Sean Hinds, Lukasz Brzozowski, and Edward H. Sargent. Colloidal Quantum-Dot Photodetectors Exploiting Multiexciton Generation. *Science*, 324(5934):1542–1544, 2009.

Appendix A

Publications and Presentations

A.1 List of publications

Below is a list of peer-reviewed publications in which I was either author or co-author.

1. **Y. Cheng**, V. R. Whiteside, M. C. Debnath, P. J. Vallely, A. J. Meleco, A. J. Roeth, T. D. Mishima, M. B. Santos, K. Hossain, S. Hatch, H. Liu, and I. R. Sellers, "An investigation of the role of radiative and non-radiative recombination processes in InAs/$GaAs_{1x}Sb_x$ quantum dot solar cells" *IEEE Journal OF Photovoltaics*, submitted.

2. **Y. Cheng**, V. R. Whiteside, M. C. Debnath, P. J. Vallely, A. J. Meleco, A. J. Roeth, T. D. Mishima, M. B. Santos, K. Hossain, S. Hatch, H. Liu, and I. R. Sellers, "An investigation of the role of recombination processes in InAs/$GaAs_{1x}Sb_x$ quantum dot solar cells" *2017 IEEE 44th Photovoltaic Specialists Conference (PVSC)*, Washington D. C., 2017, pp. 0005-0008.

3. **Y. Cheng**, M. D. C. Whitaker, R. Makkia, S. Cocklin, V. R. Whiteside, L. A. Bumm, E. Adcock-Smith, K. P. Roberts, P. Hari, and I. R. Sellers, "Role of Defects and Surface States in the Carrier Transport and Nonlinearity of the Diode Characteristics in PbS/ZnO Quantum Dot Solar Cells" *ACS Applied Materials & Interfaces* 9.15 (2017): 13269-13277.

4. **Y. Cheng**, M. Fukuda, V. R. Whiteside, M. C. Debnath, P. J. Vallely, A. J. Meleco, A. J. Roeth, T. D. Mishima, M. B. Santos, K. Hossain, S. Hatch, H. Liu, and I. R. Sellers, "Investigation of InAs/$GaAs_{1x}Sb_x$ quantum dots for applications in intermediate band solar cells " *2016 IEEE 43rd Photovoltaic Specialists Conference (PVSC)*, Portland, OR, 2016, pp. 0005-0008.

5. **Y. Cheng**, M. Fukuda, V. R. Whiteside, M. C. Debnath, P. J. Vallely, T. D. Mishima, M. B. Santos, K. Hossain, S. Hatch, H. Liu, and I. R. Sellers, "Investigation of InAs/$GaAs_{1x}Sb_x$ quantum dots for applications in intermediate band solar cells " *Solar Energy Materials and Solar Cells* 147 (2016): 94-100.

6. M. C. Debnath, T. D. Mishima, M. B. Santos, **Y. Cheng**, V. R. Whiteside, I. R. Sellers, K. Hossain, R. B. Laghumavarapu, B. L. Liang and D. L. Huffaker, "High-density InAs/$GaAs_{1x}Sb_x$ quantum-dot structures grown by molecular beam epitaxy for use in intermediate band solar cells" *Journal of Applied Physics* 119.11 (2016): 114301.

A.2 List of presentations

Below is a list of the presentations that I have either presented or been co-author of the presentation.

1. **Y. Cheng**, V. R. Whiteside, M. C. Debnath, P. J. Vallely, A. J. Meleco, A. J. Roeth, T. D. Mishima, M. B. Santos, K. Hossain, S. Hatch, H. Liu, and I. R. Sellers, "InAs quantum dots in a $GaAs_{1x}Sb_x$ matrix for intermediate

band solar cell" *2017 IEEE 44th Photovoltaic Specialists Conference (PVSC), Washington D. C., 2017 talk.*

2. A. J. Roeth, **Y. Cheng**, A. J. Meleco, V. R. Whiteside, M. C. Debnath, M. B. Santos, and I. R. Sellers, "Excitation energy dependence of the photovoltaic behavior of InAs/GaAsSb quantum dot solar cells" *APS March meeting, New Orleans, 2017 contributed talk.*

3. **Y. Cheng**, M. Fukuda, V. R. Whiteside, M. C. Debnath, P. J. Vallely, A. J. Meleco, A. J. Roeth, T. D. Mishima, M. B. Santos, K. Hossain, S. Hatch, H. Liu, and I. R. Sellers, "Investigation of InAs/$GaAs_{1x}Sb_x$ quantum dots for applications in intermediate band solar cells " *2016 IEEE 43rd Photovoltaic Specialists Conference (PVSC), Portland, 2016 talk.*

4. **Y. Cheng**, M. D. C. Whitaker, V. R. Whiteside, L. A. Bumm, and I. R. Sellers, "Investigation of transport properties of ZnO/PbS heterojunction solar cells" *APS March meeting, Baltimore, 2016 talk.*

5. **Y. Cheng**, M. C. Debnath, V. R. Whiteside, T. D. Mishima, M. B. Santos, K. Hossain, L. C. Phinney, and I. R. Sellers, "InAs quantum dots in a $GaAs_{1x}Sb_x$ matrix for intermediate band solar cell" *APS March meeting, Denver, 2013 talk.*